RESEARCH ACTIVITIES VIII
Laser Research Center for Molecular Science

VIII-A Developments and Researches of New Laser Materials

Although development of lasers is remarkable, there are no lasers which lase in ultraviolet and far infrared regions. However, it is expected that these kinds of lasers break out a great revolution in not only the molecular science but also in the industrial world.

In this project we research characters of new materials for ultraviolet and far infrared lasers, and develop new lasers by using these laser materials.

VIII-A-1 High-Energy, All-Solid-State, Ultraviolet Laser Power-Amplifier Module Design and Its Output-Energy Scaling Principle

ONO, Shingo; SUZUKI, Yuji; KOZEKI, Toshimasa; MURAKAMI, Hidetoshi; OHTAKE, Hideyuki; SARUKURA, Nobuhiko; SATO, Hiroki[1]; MACHIDA, Susumu[1]; SHIMAMURA, Kiyoshi[1]; FUKUDA, Tsuguo[2]
([1]Tokin Corp.; [2]Tohoku Univ.)

[*Appl. Opt.* **41**, 7556 (2002)]

We demonstrated that a coaxially pumped, large-aperture ultraviolet power-amplifier module using solid-state tunable laser medium Ce^{3+}:$LiCaAlF_6$ has 98-mJ, 290-nm, and 3-ns output pulses with sufficient extraction efficiency of 25%. The detailed information of design parameters, including the gain-coefficient dependence on pump condition, is successfully accumulated for further energy scaling for a terawatt-class ultraviolet chirped pulse amplification laser system or a high-pulse-energy laser system.

VIII-A-2 Generation of Intense 25-fs Pulses at 290 nm by Use of a Hollow Fiber Filled with High-Pressure Argon Gas

LIU, Zhenlin[1]; ONO, Shingo; KOZEKI, Toshimasa[2]; SUZUKI, Yuji[2]; SARUKURA, Nobuhiko[2]; HOSONO, Hideo[1,3]
([1]ERATO; [2]IMS, ERATO; [3]Tokyo Inst. Tech.)

[*Jpn. J. Appl. Phys.* **41**, L986 (2002)]

Frequency-tripled pulses at 290 nm from a 100-fs, 1-kHz Ti:sapphire regenerative amplifier system are spectrally broadened in hollow fiber filled with high-pressure argon gas. The self-phase-modulated pulses are compressed to 25 fs through a prism pair. The compressed pulse has an energy of 15 μJ.

VIII-A-3 Anomalous Power and Spectrum Dependence of THz Radiation from Femtosecond-Laser-Irradiated InAs in a High Magnetic Field of 14 T

OHTAKE, Hideyuki; MURAKAMI, Hidetoshi; YANO, Takayuki; ONO, Shingo; SARUKURA, Nobuhiko; TAKAHASHI, Hiroshi[1]; SUZUKI, Yuji[1]; NISHIJIMA, Gen[2]; WATANABE, Kazuo[2]
([1]GUAS; [2]Tohoku Univ.)

[*Appl. Phys. Lett.* **82**, 1164 (2003)]

We report on the THz radiation from femtosecond-laser-irradiated InAs in a high magnetic field up to 14 T. It is found that the radiation power exhibits anomalous magnetic-field dependence, including saturation, decrease, and recovery up to 14 T. Moreover, the radiation spectrum possesses a clear periodic structure over 6 T, possibly due to differently phased radiation from holes with different masses.

VIII-A-4 Significant Enhancement of Terahertz Radiation from InSb by Use of a Compact Fiber Laser and an External Magnetic Field

TAKAHASHI, Hiroshi[1]; SUZUKI, Yuji[1]; SAKAI, Masahiro; ONO, Shingo; SARUKURA, Nobuhiko; SUGIURA, Toshiharu[2]; HIROSUMI, Tomoya[2]; YOSHIDA, Makoto[2]
([1]GUAS; [2]Aisin Seiki Co., Ltd.)

[*Appl. Phys. Lett.* **82**, 2005 (2003)]

We investigated the magnetic-field dependence of terahertz (THz) radiation power from InSb. Significant enhancement of THz-radiation power is observed by using a compact fiber laser that delivered 100 fs optical pulses at a center wavelength of 1560 nm. Additionally, applying external magnetic fields dramatically enhanced the THz-radiation power. THz-radiation power reaches a maximum value at around 1.2 T, and its enhancement factor exceeds 100. From an applications viewpoint, this is a significant finding for practical light source design, since it is easily achieved by using a compact fiber laser and a conventional magnet.

VIII-A-5 Micro-Character Printing on a Diamond Plate by Femtosecond Infrared Optical Pulses

TAKESADA, Masaki[1,2]; VANAGAS, Egidijus[3]; TUZHILIN, Dmitri[3]; KUDRYASHOV, Igor[3]; SURUGA, Shoji[3]; MURAKAMI, Hidetoshi; SARUKURA, Nobuhiko; MATSUDA, Kazunari[1]; MONONOBE, Shuji[1]; SAIKI, Toshiharu[1]; YOSHIMOTO, Mamoru[4]; KOSHIHARA, Shin-ya[1]

([1]KAST; [2]Hokkaido Univ.; [3]Tokyo Instrument Inc.; [4]Tokyo Inst. Tech.)

[*Jpn. J. Appl. Phys.* **42**, 4613 (2003)]

Processing of less than 400 nm has been performed on the surface of a diamond plate by means of a femtosecond infrared pulse laser. Various characters with a size of about 1 μm were drawn by the femtosecond pulse laser system in conjunction with a microscope equipped with a precisely controlled piezo-stage. The tightly focused laser light on the flat surface of the diamond made it possible to minimize the light-induced graphitization. The surface of the diamond plate after laser machining was analyzed by micro-Raman measurements to estimate the graphitization effect induced by laser irradiation. The obtained results indicate that graphitization increased with the number of irradiated laser pulses.

VIII-A-6 Mode-Locking Stability Adjustment of a Kerr-Lens Mode-Locked Ti:sapphire Laser, Analyzed by a Recently Developed Real-Time Spectrum Analyzer

TAKAHASHI, Hiroshi[1]; SUZUKI, Yuji[1]; MURAKAMI, Hidetoshi; ONO, Shingo; SARUKURA, Nobuhiko; NAKAMURA, Tadashi[2]
([1]GUAS; [2]Textronix Japan., Ltd.)

[*Jpn. J. Appl. Phys.* **42**, 4330 (2003)]

This is a report on the mode-locking stability of a Kerr-lens mode-locked Ti:sapphire, measured by a newly developed noise measurement method. Mode-locking stability is monitored *via* a power spectrum, which is obtained by irradiating optical pulses onto a fast photodiode, and by processing the detected signal using a recently developed real-time spectrum analyzer. The mode-locking stability of the Ti:sapphire laser strongly depends on pump power and becomes unstable as pump power decreases from an optimum power level. Amplitude fluctuation and Q-switched mode-locking are notably observed as the main causes for a break in a continuous-wave (CW) mode-locking operation. Moreover, chaotic frequency hopping is observed in a Q-switched mode-locking operation. A real-time spectrum analyzer provides a time-varying power spectrum, which enables easy adjustment for stable CW mode-locking operation of ultra-fast solid state lasers.

VIII-A-7 Magnetic-Field-Induced Enhancement of THz-Radiation Power from Femtosecond-Laser-Irradiated InAs up to 27 T

TAKAHASHI, Hiroshi[1]; SUZUKI, Yuji[1]; QUEMA, Alex; SAKAI, Masahiro; YANO, Takayuki; ONO, Shingo; SARUKURA, Nobuhiko; HOSOMIZU, Masato[2]; TSUKAMOTO, Takeyo[2]; NISHIJIMA, Gen[3]; WATANABE, Kazuo[3]
([1]GUAS; [2]SUT; [3]Tohoku Univ.)

[*Jpn. J. Appl. Phys.* **42**, L532 (2003)]

Magnetic-field dependence of THz-radiation power from InAs surface is investigated by using a hybrid magnet, which is capable of providing a magnetic field up to 28 T. It is found that THz-radiation power saturates at around 3 T and also at 13 T. Maximum THz-radiation power with high-frequency component spectrum is observed at 3-T. This result leads to the conclusion that a magnetic field of 3 T is optimum for the enhancement of THz-radiation power. Additionally, THz-radiation spectrum exhibits periodic structure at magnetic fields above 12 T. This can be attributed to the change of dielectric constant induced by the strong magnetic field resulting in the interference of THz-radiation pulses from the front and back surfaces of the InAs substrate.

VIII-A-8 Optical Properties of Ce^{3+} Ion Doped $LiCaAlF_6$ Crystal in Vacuum Ultraviolet Region

TAKAHASHI, Hiroshi[1]; SAKAI, Masahiro; ONO, Shingo[1]; SARUKURA, Nobuhiko; SATO, Hiroki[2]; YOSHIKAWA, Akira[2]; FUKUDA, Tsuguo[1]
([1]GUAS; [2]Tohoku Univ.)

[*Jpn. J. Appl. Phys.* **42**, L660 (2003)]

The optical properties of Ce^{3+} ion doped $LiCaAlF_6$ (Ce:LiCAF) crystal is investigated in vacuum ultraviolet (VUV) region. It is found that the optical excitation from the valence band of LiCAF crystal to the highest ^2D excited state of Ce^{3+} can be utilized as an efficient excitation channel to obtain the ultraviolet emission due to $4f$–$5d$ transition of Ce^{3+}. Furthermore, the energy level of ^2D state is found to be located near the conduction band of LiCAF crystal, which leads to the electron transfer from the LiCAF crystal to the active Ce^{3+} ion.

VIII-A-9 Identification of Potential Estrogenic Environmental Pollutants by Terahertz Transmission Spectroscopy

QUEMA, Alex; TAKAHASHI, Hiroshi[1]; SAKAI, Masahiro; GOTO, Masahiro; ONO, Shingo; SARUKURA, Nobuhiko; SHIODA, Ryu[2]; YAMADA, Norihide[2]
([1]GUAS; [2]Agilent Tech. Res. Cent.)

[*Jpn. J. Appl. Phys.* **42**, L932 (2003)]

Using magnetically enhanced terahertz radiation from InAs, various naphthols, which exhibits estrogenic like activity and are potentially mimic natural hormones, are studied. The experimental results show that the naphthols, depicted by the position of the hydroxyl (-OH) component at different carbon atom sites of the naphthalene compound, are distinguishable based on the absorption of THz radiation. It is found that the THz radiation absorption is strongly related to the crystal symmetry and dipole moment of these isomers.

VIII-A-10 Excitation Fluence Dependence of Terahertz Radiation Mechanism from Femtosecond-Laser-Irradiated InAs under Magnetic Field

TAKAHASHI, Hiroshi[1]; QUEMA, Alex; YOSHIOKA, Ryoichiro; ONO, Shingo; SARUKURA, Nobuhiko
([1]GUAS)

[*Appl. Phys. Lett.* **83**, 1068 (2003)]

The excitation fluence and magnetic field dependence of terahertz (THz) radiation power from InAs is investigated. At low excitation fluence, an enhancement of the THz-radiation power is observed independent of the magnetic-field direction. As the excitation fluence is increased, a crossover of terahertz radiation mechanism is observed. At excitation fluence above this crossover, the radiation power is either enhanced or reduced depending on the magnetic-field direction. These results are explained by considering the different THz-radiation mechanisms from the InAs surface with or without photoexcited carrier screening.

VIII-B Development and Research of Advanced Tunable Solid State Lasers

Diode-pumped solid-state lasers can provide excellent spatial mode quality and narrow linewidths. The high spectral power brightness of these lasers has allowed high efficiency frequency extension by nonlinear frequency conversion. Moreover, the availability of new and improved nonlinear optical crystals makes these techniques more practical. Additionally, quasi phase matching (QPM) is a new technique instead of conventional birefringent phase matching for compensating phase velocity dispersion in frequency conversion. These kinds of advanced tunable solid-state light sources, so to speak "Chroma Chip Lasers," will assist the research of molecular science.

In this projects we are developing Chroma Chip Lasers based on diode-pumped-microchip-solid-sate lasers and advanced nonlinear frequency conversion technique.

VIII-B-1 Highly Efficient Continuous-Wave 946-nm Nd:YAG Laser Emission under Direct 885-nm Pumping

LUPEI, Voicu[1]; PAVEL, Nicolaie[2]; TAIRA, Takunori

([1]IAP-NILPRP, Romania; [2]IMS and IAP-NILPRP, Romania)

[*Appl. Phys. Lett.* **81**, 2677 (2002)]

The quasi-three-level 946-nm emission of Nd^{3+} in YAG is important for construction of low-heat solid-state lasers at fundamental frequency or for doubling it by nonlinear processes to blue 473-nm radiation. Successful attempts to lase the Nd:YAG at 946 nm in continuous-wave (CW) or pulsed regimes have been reported;[1)–3)] however, the performances of these lasers are still limited and the full lasing potential is not yet exploited. This paper discusses some possibilities to improve the laser emission parameters and to reduce the generation of heat by pumping directly into the emitting level.

In a CW quasi-three-level laser the fractional thermal loading η_h (*i.e.* the fraction of absorbed power that is transformed into heat by non-radiative processes), contains specific contributions from the ions that participate in the lasing process as well as from those that do not lase. The quantum defect ratio for the 946-nm laser emission is much larger than that corresponding to the fluorescence emission, whose average wavelength $\bar{\lambda}$ is 1038 nm. The contribution to heating from each excited Nd^{3+} ion that does not lase would be then much larger than from each ion that participate to lasing; thus, a high laser extraction efficiency will contribute to the reduction of the heat generated in the pumped laser material. A complex interrelation exists between the laser emission parameters and the heat generation and an optimization of all these characteristics would be necessary in order to make a complete use of the quasi-three-level emission potential. Both the laser emission parameters and the generation of heat are influenced by the quantum defect ratio $\eta_{qd} = \lambda_p/\lambda_l$ between the pump and laser emission wavelengths. Traditionally the 946-nm Nd:YAG lasers are pumped at 808 nm into the level $^4F_{5/2}$: this induces a parasitic upper quantum defect of ~1000 cm^{-1} between the pump and the emitting laser levels that accounts for more than half of the total quantum defect. As evidenced by the spectroscopic investigations[4)–6)] very suitable for diode laser pumping the Nd:YAG is the double-peaked absorption band centred around 885 nm that collects the thermally activated transitions $Z_2 \rightarrow R_1$ and $Z_3 \rightarrow R_2$ of the absorption spectrum $^4I_{9/2} \rightarrow {}^4F_{3/2}$. This wavelength of pump determines an increase of the quantum defect ratio by ~ 9.5%, leading to a corresponding improvement of the laser emission parameters. Moreover, by restricting strongly the reabsorption losses η_h could be diminished by as much as 50 to 60% from the value corresponding to that of 808-nm pumping.

The 946-nm CW emission in a 1.0-at.% Nd:YAG crystal (3-mm thick) is investigated by using 885-nm Ti:sapphire longitudinal pumping. The crystal was AR coated for 808 and 885 nm (reflectivity, $R < 0.5\%$), and also 946 and 1064 nm ($R < 0.1\%$). A plane-concave resonator of 25-mm length and output mirror of 50-mm radius was employed. The Ti:sapphire laser is focused on the Nd:YAG in a 160-μm diameter spot. The 946-nm laser output power *vs.* the absorbed power at 885 nm is shown in Figure 1. This dependence reflects the increase of the slope efficiency $\eta_s^{(a)}$ with increasing absorbed power, owing to the saturation of the reabsorption. The output power depends on *R*: a high reflectivity leads to a lower threshold but also to lower slope efficiency. The best results are obtained with $R = 97\%$ output mirror: the absorbed power at threshold is ~ 120 mW and $\eta_s^{(a)}$ at absorbed power about 4 times larger than the threshold reaches as much as 68%. Output power of 180 mW resulted for ~ 500 mW absorbed power at 885-nm. In our knowledge this is the largest slope efficiency obtained for CW 946-nm Nd:YAG laser emission. At $R = 93\%$ the threshold increases to ~ 260 mW, but $\eta_s^{(a)}$ at pump ~ 2 times larger than the threshold is already 63%. For $R = 98.8\%$ $\eta_s^{(a)}$ was 47%, while the absorbed power at threshold was ~ 110 mW.

The 1064-nm emission at 885-nm pumping (Figure 2) gives $\eta_s^{(a)}$ of 72% and 30 mW absorbed power at threshold for a mirror with $R = 90\%$. Slope efficiencies of 64% and 31% were obtained for $R = 95$ and 99%, respectively, with absorbed pump power at threshold of ~ 13 and ~ 5 mW.

The laser emission at 946 nm and 1064 nm under 808-nm pumping shows similar trends. The highest $\eta_s^{(a)}$at absorbed power of ~ 4 times above the threshold, namely 48%, resulted for the $R = 93\%$ mirror; the threshold was ~ 300 mW and ~ 350 mW at 946 nm were obtained for an absorbed power of ~ 1.3 W. For *R*

= 97% $\eta_s^{(a)}$ = 45% and the threshold was ~ 200 mW, while for R = 98.8% these parameters were 24% and ~ 145 mW. The 1064-nm emission had slopes of 12%, 42%, 51% for the output mirror with R = 99, 95, and 90%, respectively, while the 808-nm power absorbed at threshold was 16, 26, and ~ 45 mW. It can be observed that under 808-nm pumping the emission threshold is larger and $\eta_s^{(a)}$ is smaller than for 885-nm pumping.

Pumping resonantly into the emitting level can sensibly enhance the laser emission parameters in absorbed power. However, the weaker absorption at 885 nm as compared to 808 nm for a component of given length could reverse the situation when the laser parameters are expressed in input power. Lengthening the active component in order to increase the pump absorption will increase the reabsorption losses. A suitable solution for increasing the absorption could be a decoupling of the lengths for pump absorption from that of reabsorption, which can be achieved in a laser configuration with multi-pass of the pumping radiation inside the laser component.[7] The use of more concentrated Nd:YAG components in such a multi-pass laser configuration could also improve the absorption. Once the reabsorption becomes very low, the effect of reduction of the emission quantum efficiency by concentration quenching on threshold in these materials could be completely compensated by the increased pump absorption efficiency, similar to the 1064-nm Nd:YAG lasers. Further calculation shows that in a multi-pass laser cavity the laser parameters in input power under 885 and 808-nm pumping are similar. Such multi-pass 885-nm pumped 946-nm Nd:YAG lasers would enable an optimum use of pump power, resulting in superior laser performances and low heat generation that could enable the scaling to higher powers.

References

1) T. Y. Fan and R. L. Byer, *J. Opt. Soc. Am. A* **3**, 109 (1986).
2) G. Holleman, E. Piek and H. Walther, *Opt. Lett.* **19**, 192 (1994).
3) P. Zeller and P. Peuser, *Opt. Lett.* **25**, 34 (2000).
4) R. Lavi and S. Jackel, *Appl. Opt.* **39**, 3093 (2000).
5) V. Lupei, A. Lupei, N. Pavel, T. Taira, I. Shoji and A. Ikesue, *Appl. Phys. Lett.* **79**, 590 (2001).
6) V. Lupei, A. Lupei, S. Georgescu, T. Taira, Y. Sato and A. Ikesue, *Phys. Rev. B* **64**, 092102 (2001).
7) A. Giesen, H. Hugel, A. Voss, K. Wittig, U. Braud and H. Opower, *Appl. Phys. B* **58**, 365 (1994).

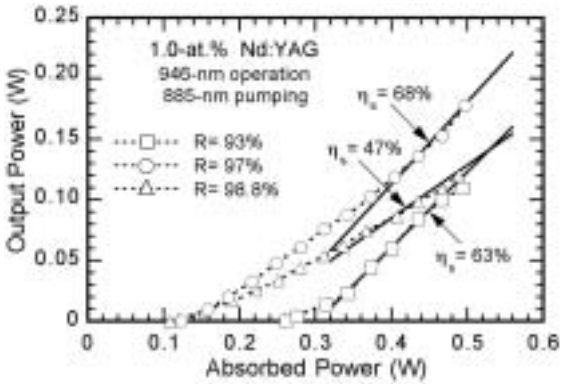

Figure 1. Output power at 946 nm function of the absorbed power under 885-nm Ti:Sapphire pumping.

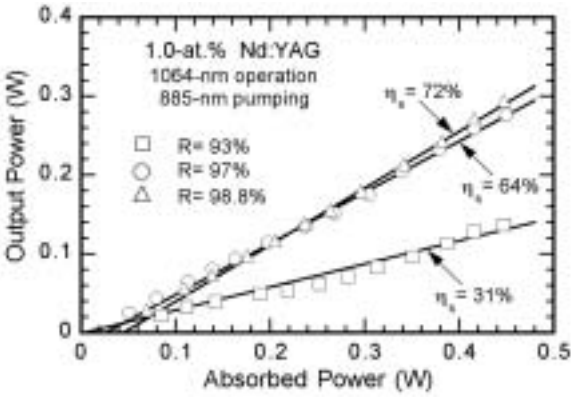

Figure 2. 1064-nm output power versus the absorbed power under 885-nm Ti:Sapphire pumping.

VIII-B-2 100-W Quasi-Continuous-Wave Diode Radially Pumped Microchip Composite Yb:YAG Laser

DASCALU, Traian[1,2,3]; TAIRA, Takunori; PAVEL, Nicolaie[2,3]

([1]CREATE-Fukui, Japan; [2]IAP-NILPRP, Romania; [3]IMS)

[*Opt. Lett.* **27**, 1791 (2002)]

The diode-pumped Yb:YAG medium has been demonstrated as a good candidate for high-power 1-μm laser systems as well as for tunable, single-axial-mode microchip configurations.[1)–3)] Besides of choice of gain medium, the configuration used for pumping, cooling and extraction plays a critical role in power scaling of a microchip laser. Recently, for scaling of a microchip Yb:YAG laser we proposed a new geometry that consists of a diode radial pumped composite Yb:YAG microchip.[4)] Theoretically was concluded that an output power of 100 W with overall optical-to-optical efficiency η_o of 39% could be obtained, employing an 13-at.% Yb-doped core of 2-mm diameter. Here we report first experimental results on this configuration: under quasi-continuous-wave (CW) pumping the best results of 112-W peak output power with η_o = 38% and slope efficiency in input power η_s of 63% were obtained.

The configuration of the diode radial pumped Yb:YAG microchip laser is shown in Figure 1. The composite crystal consists of a Yb:YAG doped core of square shape and that is diffusion bonded to an undoped YAG region. One side of the crystal was high reflectivity (HR) coated at the laser wavelength while the other surface was AR coated for this wavelength. The crystal is mounted with its HR coated side on a microchannel cooling system (water flow type, 20 °C temperature) and an indium based soldering technique was used to decrease the thermal impedance between them. The crystal was pumped by two JOLD-100-CAXF-15A diode fiber-coupled lasers (JenaOptik, Laserdiode GmbH, Germany) that delivers, each one, ~ 120 W maximum power at 940 nm ($\Delta\lambda$ ~ 4.0 nm FWHM) through a fiber of 0.6-mm core diameter and NA = 0.22. The pumping light was focused on the edge of the undoped YAG with a 1:1 achromatic optical system. Inside of the microchip it propagates by total

internal reflection through the Yb-doped core where is partially absorbed. The remained light propagates until it reaches the other edge of the undoped YAG slab: part of this light will be lost through the pumping window placed at that side, while the left light is scattered back into the microchip by a diffuse reflector.

Two crystals, one with core of 10-at.% Yb-doping level and 2 × 2-mm^2 square shape (sample #A) and the second of 1.2 × 1.2 mm^2 square 15-at.% Yb-doped core (sample #B) were used under a two diode lasers pumping, as in Figure 1. The slab shapes of 5-mm width and 0.8-mm thickness were obtained by cutting them from a 10-mm diameter rod.

The output *vs.* input power characteristics for these two crystals are presented in Figure 2, under quasi-CW pumping with rectangular pulses of 5 Hz repetition rate and 2.5% duty factor (pumping pulses of 5-ms duration). As output coupler a concave mirror of 0.1-m radius, placed 50-mm apart of the active medium, was employed. When the crystal #A is used with an output mirror of 97% reflectivity (R) a maximum output peak power of 66 W resulted at 220-W pumping power (Figure 2a); η_s was 49% (~ 58% in absorbed power). With an output mirror of R = 90% the threshold increases at ~ 33 W, however with an improved η_s of 54% (~ 64% in absorbed power). When crystal #B with R = 97% mirror was used we obtained maximum 63-W peak power with ~ 20-W absorbed at threshold and η_s far above threshold of 41% (~ 52% in absorbed power), as presented in Figure 2b. With the output mirror of R = 90% the threshold increased at ~ 33 W while η_s = 43% (~ 54% in absorbed power). The quasi-CW pumping with pulses of several milliseconds duration reduces the heat load of the crystals. The pulse duration is, however, long compared to the time necessary for the laser emission to reach the steady-state behavior. The obtained results suggest, therefore, the performances that could be obtained in CW operation if the heat is efficiently removed.

The power scalability of this microchip laser was investigated by using a third diode, placed perpendicular to the pumping directions of the first two (the inset of Figure 3). Figure 3 shows the input peak power *vs.* of pump peak power for the plane-concave resonator with R = 97% output mirror. A maximum of 112-W peak power for 298-W pump power, with η_s = 63%, was obtained for the crystal #B. For the crystal #A maximum peak power was 100 W and η_s was determined as 53%.

A future objective of this research is to demonstrate high-duty cycle or CW operation of Yb:YAG composite microchip by using this pumping scheme. As a first evaluation, the pumping repetition rate was increased, while the pumping pulse duration was kept at 5 ms. When the repetition rate increases from 10, to 30 and 60 Hz, the maximum peak output power for 298-W peak pump power decreases from 98, to 89 and 74 W, respectively, while η_s reduces from 52%, to 46% and 32% (output mirror with R = 90%). As much as 23-W average output power was obtained for 90-W average pump power (60 Hz repetition rate, 0.3 duty cycle). The temperature of the upper surface crystal was below 70 °C during all these experiments. An attempt of CW operation delivers 7.5 W for a pump power of 90 W; at this point an increase of the crystal temperature beyond 120 °C was however observed.

In conclusion a diode radial pumped composite Yb:YAG microchip laser is presented. Quasi-CW pumping of a 15-at.% Yb:YAG core (1.2 × 1.2 mm^2) with pulses of 5-Hz repetition rate and 2.5% duty cycle delivers 112-W peak power with 63% slope efficiency and 38% overall optical-to-optical efficiency. For further works, the temperature distribution into the Yb:YAG core was determined by a finite element method, while the output power was evaluated by taking into account the spatial variation of both the pump and the laser beams. The results show that efficient CW operation with 100-W power at room temperature could be obtained by using a 400-μm thick Yb:YAG chip and by improving the thermal impedance between the crystal and cooling head through an advanced soldering technique.

References

1) E. C. Honea, R. J. Beach, S. C. Mitchel, J. Skidmore, M. A. Emanuel, S. B. Sutton, S. A. Payne, P. V. Avizonis, R. S. Monroe and D. G. Harris, *Opt. Lett.* **25**, 805 (2000).
2) T. S. Rutherford, W. M. Tulloch, S. Sinha and R. L. Byer, *Opt. Lett.* **26**, 986 (2001).
3) T. Taira, J. Saikawa, T. Kobayashi and R. L. Byer, *IEEE J. Sel. Top. Quantum Electron.* **3**, 1000 (1997).
4) N. Pavel, J. Saikawa and T. Taira, *Jpn. J. Appl. Phys.* **40**, 146 (2001).

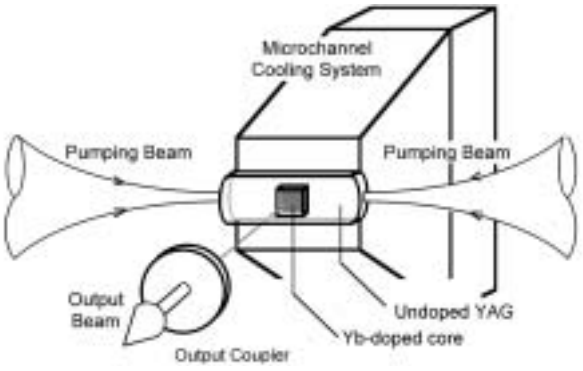

Figure 1. Schematic of the diode radial pumped composite Yb:YAG laser.

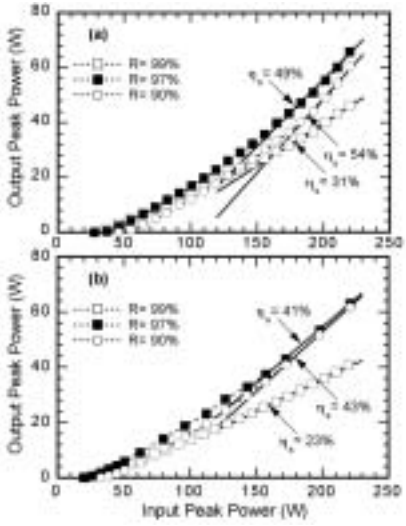

Figure 2. Output power *vs.* input power for composite Yb: YAG microchip laser with (a) crystal #A and (b) crystal #B.

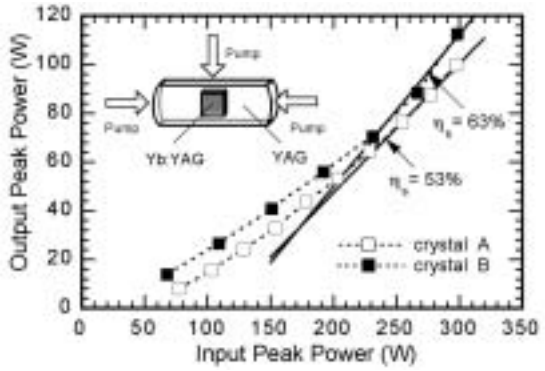

Figure 3. Performances of the microchip laser under pumping with three diodes, output coupler of 97% reflectivity.

VIII-B-3 Laser Operation with Near Quantum-Defect Slope Efficiency in Nd:YVO_4 under Direct Pumping into the Emitting Level

SATO, Yoichi; TAIRA, Takunori; PAVEL, Nicolaie[1]; LUPEI, Voicu[2]
([1]IMS and IAP-NILPRP, Romania; [2]IAP-NILPRP, Romania)

[*Appl. Phys. Lett.* **82**, 844 (2003)]

Construction of efficient solid-state lasers requires laser components able to absorb completely the pump radiation and to use it for high performance laser emission. These requirements are fulfilled by laser materials with broad and intense absorption bands that match the diode lasers emission spectrum, as well as with a high value for the product of the effective emission cross section σ_{eff} and the effective luminescence lifetime $\tau_f = \tau_{rad}\eta_{qe}$, where η_{qe} is the emission quantum efficiency. The Nd-doped crystals of the vanadate family, such as YVO_4 or $GdVO_4$, fulfill well these spectroscopic requirements.[1),2)] The Nd:YVO_4 lasers are traditionally pumped into the strongly absorbing $^4F_{5/2}$ level at 808.8 nm and this introduces a parasitic upper quantum defect (QD) between the pumping- and the emitting-laser level. The global QD in these lasers could be then reduced by elimination of this upper QD by pumping directly into the emitting level $^4F_{3/2}$. This modality of pumping was used in the first experiments to demonstrate the possibility of excitation of Nd^{3+} emission by resonant diode pumping.[3)] Recently, the pumping into the emitting level was reinvestigated for diluted Nd:YVO_4 crystals;[4)–6)] preliminary data on concentrated Nd:YVO_4 crystals were also reported.[5),6)] It was thus revealed that a suitable pump transition for Nd:YVO_4 is $^4I_{9/2}(Z_1) \rightarrow {}^4F_{3/2}(R_1)$, at 879.8 nm. The slope efficiency of the 1064-nm laser emission for both 809 and 880-nm pump was lower than the limit determined by η_{qd} for these wavelengths (0.760 and 0.827, respectively), even considering fairly large residual optical losses *L*. While for direct pumping this difference can be attributed[5),6)] to a less than unity efficiency of superposition between the pump and laser volumes η_m and to the use of uncoated crystals, in case of 809-nm pumping the possibility of a less than unity of η_p must be further checked. The aim of the present work is the improvement of laser parameters by using coated crystals and pump focusing conditions able to increase η_m. A method to determine the pump level efficiency η_p for 809-nm pumping based on pump saturation effects was developed.

The 1-μm CW laser emission of Nd:YVO_4 was investigated under end-pumping with 880-nm radiation of a Ti:Sapphire and of a diode laser. The laser crystal was a 1.0-mm thick *a*-cut plate with 1.0-at.% Nd, AR coated on both sides for 809, 880 and 1064-nm wavelengths. A plane-concave resonator of 45-mm length and 50-μm radius of the output mirror was used under Ti:Sapphire pumping. The Gaussian pump light was focused on crystal in a 50-mm diameter spot and the excitation was made with $E \| c$ crystal axis. Figure 1 shows the output power *vs.* Ti:Sapphire 880-nm input power. For a 10% transmission (T) output coupler the slope efficiency reached 80%, the threshold of emission was ~ 25-mW and for 1.0 W input power the laser emitted 0.79 W at 1064 nm. Slope efficiency of 74% and 67% resulted with T = 5 and 3%, respectively. These data give consistently round-trip residual losses L of ~ 0.9 % with η_m close of unity, and thus the difference between the obtained slope efficiency and that determined by the QD for this wavelength of pump can be fully accounted by the residual optical losses L. When the Ti:Sapphire laser wavelength was tuned to 809 nm the slope efficiency in the range of 70 to 650 mW input power was 70%, 63% and 57% for T = 10%, 5% and 3%, respectively.

Traditionally, for 809-nm pumping η_p has been considered as unity;[7)] however, other laser emission results[8)] indicate a lower value (~ 0.95) that could be, however, influenced by uncertainties in determining η_m. Here we show that η_p can be evaluated independently based on saturation effects in the pump transmission. Based on a rate equation modeling that accounts for this emission, a general equation for the dependence of the pump power on the distance *z* inside the active medium in absence of laser emission was obtained:

$$\frac{dP_{in}(z)}{dz} = -\alpha_a \frac{\pi w_p^2 \cdot I_p^{sat}}{2\beta} \times \ln\left[1 + \frac{2\beta}{\pi w_p^2 \cdot I_p^{sat}} P_{in}(z)\right] \qquad (1)$$

where $P_{in}(z)$ is the pump power, I_P^{sat} is the pump-saturation intensity, α_a is the absorption coefficient, and w_p the pump beam waist. The parameter β accounts for the mechanisms of excitation and de-excitation of the emitting level: for pumping above the emitting level (including 809-nm pumping), $\beta \equiv \eta_p$ while when pumping into the emitting level $\beta = 1 + f_2/f_0$, with f_2 and f_0 the fractional thermal population of the Stark sublevels $^4F_{3/2}(R_1)$ and $^4I_{9/2}(Z_1)$, respectively. Considering the energy level diagram of Nd:YVO_4 at the room temperature $f_0 = 0.4$, $f_2 = 0.52$ and $\beta = 2.3$.

Equation (1) integrated over the length of the crystal was used to estimate the parameter β from the fit of the measured transmission at various pump powers. In the experiments on saturation the Gaussian Ti:Sapphire radiation was focused on the 1-at.% Nd:YVO_4 crystal to a waist of 21-μm in case of 880 nm and 29-μm for 809-nm pumping. The absorption coefficients at 880 nm and

809 nm wavelengths, determined for low intensity of the Ti:Sapphire laser, were ~ 55 cm^{-1} and ~ 75 cm^{-1} respectively. In case of 809-nm pumping a good agreement was obtained for η_p = 1 (Figure 2); the inset of Figure 2 shows clearly the differences between the theoretical curves for η_p = 0.95 and 0.9 and the experimental data. At 880-nm pumping the effect of the induced emission on transmitted power at high pump intensity is evidenced by the good fit with β = 2.3.

A fiber array packed diode bars FAP-81-16C-800B laser (Coherent Co.) was next used to pump the Nd:YVO_4 crystal, in a 50-mm plane-plane resonator. A slope efficiency of 75% was obtained for T = 10% ($E||c$ pumping); the absorbed power at threshold was 0.55 W and 1.1-W output power resulted for 2.0-W absorbed power. The threshold absorbed power decreases to 0.33 and 0.16 W for T = 5 and 1%, respectively, however with a reduced slope efficiency of 69% and 28%.

In conclusion, one-micron highly efficient laser emission with 80% slope efficiency (~ 0.79 optical-to-optical efficiency) under Ti:sapphire and 75% slope efficiency relative to absorbed power under diode laser 880-nm pumping was obtained in a 1-mm thick, 1-at.% Nd:YVO_4 crystal; the first of these is close to the quantum defect limit. The pump-beam saturation effects on transmitted power under non-lasing condition indicate that η_p of the $^4F_{5/2}$ level is ~ 1.0. Directly-pumped highly Nd-doped vanadates have potential for construction of highly-efficient CW miniature lasers by using thinner active components with enhanced absorption and with extended capabilities to dissipate the heat or for scaling to higher powers; they could be also useful in the design of transversely-pumped Nd:YVO_4 lasers.

References

1) R. A. Fields, M. Birnbaum and C. L. Fincher, *Appl. Phys. Lett.* **51**, 1885 (1987).
2) T. Jensen, V. G. Ostroumov, J. P. Meyn, G. Huber, A. I. Zagumennyi and I. A. Shcherbakov, *Appl. Phys. B* **58**, 373 (1994).
3) R. Newman, *J. Appl. Phys.* **34**, 437 (1963).
4) R. Lavi, S. Jackel, Y. Tzuk, M. Winik, E. Lebiush, M. Katz and I. Paiss, *Appl. Opt.* **38**, 7382 (1999).
5) V. Lupei, N. Pavel and T. Taira, *Opt. Commun.* **201**, 431 (2002).
6) V. Lupei, N. Pavel and T. Taira, *IEEE J. Quantum Electron.* **38**, 240 (2002).
7) A. W. Tucker, M. Birnbaum, C. L. Fincher and J. W. Erler, *J. Appl. Phys.* **48**, 4907 (1977).
8) R. A. Fields, T. S. Rose, M. E. Innochenzi, H. T. Yura and C. L. Fincher, *Proc. Advanced Solid State Lasers Conf.* (Optical Society of America, Washington, D.C.), 301 (1989).

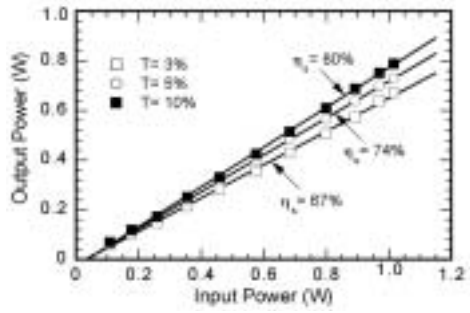

Figure 1. CW 1064-nm laser emission under 880-nm Ti: Sapphire pumping for 1-at.% Nd:YVO_4.

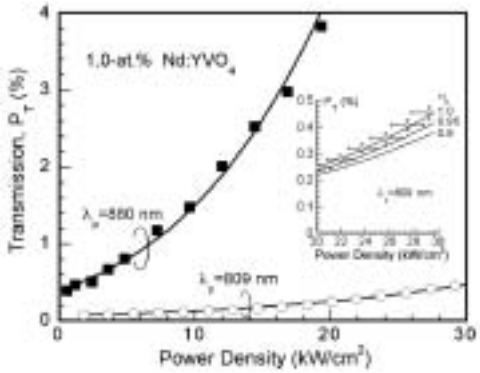

Figure 2. Transmitted power P_T *vs.* pump-beam intensity in absence of laser emission: symbols for experiments and curves from theory with β = 2.3 (880 nm) and η_p = 1 (809-nm pumping). The inset shows the fit of the 809-nm pump data with η_p = 1, 0.95, and 0.9.

VIII-B-4 High-Power Blue Generation in a Periodically Poled MgO:$LiNbO_3$ Ridge-Type Waveguide by Frequency Doubling of a Diode End-Pumped Nd:YAG Laser

PAVEL, Nicolaie[1]; SHOJI, Ichiro; TAIRA, Takunori; IWAI, Makato[2]; YOSHINO, Takeshi[2]; YAMAGUCHI, Shoichiro[2]; IMAEDA, Minoru[2]
([1]IMS and IAP-NILPRP, Romania; [2]NGK)

[*OSA, TOPS* **83**, 388 (2003)]

The $^4F_{3/2} \rightarrow {}^4I_{9/2}$ laser transition at 946 nm of Nd^{3+}:YAG opens the way for generation of continuous wave (CW) blue laser radiation that is of interest for various application, such us display technologies, obtaining of high-density optical disk systems, high-resolution printing, or biological applications. An attractive way to obtain a compact blue-light source is second-harmonic generation (SHG) by quasi-phase matching (QPM) interaction. Recently, MgO:$LiNbO_3$ (MgO:LN) was demonstrated to be a good nonlinear material for blue SHG: it presents higher resistance to photorefractive damage than LN, decreased coercive field compared with LN and a large nonlinear coefficient d_{33} ~ 25 (±2.5) pm/V.[1),2)] The key points for obtaining efficient and high-power SHG waveguide devices include strong confinement of the light wave into the waveguide, good overlap of fundamental and second-harmonic modes, prevention of nonlinear properties degradation, and maintaining of a high

optical-damage resistance, particularly in the shorter wavelength region. A CW blue power of 17.3 mW at 426 nm was demonstrated from a AlGaAs laser diode of 55-mW output power by using a MgO:LN proton-exchanged waveguide.[3] Proton-exchanged waveguides has, however some limitations, such as mode-field mismatching caused by dispersion and refractive index profiles, a trade-off between index change and non-linearity[4] and even degraded nonlinear properties.

A machining technique for processing three-dimensional waveguides[5] leads to a new waveguide technology: thus, a ridge-type waveguide QPM-SHG MgO:LN device that preserves the original performances of the nonlinear crystal was developed. CW SHG generation with 100 mW power at 412 nm using a Ti:Sapphire laser as a pumping source and with 14 mW output under diode laser pumping were demonstrated.[6] This work reports on our efforts toward scaling blue light obtained by frequency-doubling from a periodically polled MgO:LN ridge-type waveguide: using a diode end-pumped Nd:YAG laser operating at 946 nm as a fundamental source the maximum CW blue-light was 189 mW with a conversion efficiency of 49%.

A sketch of the experimental set-up is presented in Figure 1. A homemade diode-end pumped Nd:YAG laser was used in experiments. The 3-mm thick Nd:YAG crystal (1.0-at.% doping level) was AR coated for 809, 946 and 1064 nm. A 400-μm diameter, 0.22 NA fiber-coupled diode (HLU32F600, LIMO Co., Germany) was used for CW pumping. A plane-concave resonator of 30-mm length and output mirror of 100-mm radius was employed. With an output mirror of 97% reflectivity at 946 nm the laser delivered a random polarised beam of maximum 3.7 W for an absorbed power of 9.5 W in a beam characterised by a M^2 factor of 2.5. The slope efficiency was 44% with respect to the absorbed pump power. A glass plate positioned at the Brewster angle was used in order to achieve a polarised beam. For an absorbed power at 809 nm of 4.2 W the output was 1.1 W in a Gaussian beam (M^2 = 1.05). The laser spectrum, which was investigated with an Advantest Q8384 Spectrum Analyser (0.01-nm resolution), was centred at 946.2 nm and presented four longitudinal modes.

A periodically poled MgO:LN ridge-type waveguide of 8.5-mm length was used in experiments. Both the input and output surfaces were cut at 10° and AR coated at 946 nm by a SiO_2 monolayer; no coating was provided for the 473-nm wavelength. The MgO:LN ridge-type waveguide was placed on an aluminum plate whose temperature was controlled with 0.1 °C accuracy. The 946-nm radiation was varied by a rotating polarizer and focused into the waveguide with a lens of 8-mm focal length and NA = 0.55. For comparison, a Ti:Sapphire laser (Spectra Physics, Model 3900S) whose beam was characterized by M^2 ~ 1.03, was also used to pump the MgO:LN waveguide. Figure 2 presents the 473-nm blue light characteristics as a function of the 946-nm power coupled into the waveguide. The maximum blue power under Nd:YAG laser pumping was 189 mW with a conversion efficiency of 49%. If the Fresnel losses on the waveguide exit face are considered the maximum internal blue-light power is ~ 219 mW, corresponding to a conversion efficiency of ~ 57%. The measured temperature bandwidth was ΔT = 2.3 °C, in very good agreement with the predicted theoretical value of 2.35 °C. Under pumping by Ti:Sapphire laser the maximum blue power at 473-nm was 104 mW (conversion efficiency of 48%); the results were comparable with those obtained under pumping by Nd:YAG laser. The conversion efficiency saturation was attributed to the absorption of both the blue and fundamental radiations into the waveguide. Thus a slightly decrease of the phase-matching temperature with increasing of the blue output power was observed.

In conclusion, blue-light generation from a periodically polled MgO:$LiNbO_3$ ridge-type waveguide by frequency doubling of a diode end-pumped Nd:YAG laser is reported. To the authors best knowledge this is the first demonstration of such a system. The output power at 473 nm of 189 mW (internal power of 219 mW) was obtained, indicating the potential for high-power SHG of the ridge-type waveguide fabricated by ultra-precision machining.

References

1) I. Shoji, T. Kondo, A. Kitamoto, M. Shirane and R. Ito, *J. Opt. Soc. Am. B* **14**, 2268–2294 (1997).
2) A. Kuroda, S. Kurimura and Y. Uesu, *Appl. Phys. Lett.* **69**, 1565–1567 (1999).
3) T. Sugita, K. Mizuuchi, Y. Kitaoka and K. Yamamoto, *Opt. Lett.* **24**, 1590–1592 (1999).
4) K. Mizuuchi, H. Ohta, K. Yamamoto and M. Kato, *Opt. Lett.* **22**, 1217–1219 (1997).
5) T. Kawaguchi, K. Mizuuchi, T. Yoshino, J. Kondo, A. Kondo, M. Imaeda and K. Yamamoto, *Technical Digest of ISOM 2000* p. 66.
6) T. Kawaguchi, T. Yoshino, J. Kondo, A. Kondo, S. Yamaguchi, K. Noda, T. Nehagi, M. Imaeda, K. Mizuuchi, Y. Kitaoka, T. Sugita and K. Yamamoto, *Technical Digest of CLEO 2001 Conference*, 6–11 May 2001, Baltimore, USA, paper CTuI6, pp. 141–142.

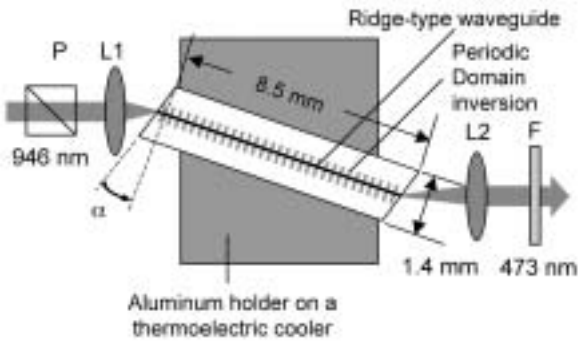

Figure 1. The experimental set-up for blue generation. P: polarizer; L1: focusing lens; L2: collimating lens; F: 946-nm cut filter.

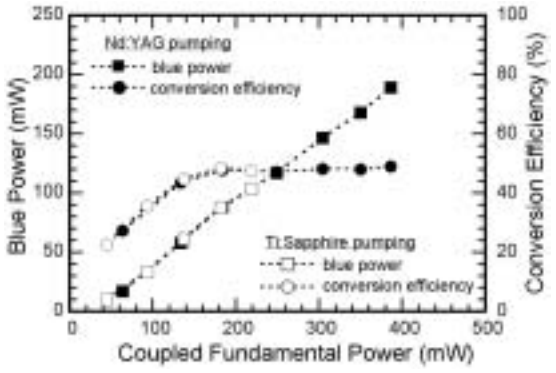

Figure 2. Blue laser characteristics vs. the 946-nm power coupled into the waveguide under pumping by Nd:YAG and Ti:Sapphire laser.

VIII-B-5 The Effect of Nd Concentration on Fundamental and Frequency-Doubled CW Laser Emission of Miniature Nd:YAG Lasers

LUPEI, Voicu[1]; PAVEL, Nicolaie[2]; TAIRA, Takunori
([1]IAP-NILPRP, Romania; [2]IMS and IAP-NILPRP, Romania)

[*CLEO/QELS 2003* paper CThM44]

This work discussed and demonstrated the benefit of using the direct pumping at 885 nm into the emitting level $^4F_{3/2}$ of concentrated Nd:YAG single crystals and ceramics for construction of efficient continuous-wave (CW) solid state lasers at the fundamental and frequency-doubled wavelength. Compared with the traditional 808-nm pumping into the strongly absorbing $^4F_{5/2}$ level, the direct pumping could improve the laser parameters (reduction of threshold and enhancement of slope efficiency) by ~ 10%, while the fraction of absorbed power transformed into heat for the 1064-nm laser emission can be diminished by ~ 30%. The reduced pump absorption of the emitting level can be compensated by using concentrated laser materials.[1)]

The laser components used in this investigation are 3-mm long Nd:YAG crystals with 1.0 or 2.4-at.% Nd and ceramics with 3.5-at.% Nd, coated as AR for 946 and 1064 nm and HT for the 808 and 885-nm wavelengths of pumping. The Gaussian radiation from a Ti:Sapphire laser was focused to a 50-μm diameter spot on the surface of the active media, for both pumping wavelengths. A plane-concave resonator of 35-mm length and output mirror of 50-mm radius was used for 1064-nm emission.

With an output mirror of 90% reflectivity the slope efficiency for the 1.0-at.% Nd sample under 885-nm pumping was 79%, close to the quantum defect limit of 83% (Figure 1). This is the largest slope efficiency reported so far for the CW Nd:YAG lasers. With increasing Nd concentration, C_{Nd} the slope efficiency diminishes slightly owing to increased residual losses: the value was 70% and 57% for the 2.4 and 3.5-at.% Nd:YAG, respectively. For the 808-nm pumping the slope efficiency for the 1.0, 2.4 and 3.5-at.% Nd:YAG components was 69%, 64%, and 52%, respectively. The best optical-to-optical efficiency in input power for 885-nm pumping is obtained with the 3.5-at.% Nd:YAG, which shows the largest absorption efficiency, while for 808-nm pumping the best results are obtained with the 2.4-at% Nd sample for which the absorption efficiency is already close to the unity. In case of 946-nm emission (output mirror of 97% reflectivity), the slope efficiency in absorbed power for the 1.0 and 2.4-at.% Nd under 885-nm pumping was 66% and 42%, respectively, while under 808-nm pumping the slope efficiency was 55% and 37%. For this wavelength of operation the increased reabsorption precludes the use of higher C_{Nd} for the single pump-pass lasers. However, as the theoretical modeling show, the direct pumping of the 946-nm emission of concentrated Nd:YAG can be much more efficient in case of multiple-pass-pumping.

The increased emission parameters at the fundamental frequency under direct pumping are expected to influence the performances of the intracavity frequency-doubling devices, such as a reduction of emission threshold and a more pronounced dependence on the absorbed pump power.[2)] This is evidenced with a end-pumped V-type frequency-doubling device for the Nd:YAG 1064-nm emission using a nonlinear LBO crystal (type I, critical phase matching, 25 °C temperature operation). A marked enhancement of the 532-nm emission in absorbed power was observed for the 1-at.% Nd:YAG crystal (Figure 2a). However, for a given input power the performances with 809-nm pumping are superior, although a strong limiting is observed for high pump powers. The green emission parameters in input power under 885-nm pumping are improved by using higher C_{Nd}, such as 2.4-at.% Nd, owing to the increased pump absorption efficiency (Figure 2b).

In conclusion, highly efficient fundamental (up to 79% slope efficiency) and frequency-doubled continuous-wave laser emission of Nd:YAG crystals and ceramics of various Nd concentration under 885-nm direct pumping with Ti:Sapphire laser is demonstrated. These results demonstrate the utility of direct pump of concentrated Nd laser materials for construction of efficient CW Nd lasers at the fundamental or doubled frequency.

References

1) V. Lupei, N. Pavel and T. Taira, *IEEE J. Quantum Electron.* **38**, 240 (2002).
2) V. Lupei, G. Aka and D. Vivien, *Appl. Phys. Lett.* **81**, 811 (2002).

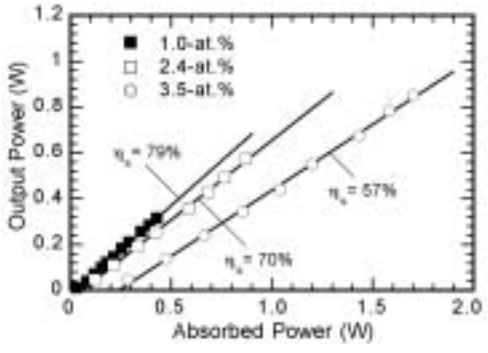

Figure 1. Output power at 1064 nm *vs.* absorbed power at 885-nm under Ti:Sapphire pumping.

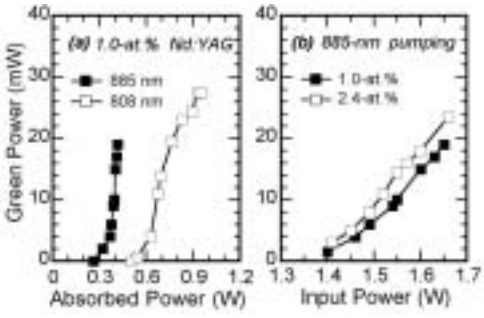

Figure 2. (a) Green power *vs.* absorbed power for the 1.0-at.% Nd:YAG crystal under 885 and 808-nm pumping, and (b) green power under 885-nm pumping for the 1.0 and 2.4-at.% Nd:YAG.

VIII-B-6 Great Reduction of Thermally-Induced-Birefringence Effect in Highly Nd^{3+}-Doped YAG Ceramics by Laser Oscillation

SHOJI, Ichiro; TAIRA, Takunori; IKESUE, Akio[1]; YOSHIDA, Kunio[2]
([1]JFCC; [2]Osaka Inst. Tech.)

[*CLEO/Europe* CA8-4-FRI (2003)]

Nd:YAG ceramics are promising materials for high-power and high-efficient microchip lasers because highly transparent and highly Nd^{3+}-doped ceramics are available with superior thermomechanical properties.[1)] We have investigated thermally-induced-birefringence effect in Nd:YAG ceramics and found that the depolarization loss of highly Nd^{3+}-doped ceramics is much larger than that of low-concentrated Nd:YAG single crystals even at the same absorbed pump power under non-lasing condition.[2)] This is mainly due to larger thermal loading, η_h, for higher Nd^{3+} concentration; η_h depends on the radiative quantum efficiency, η_r, which becomes smaller for higher Nd^{3+} concentration because of significant interaction between Nd^{3+} ions. Under lasing, however, η_h does not depend on η_r and then becomes a constant small value in an ideal case, reducing the depolarization to much smaller values than those under non-lasing. We experimentally investigated the reduction of depolarization under lasing condition.

The measurement was performed with the pump-probe measurement.[2)] A Ti:sapphire laser oscillating at 808nm was used as the pump source and a linearly polarized He-Ne laser was used as the probe. We used a 3.5at.% Nd:YAG ceramic, the thickness of which was 1.9mm, and also used a (111)-cut 3.0mm-thick 1.0at.% Nd:YAG single crystal as comparison. The laser output power as a function of the absorbed pump power for both the samples are shown in Figure 1. Lower output for the ceramic is supposed to be due to lower mode matching caused by more significant thermal-lens effect. Figure 2 shows the dependence of the depolarization on the absorbed pump power under non-lasing and lasing conditions. When lasing occurs, the depolarization of the 3.5at.% Nd:YAG ceramic reduced to 1/3 of that under non-lasing condition, which is nearly the same with that of the non-lasing single crystal. We also found that η_h is not constant even under lasing in a practical case, and the depolarization at each absorbed pump power can be estimated from the characteristics of the laser oscillation, as shown by the dotted curves in Figure 2.

In conclusion, we have experimentally verified that the depolarization of highly Nd^{3+}-doped YAG ceramics is greatly reduced by laser oscillation.

References

1) T. Taira, A. Ikesue and K. Yoshida, *OSA Trends in Optics and Photonics* **19**, 430 (1998).
2) I. Shoji, Y. Sato, S. Kurimura, V. Lupei, T. Taira, A. Ikesue and K. Yoshida, *Opt. Lett.* **27**, 234 (2002).

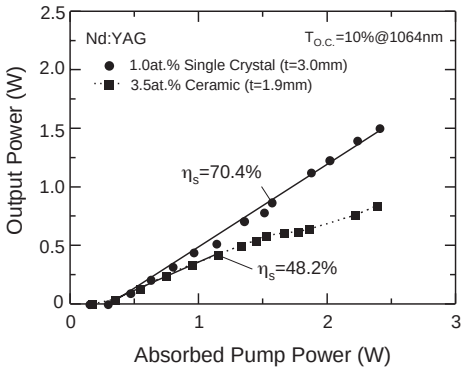

Figure 1. Laser output power as a function of the absorbed pump power for the ceramic and single-crystal.

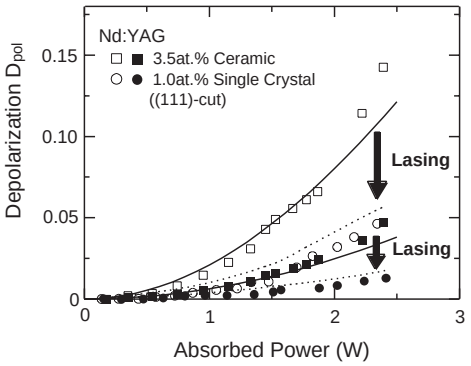

Figure 2. Dependence of the depolarization on the absorbed pump power under non-lasing and lasing conditions. The solid and dotted curves are the calculated depolarization under non-lasing and lasing conditions, respectively.

VIII-B-7 Periodical Poling Characteristics of Congruent MgO:$LiNbO_3$ Crystals at Elevated Temperature

ISHIZUKI, Hideki; SHOJI, Ichiro; TAIRA, Takunori

[*Appl. Phys. Lett.* **82**, 4062–4064 (2003)]

Quasi-phase matching (QPM) is an attractive technique for efficient nonlinear wavelength conversion, and various types of QPM devices have been demonstrated. A 5 mol% MgO-doped $LiNbO_3$ (MgO:LN) crystal has attracted much attention for the material of the QPM devices because of its higher resistance to photorefractive damage than that of non-doped LN. It has also a large nonlinear coefficient and a lower

coercive field to invert the sign of the nonlinear coefficient of the than that of non-doped LN. These features mean that MgO:LN is a suitable material for QPM devices with large cross-sections for high-power and/or short-pulse operation. However, few reports have been made on realizing bulk QPM devices by use of MgO:LN, and the maximum thickness was limited to 1mm. Here, we report the periodic poling characteristics of MgO:LN crystal at elevated temperature and demonstrate successful periodical poling of 3mm-thick MgO:LN crystals with 30 μm period.

The coercive field of MgO:LN was measured in an insulation-oil bath. An aluminum electrode of 0.2 μm thickness was prepared on the crystal surface by vacuum evaporation and photolithography. The measured coercive-field dependence on crystal temperature is shown in Figure 1. The open triangles are the estimated coercive field was measured by multipulse application totally longer than 100seconds, and the filled circles are the values obtained by applying only one high-field pulse of 1-second duration. The measured values by using 1-second pulse may have a little higher value than that by multipulse application because of the slow response time of the crystal. The coercive field decreased drastically with increasing temperature. The coercive fields at T = 250 °C were measured to be 1.2 kV/mm, which is about 1/4 compared with that for MgO:LN at room temperature(RT) and about 1/17 of that for non-doped LN at RT.

We tried to fabricate periodically poled structures of 30 μm grating period in 3-mm-thick MgO:LN at elevated temperature. At T = 170 °C, we achieved periodically poled structures with smooth surface by applying ~ 5 kV (~ 1.7 kV/mm) pulses as shown in Figure 2. Figure 2(a) shows the photograph of the *y*-face cross-section of obtained periodic structures after HF etching, and Fig. 2(b), 2(c) and 2(d) present the +*z* surface, *y*-face (expansion) and –*z* surface photographs, respectively. Periodic patterning with high aspect ratio (periodic-pattern width : crystal thickness) of 1:200 was realized.

In conclusion, we investigated the coercive field dependence on the crystal temperature for 5 mol% MgO:LN. The coercive field at 250 °C was found to reduce to about 1.2 kV/mm, which is about 1/4 of that at room temperature. We successfully fabricated periodic structures of 30 μm period with smooth surfaces in 3-mm-thick MgO:LN. The drastically reduced coercive field of MgO:LN crystals may enable us to realize much thicker QPM device than ever reported. This kind of thick QPM devices can be used as intracavity elements, and for high-power wavelength conversion, short-pulse amplification, and pulse compression.

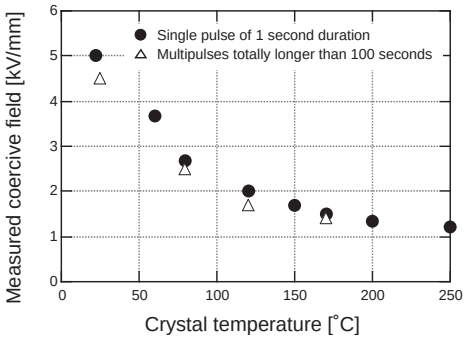

Figure 1.

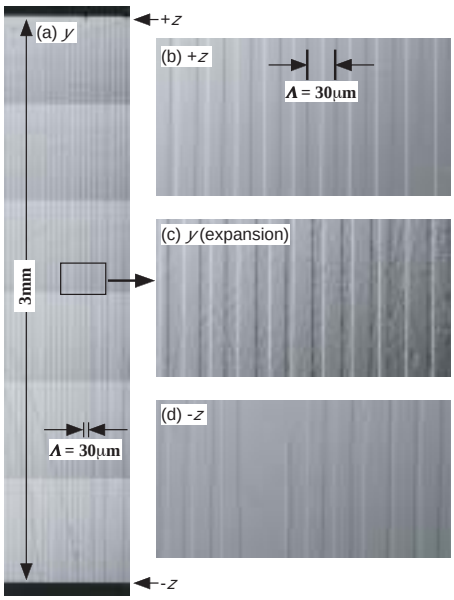

Figure 2.

VIII-B-8 Energy Transfer Processes of Nd^{3+} in Y_2O_3 Ceramic

LUPEI, Aurelia[1]; LUPEI, Voicu[1]; TAIRA, Takunori; SATO, Yoichi; IKESUE, Akio[2]; GHEORGHE, Cristian[1]
([1]Inst. Atomic Phys.; [2]JFCC)

[*J. Lumin.* **102-103**, 72–76 (2003)]

The paper presents spectroscopic and energy transfer results from the investigation of Nd^{3+}:Y_2O_3 transparent ceramics, as a new variant of a laser material. The positions of main Nd^{3+} lines (N) in ceramic Nd^{3+}:Y_2O_3, at low concentrations, are identical to those reported for single crystals. The absence of any other spectral satellites than those corresponding to Nd^{3+} pairs (M) as well as the relative intensity of M lines, show that no structural defects are present in the crystalline lattice of ceramic grains and that the distribution of Nd^{3+} ions at the available lattice sites is random. Thus, from spectroscopic and microstructural point of view, the ceramic Nd^{3+}:Y_2O_3 materials are similar to single crystals. At least two satellite lines were observed in high resolution absorption spectra and assigned to pairs of identical Nd^{3+} centers at nearest distances, C_2–C_2 pairs (8 sites at distances smaller than 4 Å) and dissimilar Nd^{3+} centers ,

C_2–C_{3i} pairs (4 sites at distances smaller than 4 Å).

The global emission decays of $^4F_{3/2}$ Nd^{3+} level at 300 K show strong concentration dependence. The decays for concentrations up to ~ 3 at% present a complex non-exponential behavior, that is interpreted in terms of a cross-relaxation process involving at least two types of interactions: a short range—probably superexchange—connected with interaction within near neighbor pairs and dipole–dipole and a migration term. Though the system contains two types of Nd^{3+} sites, no energy transfer or cross-relaxation to C_{3i} sites is considered for low concentrations since no magnetic dipole allowed transitions are involved in these processes. The efficient energy transfer for low concentrations (dipole-dipole microparameter $C_{DA} \sim 3.7 \times 10^{-39}$ cm^6 s^{-1} is ~ 20 times larger than that for Nd^{3+} in YAG[1]) and the additional transfer mechanisms at higher concentrations determines a strong drop of emission quantum efficiency with concentration and restricts the range of Nd^{3+} concentration in Y_2O_3 useful for laser emission to the range of ~ 1 at%.

Reference

1) V. Lupei, A. Lupei, S. Georgescu, T. Taira, Y. Sato and A. Ikesue, *Phys. Rev. B* **61**, 092102 (2001).

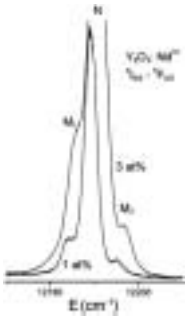

Figure 1. The absorption spectra corresponding to $^4I_{9/2} \rightarrow {}^4F_{5/2}$ (1) transition of Nd^{3+} in Y_2O_3 ceramic for 1 and 3 at%.

VIII-B-9 Second-Harmonic Nonlinear Mirror CW Mode Locking in Yb:YAG Microchip Lasers

SAIKAWA, Jiro; TAIRA, Takunori

[*Jpn. J. Appl. Phys.* **42**, L649 (2003)]

In recent years there has been great interest in sub-picosecond diode-pumped solid-state lasers with multi-watt average powers. Yb:YAG is the candidate for high power sub-picosecond lasers because it has wide emission bandwidth and large thermal conductivity. For high power sub-picosecond mode locked lasers, our approach is the second harmonic nonlinear mirror mode locking (NLM) technique. This technique is based on the second harmonic generation (SHG); thus it has no absorption losses and does not require interferometric cavity length control. In this paper we report the demonstration of a cw-pumped Yb:YAG laser that is passive mode-locked by the nonlinear mirror technique; the possibility to obtain high power sub-picosecond Yb:YAG lasers under diode laser pumping is discussed.

The experimental setup of NLM mode locked Yb:YAG laser is shown in Figure 1. A 15-at.% Yb:YAG chip (1 mm thickness) was used; the Yb:YAG crystal was sandwiched between two undoped YAG plates and is contact with a copper heatsink (~ 20 °C). The cavity length is ~ 2 m and excepting the output coupler M6, the other cavity mirrors were coated as high reflectivity around 1030 nm; moreover, the mirrors M5 and M6 were high reflectivity coated at the SH wavelength. Two LBO crystals (10 mm and 5-mm length) that were cut for type-I temperature tuned non-critical phase matching and antireflection coated for both the fundamental and SH wavelength were used. The LBO crystal was inserted into an oven whose temperature was controlled with 0.1 °C accuracy. The nonlinear mirror was composed of the LBO crystal and the output coupler M6.

In the mode locking operation (under phase-matching), the laser jumped from cw operation to self-start cw mode locking operation. The pulse duration was measured to 9 ps (5mm-LBO). This limitation of pulse width was due to bandwidth of nonlinear mirror. The pulse repetition rate was 82 MHz, and a maximum average power of 900 mW and an optical conversion efficiency of 54% were obtained.

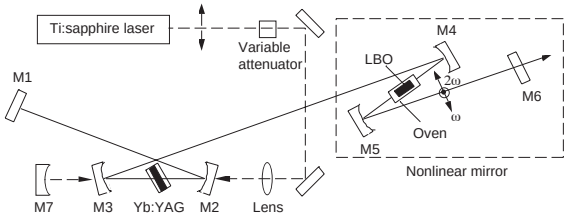

Figure 1. The cavity set up of NLM mode-locked Yb:YAG laser.

Research Center for Molecular-Scale Nanoscience

VIII-C Synthetic Approach Toward Molecular Scale Electronics

Electric properties of organic and in-organic nano structures are challenging field in material science. Those of aggregates, crystals, or polymers which are made from a large number of molecules or atoms have been well studied and established. In contrast, nano scale electronics is the forefront of science, and has been revealed gradually to have diverse phenomena such as quantum conductance, the Kondo effect, the Coulomb blockade, resonance tunneling and so on. In order to establish this field, we are synthesizing new organic and in-organic nano strucutures by using usual synthetic methods together with non-conventional lithographic technique, and measure their electric properties mainly.

VIII-C-1 Linear Functionalized Terthiophene Phenanthroline Polymer for Nanodevices

OGAWA, Takuji[1]; ENDO, Hiroaki[2]; ARAKI, Koiti[1]
([1]IMS, JST; [2]IMS and Ehime Univ.)

The development of molecular electronic devices requires the preparation of new funcional materials with suitable properties. Among them one have pursued the preparation of linear chain polymers constituted by porphyrins or ruthenium complexes that could be obtained in a controlled way. The redox and photophysical properties of those compounds are well known, such that one were atracted by the possibility of generating nanodevices by connecting a bunch or even a single strand of those polymers to a couple of nanogap electrodes. In this communication we report the synthesis and characterization of the monomer as well as the properties of the a new linear hexathiophene-phenanthroline based charge transfer polymer functionalized with $[Ru(bipy)_2(phen)]$ complexes, obtained by electropolymerization. The 1,10-phenanthroline with thiophene (tphen) and tertiophene (ttphen) radicals at the 3,8-positions were obtained by conventional Ni catalyzed coupling reactions and the complexes by reaction with $[Ru(bipy)_2(OH_2)]$ in DMF. Both complexes exhibited four reversible waves in the –1 to –2 V range assigned to the reduction of each of the bipy, phen and thiophene groups to the corresponding radical anion. In the anodic side a quite different behavior was observed. While the ttphen derivative exhibited a catalytic oxidation of ttphen ligand around 1.3 V responsible for the electropolymerization, a reversible Ru(III/II) wave was observed for the tphen derivative. One found out that the polymeric complex can be easily grown in between the nanogap electrodes. The conduction and photoconduction properties are being investigated.

VIII-C-2 Synthesis of Self-Standing Molecular Jacks Bearing Long Anchoring Arms

OGAWA, Takuji[1]; MIZUGUTI, Eisuke[2]
([1]IMS, JST; [2]IMS and Ehime Univ.)

A series of porphyrin derivatives bearing more than four lipoic acyl groups have been synthesized. The lipoic acyl group has disulfide moiety at the end of the acyl chain, and can be adsorbed to the gold surface. When rhodium metal is introduced in the center of the porphyrin, a variety of organic functional groups can be introduced as the axial group of the porphyrin plain. Thus, when the po rphyrin plain is anchored to the gold surface by the lipoic acyl groups, the axial organic functional groups will stand perpendicularly to the gold surface. We call the porphyirn part of the molecule as a "molecular jack," because a variety of molecular wires can be connected to the electrode metal surface through the molecule.

One merit of the molecular jack is that the occuping area of the molecule on the electrode surface can be controlled by changing the length of the alkyl group connecting to the lipoic acyl group. We have synthesized a tetraarylporphyrin derivative whose aryl groups are subsitituted with $(-O-(CH_2)_{11}-OCO-(CH_2)_4-C_3H_5(S–S))$ at their 3,5-positions. The distance between one S–S group to that of the oposite side is about 6 nm. Consequently the molecule will occupy circular area of about 6 nm diameter on the adsorbed metal surface. Thus when the molecules are adsorbed to the metal electrodes with the size of 60 nm × 60 nm, only 100 molecules will be present on it at the most. By reducing the number of molecules present on the electrodes, it will become much easier to discuss about the electronic properties of the individual molecules.

VIII-C-3 Synthesis and Self-Assembly of Novel Porphyrin Molecular Wires

OGAWA, Takuji[1]; KAWAO, Masahiro[2]
([1]IMS, JST; [2]IMS and Ehime Univ.)

Long π-conjugated molecular-wires have been focused much attentions because they can be used for organic conducting material, nonlinear optical material and molecular wire. The recently reported meso-meso-linked porphyrin wires were soluble in organic solvent in spite of their high molecular weight. The high solubility can be explained by the vertically crossed porphyrin π-plains to each other: because of the sterical requirement, intermolecular ππ-stacking was prevented. However at the same time because of the configuration, π-electronic conjugation was not effective, and the absorption band do not shift to the longer wavelength

even for the long oligomers. Because tunnel resistance is generally less when the molecule has lower HOMO-LUMO gap, we need molecules of lower HOMO-LUMO gap for good molecular conductor.

We prepared sub-micrometer long oligo-diethynylporphyrins by usual copper catalyzed oxidative coupling of diethynylporphyrins. The products were purified by repeating gel permeation chromatography (GPC) and analyzed by analytical GPC, absorption spectroscopy, matrix assisted laser dissorption time of flight mass spectroscopy (MALDI-TOFMS), and atomic force microscopy (AFM). Although with the MALDI-TOFMS no molecular peaks greater than ca. 100,000 could be detected, GPC and AFM data clearly indicated the presence of sub-micrometer long molecules.

These sub-micrometer π-conjugated molecules self-assembled on HOPG to make some kinds of ordered super structures as observed by AFM. When the length of the molecule is less than 100 nm and the concentration of the solution is relatively high, a regular network structure was formed in which the distance between each molecules is *ca.* 16 nm and the hight is *ca.* 0.9 nm in average. In longer molecules with less concentrated solution, a rectangular sheet structure was observed with the distance of 4 nm and the hight of 0.3 nm. Judging from the size, we postulate that in the regular network sturucture two or three molecular wires are stranded to make thicker molecular rope.

VIII-C-4 Synthesis and Characterization of Dendrimer Protected Sub-Micrometer Long Conjugated Porphyrin Wires

OGAWA, Takuji[1]; OZAWA, Hiroaki[2]
([1]IMS, JST; [2]IMS and Ehime Univ.)

Direct measurements of electronic properties of single molecule are still a challenging target of materials science, and have been reported in several papers by using scanning probe microscopic methods (SPM), or break junction methods. However, no one has ever succeeded in the electronic measurement with observing the molecules between the electrodes. One reason is that the roughness of electrodes surface, which was fabricated by usual electron beam lithographic methods, is larger than the diameter of the molecular wires, and it is difficult to observe the molecules clearly by SPM. In order to overcome the problem, we synthesized long (> 100 nm) and thick (3–5 nm) porphyrin wires surrounded by dendrimer moiety. Surrounding the wire with the dendrimer has several merits: (1) The diameter become enough large to observe them with AFM on the gapped electrodes, (2) solubility is increased, and (3) the wire may become rigid because of the steric hindrance between the adjacent moiety. Synthesized porphyrin wires were analyzed with gel permeation chromatography (GPC) and atomic force microscopy (AFM). The GPC analyses showed that the molecules have molecular weight greater than one million, which correspond to *ca.* 500 mer. The AFM images showed that the wires have the hight of *ca.* 5 nm, and in some molecules the lengths were nearly 1 μm.

VIII-D Development of Organic Semiconductors for Molecular Thin-Film Devices

Organic light-emitting diodes (OLEDs) and organic field-effect transistors (OFETs) based on π-conjugated oligomers have been extensively studied as molecular thin-film devices. Organic semiconductors with low injection barriers and high mobilities are required for highly efficient OLEDs and OFETs. Radical cations or anions of an organic semiconductor have to be generated easily at the interface with an electrode (or a dielectric), and holes or electrons must move fast in the semiconducting layer. Compared with organic *p*-type semiconductors, organic *n*-type semiconductors for practical use are few and rather difficult to develop. Recently, we found that perfluorinated oligomers are efficient electron-transport materials for OLEDs.

VIII-D-1 Oligo(2,6-Anthrylene)s: Acene-Oligomer Approach for Organic Field-Effect Transistors

ITO, Kaname; SUZUKI, Toshiyasu; SAKAMOTO, Youichi; KUBOTA, Daisuke[1]; INOUE, Youji[1]; SATO, Fumio[1]; TOKITO, Shizuo[1]
([1]NHK Sci. Technical Res. Labs.)

[*Angew. Chem., Int. Ed.* **42**, 1159–1162 (2003)]

Oligo(2,6-anthrylene)s (**2A** and **3A**) and their dihexyl derivatives (**DH-2A** and **DH-3A**) have been synthesized by the Suzuki coupling using palladium catalysts. Organic field-effect transistors (OFETs) of these anthracene oligomers were fabricated on SiO_2/Si substrates by high-vacuum evaporation. OFETs with **2A** exhibited FET activity, and the hole mobilities ranged from 0.0031 to 0.013 $cm^2V^{-1}s^{-1}$. The oligomer **3A** showed even higher mobilities (0.064–0.072 $cm^2V^{-1}s^{-1}$). Field-effect mobilities of **DH-2A** were greater than 0.1 $cm^2V^{-1}s^{-1}$. The highest mobilities (0.18 $cm^2V^{-1}s^{-1}$) were observed in **DH-3A** OFETs. X-ray diffraction studies on the films indicated a high degree of lamellar ordering and crystallinity.

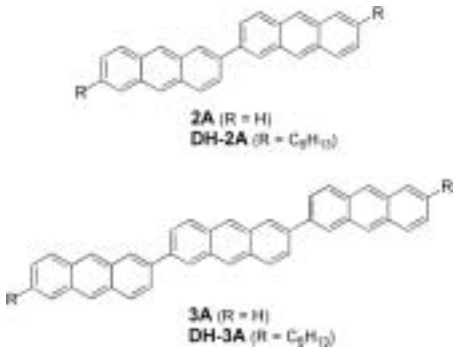

Figure 1. Structures of anthracene oligomers.

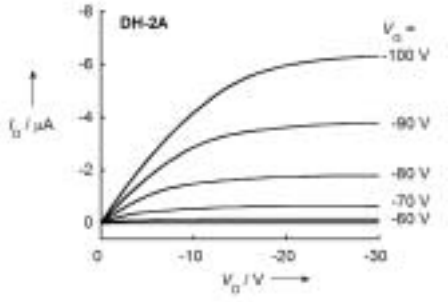

Figure 2. Drain current (I_D) *vs* drain voltage (V_D) as a function of gate voltage (V_G) for an OFET with **DH-2A** (T_{sub} = 70 °C). Channel length L = 100 μm and channel width W = 1 mm (W/L = 10).

VIII-D-2 Color Tunable Organic Light-Emitting Diodes Using Pentafluorophenyl-Substituted Iridium Complexes

TSUZUKI, Toshimitsu[1]; SHIRASAWA, Nobuhiko; SUZUKI, Toshiyasu; TOKITO, Shizuo[1]
([1]NHK Sci. Technical Res. Labs.)

[*Adv. Mater.* **15**, 1455–1458 (2003)]

Novel iridium complexes with perfluorophenyl-substituted phenylpyridine ligands have been developed. The figure shows the photoluminescence (PL) spectra of four complexes in the doped films. By changing the position of substitution, the peaks in the PL spectra are tuned in the wavelength region 513–578 nm. Light-emitting diodes using these complexes as the emitting material show an external quantum efficiency of 10–17%.

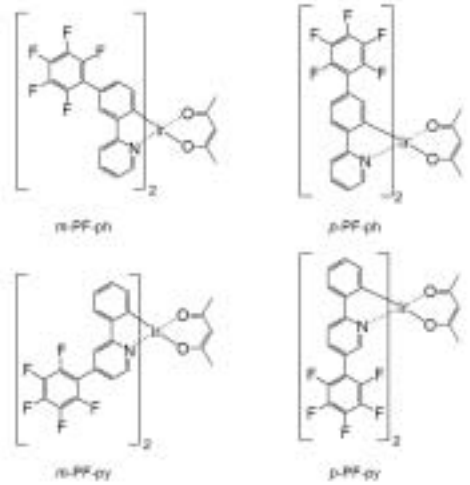

Figure 1. Structures of iridium complexes.

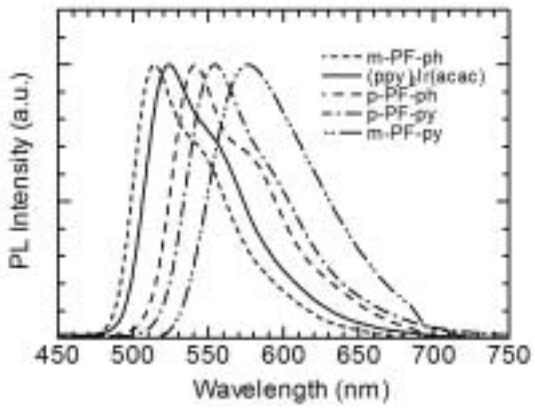

Figure 2. PL Spectra for films of the complexes (6%) doped in CPB.

VIII-E Field-Effect Transistors with Organic Semiconductors

Considerable attention has recently focused on organic field-effect transistors (OFET) because of their potential use in low-cost flexible electronic devices. In order to improve output characteristics, carrier transport in organic semiconductors is the most important subject to be elucidated.

VIII-E-1 Carrier Transport in Field-Effect Transistors Based on Single-Crystalline Wires of Bis-(1, 2, 5-thiadiazolo)-*p*-Quinobis(1, 3-dithiole) (BTQBT)

FUJIWARA, Eiichi; TAKADA, Masaki[1]; YAMASHITA, Yoshiro[2]; TADA, Hirokazu
([1]GUAS; [2]Tokyo Inst. Tech.)

We prepared single-crystalline wires of bis(1, 2, 5-thiadiazolo)-*p*-quinobis(1, 3-dithiole), whose ends were anchored to the drain and source electrodes of bottom-contact-type field-effect transistors. Figures 1 shows the SEM image of BTQBT wires grown on the substrates at 360 K. Molecular crystalline wires bridge the gaps between electrodes. It is noted that wires are anchored selectively to the electrodes and no aggregates exist on SiO_2 surface under appropriate growth conditions. Figure 2 shows the temperature dependence of the field-effect mobilities of the devices composed of nanowires and small grains in the temperature range from 5 K to 300 K. The tunnel transport and thermally activated hopping were found to be dominant at $T < 30$ K and 30 K $< T <$ 150 K, respectively, in both devices. While hopping behavior was still dominant in the device of small grains at $T >$ 150K, the mobility of wires varied as $T^{-1.3}$, indicating that phonon scattering governed carrier transport in single-crystalline wires.

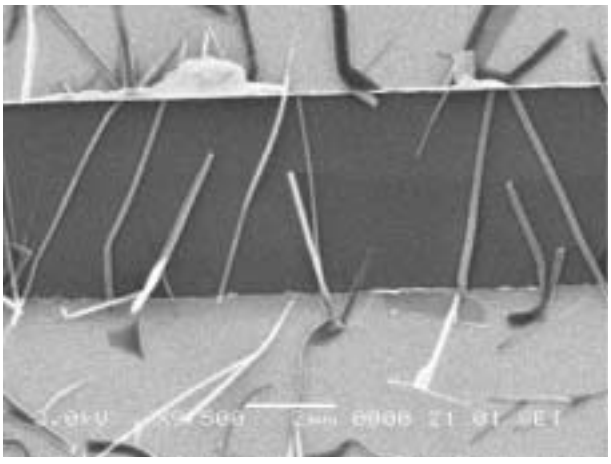

Figure 1. SEM image of BTQBT wires on FET electrodes with spacing of 5 μm.

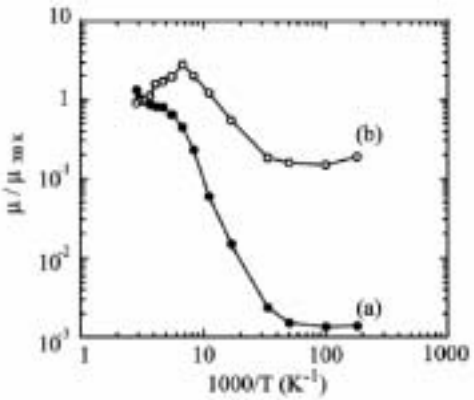

Figure 2. Temperature dependence of field-effect mobilities of small grains (a) and wires (b).

VIII-E-2 Field-Effect Transistors of $F_{16}CuPc$ with Bottom- and Top-Contact Electrodes

MINARI, Takeo[1]; FUJIWARA, Eiichi; TAKADA, Masaki[2]; TADA, Hirokazu; NEMOTO, Takeshi[1]; ISODA, Seiji[1]
([1]Kyoto Univ.; [2]GUAS)

Output characteristics of organic field-effect transistors depend strongly upon device structures. We have prepared bottom- and top-contact FET devices based on hexadecafluoro-copperphthalocyanine ($F_{16}CuPc$) films and studied electrical properties. It was found that electron mobilities of the top contact FETs were higher than those of the bottom contact FETs probably due to the difference in electric field distribution. Electron mobility of top contact FETs increased with increasing grain size of $CuPcF_{16}$ films, but large grains cause lower mobility owing to poor contact at the interface between the electrodes and the organic film in the bottom contact FETs. The FET with thick $CuPcF_{16}$ films resulted in the higher mobility in the bottom contact FETs because of less influence of air. In top contact FET, however, the thicker film gave rise to the less drain current because of the increase of resistance between source electrode and accumulation layer.

VIII-F Molecular Assemblies on Silicon Surfaces *via* Silicon-Carbon Covalent Bonds

Preparation of molecular assemblies on inorganic semiconductors such as silicon and germanium has received a growing interest because of their potential application to stable regist for nano-patterning. We have prepared organic monolayers on silicon by wet process and studied film structures with IR and AFM.

VIII-F-1 Molecular Conformation of *n*-Alkyl Monolayers Covalently Bonded to Si(111) Probed by Infrared-Visible Sum-Frequency Spectroscopy

ISHIBASHI, Taka-aki[1]; ARA, Masato[2]; TADA, Hirokazu; ONISHI, Hiroshi[1]
([1]KAST; [2]GUAS)

[*Chem. Phys. Lett.* **367**, 376–381 (2003)]

Infrared-visible sum-frequency spectra of *n*-alkyl (C_nH_{2n+1}; n = 10–13, 18) monolayers anchored on the Si(111) surface through a Si–C covalent bond were measured for the C–H stretch region. Spectral shapes exhibited azimuthorientation dependence compatible with the C_{3v} symmetry of the substrate as shown in Figure 1, indicating that the monolayers were epitaxially constructed on the substrate. Three methyl bands dominated each spectrum, and two-weak methylene bands were identified. Two distinct intensity patterns of the methyl bands were observed depending on n as shown in Figure 2. The observed spectra were interpreted with reference to reported molecular models of the monolayer that consist of alkyl chains with an all-trans head part and a twisted stem.

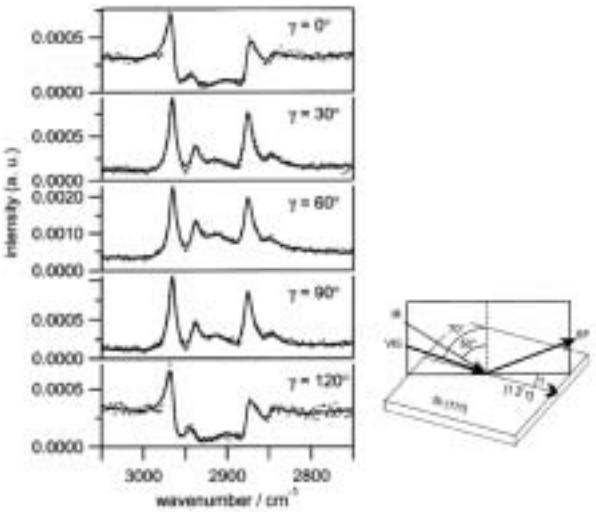

Figure 1. Azimuth dependence of SF spectra of tridecyl ($C_{13}H_{27}$) monolayer on Si(111). The spectra were measured at room temperature.

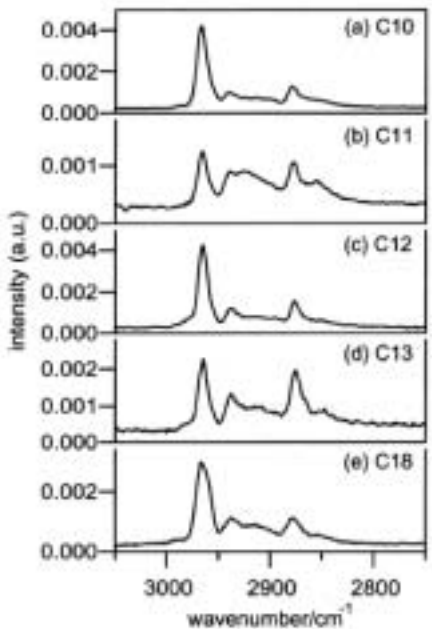

Figure 2. SF spectra of *n*-alkyl (C_nH_{2n+1}; n = 10–13, 18) monolayers on Si(111) measured at the azimuth $\gamma = 60°$.

VIII-F-2 Study on Phase Transition of Alkyl-Monolayers Anchored Covalently to Silicon by Temperature Dependent ATR-FT-IR

YAMADA, Ryo; ARA, Masato[1]; TADA, Hirokazu
([1]GUAS)

The phase behavior of alkyl-monolayers formed on Si(111) surface was investigated by an attenuated total reflection Fourier transform infra-red spectroscopy from room temperature to 590 K (Figure 1). A continuous disordering process of the monolayer was indicated from the gradual peak shifts toward higher frequency in C–H stretching modes with small decrease in the peak intensities as temperature was increased to 440 K. The rapid decrease in peak intensity was observed above 440 K. The observed changes in the spectrum were reversible by 440 K while the peak intensity was decreased and peak position became higher when the substrate was cooled to room temperature after heated above 440 K, indicating the destruction of the monolayer above 440 K. The temperature limit for the reversible phase transition was much higher than that for alkanethiol monolayer on Au(111) surface (*ca.* 350K), showing that the monolayer formed by Si–C covalent bond was more stable than that of alkanethiols on Au(111) surface due to the stronger anchoring of the molecules to the substrate.

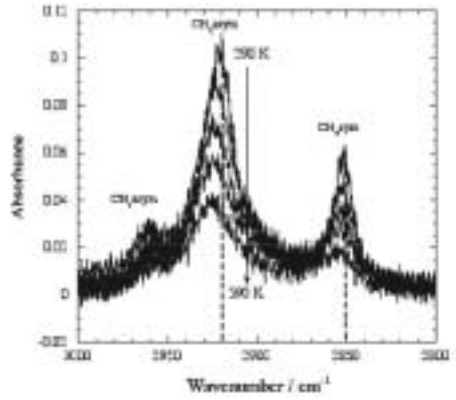

Figure 1. Temperature dependent ATR-FT-IR spectra in the C–H stretching region of octadecene-monolayer on Si(111) surface.

VIII-F-3 Friction Force Microscopy Using Silicon Cantilevers Covered with Organic Monolayers *via* Silicon-Carbon Covalent Bonds

ARA, Masato[1]; TADA, Hirokazu
([1]GUAS)

[*Appl. Phys. Lett*. **83**, 578–580 (2003)]

Cantilevers covered with hydrocarbon (CH) and fluorocarbon (CF) monolayers *via* Si–C covalent bonds were prepared and used for adhesion force measurements and friction force microscopy of the surface patterned also with CH and CF areas. The adhesion and friction forces on CF areas were larger than those on CH areas, especially using CF cantilevers as shown in Figure 1. Large polarizabilities of CF molecules compared to CH molecules are found to enhance the contrast in adhesion and friction images. The cantilevers covered with organic monolayers *via* covalent bonds are useful for chemical force microscopy with contact and noncontact mode atomic force microscopy in various atmospheres since the interface between molecules and cantilevers is thermally and chemically stable.

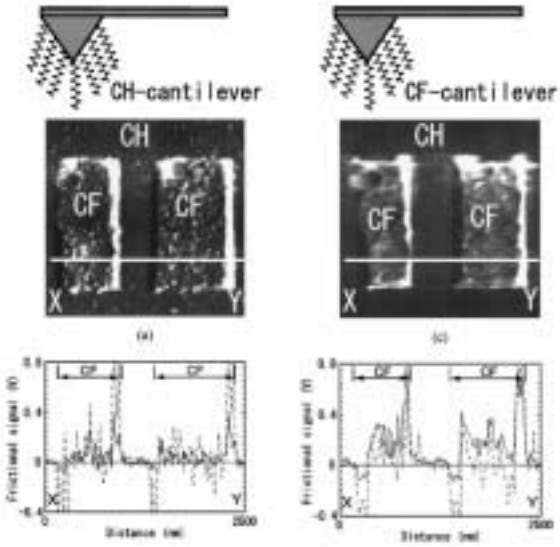

Figure 1. FFM images (a) and (c) (2.5 mm × 2.5 mm) and the friction profiles (b) and (d) of the patterned surface on Si(111) with a CH (a, b) and a CF cantilever (c, d). Spring constants of both cantilevers were 0.6 N/m. Typical loads applied were 30 nN. Solid curves and dashed curves were the profiles measured in air and *in vacuo*, respectively.

VIII-G Development of Precisely-Defined Macromolecules and Their Organization on Substrate Surfaces for Planar Molecular-Scale Electronics Circuits

The concept of molecular-scale electronics is now realized for individual components such as wire, diode, switch, and memory cell, but the fabrication of complete molecular-scale circuits remains challenging because of the difficulty of connecting molecular modules to one another. Molecular monolithic technology, which integrates the wiring, transistors and the required passive elements on a single macromolecule, has been proposed as a promising solution to this problem. In this project we have been trying to establish both the architecture of this novel class of macromolecules and the protocols for their purposive organization on metal/semiconductor substrate surfaces.

VIII-G-1 Characterization of Electronic Properties of Molecular Enamel Wires

TANAKA, Shoji

The precisely-defined "insulated molecular wire," in which rigid insulators are placed around a π-conjugated backbone except the "electrical connections," is one of the key modules for realizing ultra-dense molecular-scale electronic circuits. The well known approach to this special class of molecular wire is based on the supramolecular complex between π-conjugated oligomers and cyclodextrin molecules. As an alternative approach, we have proposed "molecular enamel wire" concept, in which the insulator mantle is covalently bonded to the backbone. The stability of insulator-attachment of molecular enamel wire will be superior to that of supramolecular wire due to the intrinsic toughness of a covalent bond. So far, we have established the synthetic approaches to molecular enamel wires based on building blocks **1** (Figure 1). Here we report the effects of the insulator mantles on electronic behaviors of these molecular enamel wires.

Figure 2 shows the absorption spectra of the vacuum-deposit thin films of oligomers **2**–**5** on quartz substrate as well as those in THF. Generally photopysical process of a π-conjugated molecule in solid state is complicated due to the intermolecular π-π interactions. The electronic spectra of the thin film of non-insulated oligothiophenes **2**–**3** are apparently dissimilar to those in the THF solution. In contrast, the thin film spectra of insulated oligothiophenes **4**–**5** are nearly identical to the THF solution spectra. These results indicate that the intermolecular π-π interactions are efficiently prevented by the insulator mantle of **4**–**5**. This conclusion is supported by the electrochemical data. Typical cyclic voltammograms of insulated and non-insulated α-12T derivatives **6**–**7** are shown in Figure 3. The voltammogram of non-insulated α-12T **6** is broad and ill-defined in contrast to that of insulated α-12T **7**, where three reversible waves are obtained. In general the ill-resolved cyclic voltammogram of long oligothiophenes has its origin in i) adsorption of charged species on the electrode surface and/or ii) π-complex formations such as "π dimer" and "dimer radical ion." Therefore the reversible electrochemical behavior of insulated α-12T **7** can be attributed to the steric inhibitions of adsorption and/or complex formation *via* π-system of the oligomers by the insulator mantle.

In conclusion these experimental data clearly demonstrate the availability of our "molecular enamel wire" concept in molecular-scale engineering.

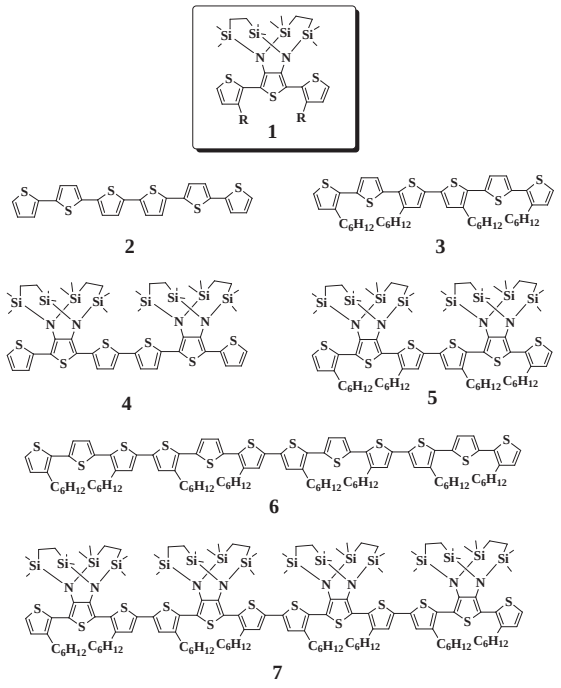

Figure 1. Molecular Structure of oligomers.

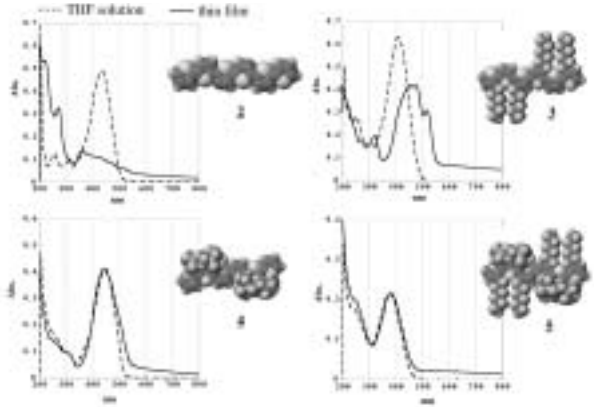

Figure 2. UV/Vis spectra of oligomers.

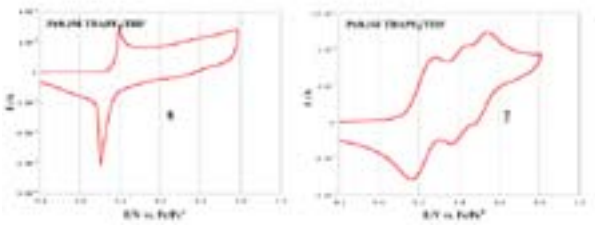

Figure 3. Cyclic voltammograms of oligomers.

VIII-G-2 Combined Spectroscopic and Theoretical Study of Narrow-Bandgap Heterocyclic Cooligomers Containing Alternating Aromatic-Donor and *o*-Quinoid-Acceptor Units

RUIZ DELGADO, Mari Carmen[1]; HERNÁNDEZ, Víctor[1]; LÓPEZ NAVARRETE, Juan T.[1]; TANAKA, Shoji; YAMASHITA, Yoshiro[2]
([1]Univ. Malágo.; [2]Tokyo. Inst. Tech.)

In this paper we analyze, with the help of Density Functional Theory calculations, the relationship between the molecular structure and the optical and vibrational properties of two narrow-bandgap π-conjugated cooligomers containing an alternating sequence of aromatic-donor and *o*-quinoid acceptor units. The optimized molecular geometries of these cooligomers reveal that short inter-ring S···N contacts occur in their minimum-energy structure between the two types of constituiting units, and that the resulting rigid coplanar arrangement of the rings enhances the degree of π-conjugation and lowers the bandgap.

VIII-G-3 Electrochemical Synthesis and Properties of Poly[1,4-bis(*N*-pyrrolylalkoxy)benzene]s with a Three-Dimentional Crosslinked Structure

ONO, Katsuhiko[1]; YAMADA, Satsuki[1]; OHKITA, Masakazu[1]; SAITO, Katsuhiro[1]; TANAKA, Shoji; HANAICHI, Takamasa[2]
([1]Nagoya Inst. Tech.; [2]Hanaichi UltraStruc. Res. Inst.)

[*Chem. Lett.* 516–517 (2003)]

The title polymers, which were composed of π-conjugated pyrroles and dialkoxybenzene crosslinkers, were prepared by electrochemical polymerization to afford amorphous thin films, which were characterized by cyclic voltammetry (CV), scanning electron microscope (SEM), and redox stability.

VIII-H Development of Novel Heterocyclic Compounds and Their Molecular Assemblies for Advanced Materials

Heterocycles containing sulfur and/or nitrogen atoms are useful as components of functional materials since heteroatoms in their rings are helpful to stabilize ions or ion-radical species, and extended π-conjugation decreases Coulombic repulsion. In addition intermolecular interactions caused by heteroatom contacts can be expected to form novel molecular assemblies. In this project new electron acceptors, donors, and donor-acceptor compounds based on heterocycles such as 1,2,5-thiadiazole and 1,3-dithiole were synthesized and their properties including those of the charge-transfer complexes or ion-radical salts were investigated. Unique crystal structures were constructed by using weak intermolecular interactions such as hydrogen bonding or heteroatom contacts.

VIII-H-1 Non-Planar BEDT-TTF Derivatives Fused with Tetrahydrofuran Rings Affording Cation Radical Salts with Unusual Crystal Structures

YAMASHITA, Yoshiro[1]; TOMURA, Masaaki; IMAEDA, Kenichi[2]
([1]IMS and Tokyo Inst. Tech.; [2]IMS and Chubu Univ.)

[*Mol. Cryst. Liq. Cryst.* **380**, 203–207 (2002)]

The title non-planar electron donors **1** and **2** were prepared by the several steps involving the addition reaction of oligo(1,3-dithiole-trithione) with 2,5-dihydrofuran. They afforded the cation radical salts as single crystals whose unusual crystal structures were revealed by X-ray analysis.

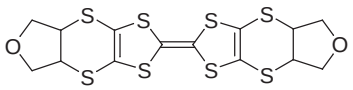

1

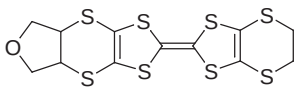

2

VIII-H-2 Synthesis and Characterization of New π-Conjugated Molecules Containing Bis(ethynylpyridine) Units with a Benzothiadiazole Spacer

AKHTARUZZAMAN, Md.[1]; TOMURA, Masaaki; ZAMAN, Md. Badruz[2]; NISHIDA, Jun-ichi[1]; YAMASHITA, Yoshiro[3]
([1]Tokyo Inst. Tech.; [2]IMS and Steacie Inst. Mol. Sci.;

[3]IMS and Tokyo Inst. Tech.)

[*J. Org. Chem.* **67**, 7813–7818 (2002)]

Three novel 4,7-bis(*n*-pyridylethynyl)-2,1,3-benzothiadiazoles (*n* = 2, 3 and 4) were synthesized by using the Sonogashira cross-coupling reaction of 4,7-dibromo-2,1,3-benzothiadiazole with the corresponding ethynylpyridines in the presence of a Pd(II) catalyst. The viologen analogues were also prepared by methylation of pyridyl nitrogen atoms. X-ray structure analysis of these compounds revealed the linear molecular structures with unusual columnar crystal structures. Insertion of a benzothiadiazole moiety into the acetylene-pyridine skeleton brings about a large increase in electron affinity and the bispyridyl compounds obtained here show high fluorescence quantum yields.

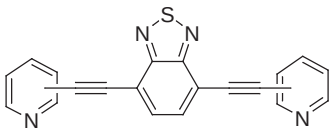

2,2'-dipyridyl, 3,3'-dipyridyl, 4,4'-dipyridyl

VIII-H-3 Preparation and Structures of Dication Salts of Phenyl Substituted TTF Vinylogues

YAMASHITA, Yoshiro[1]; TOMURA, Masaaki
([1]IMS and Tokyo Inst. Tech.)

[*J. Solid State Chem.* **168**, 427–432 (2002)]

Some TTF vinylogues **1a-l** containing phenyl groups at the vinyl positions were synthesized. The redox properties were investigated by cyclic voltammograms, showing that they are strong electron donors and the Coulomb repulsion is decreased in the dication states. Some of the donors afforded their dication salts as single crystals by electrochemical oxidation or the reaction with $CuCl_2$. X-ray structure analysis has revealed that the dication molecules have structures with planar TTF vinylogue units and twisted phenyl groups. The crystal structures are unusual to avoid the steric interactions of the phenyl groups.

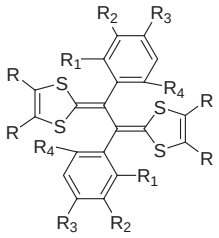

1

	R,R	R_1	R_2	R_3	R_4
1a	$(CH{=}CH)_2$	H	H	H	H
1b	$(CH{=}CH)_2$	F	H	H	F
1c	$(CH{=}CH)_2$	H	H	Cl	H
1d	$(CH{=}CH)_2$	CN	H	H	H
1e	$(CH{=}CH)_2$	H	H	CN	H
1f	$(CH{=}CH)_2$	OCH_2O		H	H
1g	SCH_2CH_2S	F	H	H	F
1h	SCH_2CH_2S	Cl	H	H	H
1i	SCH_2CH_2S	CN	H	H	H
1j	SCH_2CH_2S	H	H	CN	H
1k	SCH_2CH_2S	OCH_2O		H	H
1l	H, H	F	H	H	F

VIII-H-4 Unsymmetrical Tetrathiafulvalene with a Fused 1,2,5-Thiadiazole Ring and an Ethylenedioxy Group

TOMURA, Masaaki; YAMASHITA, Yoshiro[1]
([1]IMS and Tokyo Inst. Tech.)

[*Acta Crystallogr., Sect. E* **59**, o145–o147 (2003)]

In the crystal structure of the title compound, 4,5-ethylenedioxy[1,2,5]thiadiazolotetrathiafulvalene, $C_8H_4N_2O_2S_5$, a large number of short intermolecular S···S contacts are observed [3.519(5)–3.610(5) Å]. The molecules stack along the *c* axis in a face-to-face fashion.

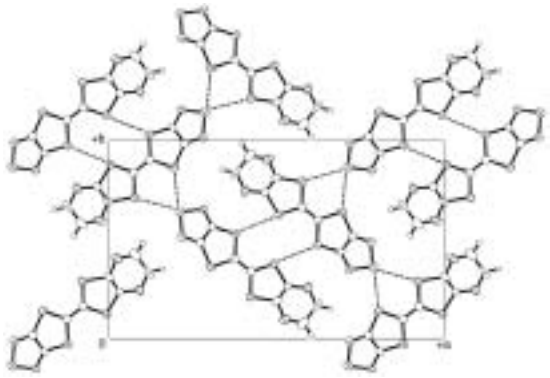

Figure 1. Packing diagram of the title compound viewed along the *c* axis. Dotted lines indicate the short intermolecular S···S contacts.

VIII-H-5 Novel Electron Acceptors Containing Nitrogen, Sulfur-Heterocyclic Units

YAMASHITA, Yoshiro[1]; SUZUKI, Kazuharu[2]; TOMURA, Masaaki
([1]IMS and Tokyo Inst. Tech.; [2]IMS and Inst. Res. Innov.)

[*Synth. Met.* **133-134**, 341–343 (2003)]

A tetracyanodiphenoquinodimethane (TCNDQ) analog **1** containing fused thiadiazole rings is a stronger electron acceptor than tetra-cyanoquinodimethane (TCNQ). The single crystals of this TCNDQ analog were found to exhibit semiconductive behaviors as a single component whose structures were revealed by X-ray structure analysis. The anion radical salts with Et_4N and Me_4P ions were obtained as single crystals by electrochemical reduction. They are 1:1 salts and showed semiconductive behaviors. The structures include tape-like networks formed by S···N contacts. Furthermore, one of the benzothiadiazole rings was replaced with a thiophene unit to give new π-extended quinonoid acceptors **2** which are highly polarized and exhibit their absorption maxima above 500 nm.

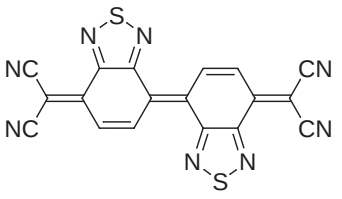

1

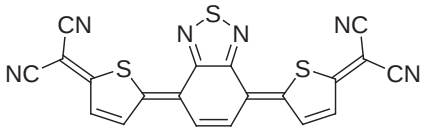

2

VIII-H-6 Linear Molecules with Ethynylpyridine and Bisbenzothiadiazole Units

AKHTARUZZAMAN, Md.[1]; TOMURA, Masaaki; NISHIDA, Jun-ichi[1]; YAMASHITA, Yoshiro[2]
([1]Tokyo Inst. Tech.; [2]IMS and Tokyo Inst. Tech.)

[*Synth. Met.* **137**, 873–874 (2003)]

7,7'-Bis(pyridylethynyl)-4,4'-bis(2,1,3-benzothiadiazole) derivatives were synthesized using the Sonogashira reaction. X-ray crystallographic analysis of the 4,4'-dipyridyl derivative revealed the linear molecular structure with an unusual tape-like crystal structure. They show high electron affinity and fluorescence with large Stokes shifts. The viologen analogues were also prepared by methylation of the pyridyl nitrogen atoms.

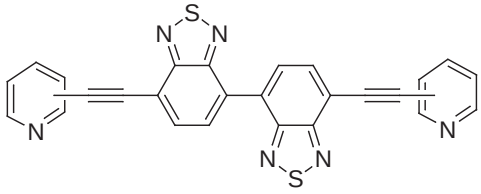

3,3'-dipyridyl, 4,4'-dipyridyl

VIII-H-7 Hydrogen Bonding Networks Consisted of Conjugation-Extended 4,4'-Bipyridines and Chloranilic Acid

AKHTARUZZAMAN, Md.[1]; TOMURA, Masaaki; TAKAHASHI, Kazuko[2]; NISHIDA, Jun-ichi[1]; YAMASHITA, Yoshiro[3]
([1]Tokyo Inst. Tech.; [2]Tohoku Univ.; [3]IMS and Tokyo Inst. Tech.)

[*Supramol. Chem.* **15**, 239–243 (2003)]

Hydrogen-bonding networks of π-extended 4,4'-bipyridines, 2,5-di(4-pyridyl)thiophene **1**, 2,5-di(4-pyridyl)furan **2** and 1,4-di(4-pyridyl)benzene **3** with 2,5-dichloro-3,6-dihydroxy-1,4-benzoquinone (chloranilic acid, **CA**) have been investigated. The dipyridyl compounds afforded three complexes, (dication of **1**)·(monoanion of **CA**)$_2$, (dication of **2**)·(dianion of **CA**)·(MeOH) and **3**·(dication of **3**)·(dianion of **CA**)·$(H_2O)_6$ with **CA**. X-ray structure analyses revealed the formation of unusual molecular tape and sheet structures involving N–H···O, O–H···O, C–H···O and N–H···N hydrogen bonds, where the aromatic spacer groups play an important role in constructing the unique crystal structures.

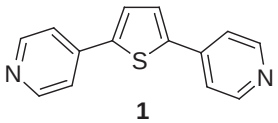

1

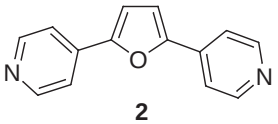

2

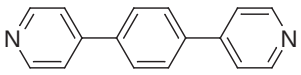

3

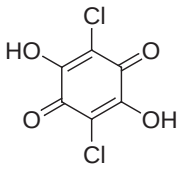

CA

VIII-I Green and Risk-Free Catalysis

Catalytic organic transformations under mild, safe, and green conditions is an important goal in synthetic organic chemistry. We recently reported that several palladium-catalyzed reactions, including π-allylic substitution, carbonylation, the Heck reaction, and Suzuki-Miyaura cross-coupling, took place in water by use of palladium-phosphine complexes bound to an amphiphilic polystyrene-poly(ethylene glycol) graft copolymer (PS-PEG) resin. Rhodium-catalyzed hydroformylation, cyclotrimerization of alkynes, and Michael-type addition of arylboronic acids were also found to proceed smoothly in water. Here we wish to report that Heck reaction, Sonogashira reaction, Wacker reaction were successfully examined in water by use of PS-PEG resin-supported transition metal complexes.

VIII-I-1 Heck Reaction in Water with Amphiphilic Resin-Supported Palladium-Phosphine Complexes

UOZUMI, Yasuhiro; KIMURA, Tsutomu

[*Synlett* 2045–2048 (2002)]

The Heck reaction of various aryl halides and alkenes took place in water in the presence of an amphiphilic polystyrene-poly(ethylene glycol) resin-supported palladium-phosphine complex to give the corresponding styrene derivatives in quantitative yields.

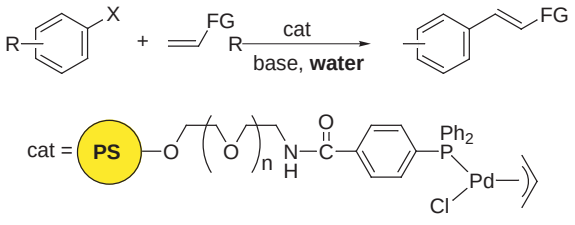

Scheme 1.

VIII-I-2 The Sonogashira Reaction in Water with an Amphiphilic Resin-Supported Palladium-Phosphine Complex under Copper-Free Conditions

UOZUMI, Yasuhiro; KOBAYASHI, Yukinari

[*Heterocycles* **59**, 71–74 (2003)]

The Sonogashira reaction of aryl halides with terminal alkynes was catalyzed by an amphiphilic polystyrene-poly(ethylene glycol) (PS-PEG) resin-supported palladium-phosphine complex in water to give the corresponding aryl-substituted alkynes in high yields under copper-free conditions. Reaction of *o*-iodophenol with terminal alkynes under Sonogashira conditions gave benzofuran derivatives in one step.

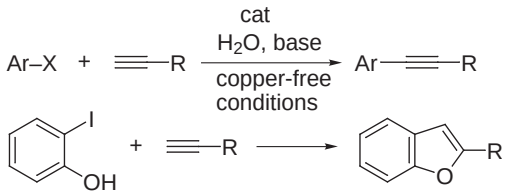

Scheme 1.

VIII-I-3 Polymer-Supported 2,2'-Bis(oxazolin-2-yl)-1,1'-Binaphthyls (boxax): Immobilized Chiral Ligands for Asymmetric Wacker-Type Cyclizations

HOCHE, Heiko; UOZUMI, Yasuhiro

[*Synlett* 2049–2053 (2003)]

Homochiral 2,2'-bis(oxazolin-2-yl)-1,1'-binaphthyl (boxax) ligands were anchored on various polymer supports including PS-PEG, PS, PEGA, and MeO-PEG *via* selective monofunctionalization at the 6-position of the binaphthyl backbone. Palladium(II) complexes of the supported boxax ligands catalyzed Wacker-type cyclization of 2-(2,3-dimethyl-2-butenyl)phenol to give 2-methyl-2-isopropenyl-2,3-dihydrobenzofuran with up to 96% ee.

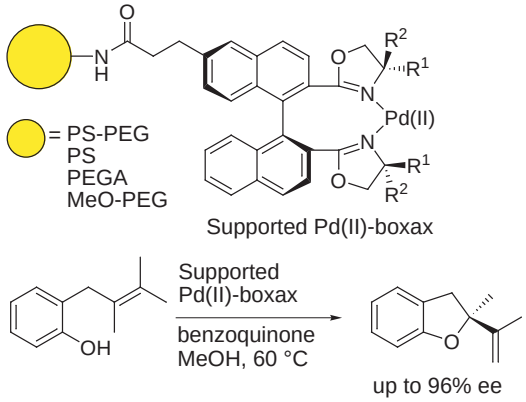

Scheme 1.

VIII-J Designing Artificial Photosynthesis at Molecular Dimensions

Photosynthesis is one of the finest piece of molecular machinery that Nature has ever created. Its ultrafast electron transfer and following well-organized sequence of chemical transformation have been, and will continue to be, challenging goals for molecular scientists. We are trying to mimic the function of photosynthesis by assembling molecular units that perform individual physical/chemical action. The molecular units include porphyrins, redox active organic molecules, and transition metal complexes. Our ultimate goal is to design artificial molecular systems that effect multiple chemical reactions triggered by light on the basis of molecular rationale.

VIII-J-1 Photooxidation of Alcohols by a Porphyrin/quinone/TEMPO System

NAGATA, Toshi; ITO, Hajime; NAGASAWA, Takayuki

Photoinduced electron transfers involving porphyrins are widely studied, but utilizing the high-energy radical ion pairs for driving chemical reactions remains to be a great challenge. We reported preliminary results on photooxidation of alcohols by a porphyrin/quinone/TEMPO system in AR2002. This year we report the mechanistic detail of this reaction system.

When a solution of porphyrin **1** (1 μmol), TEMPO (25 μmol), 2,5-di-*tert*-butyl-1,4-benzoquinone (100 μmol), benzyl alcohol (300 μmol) and *n*-dodecane (50 μmol; an internal standard for the gas chromatography) in 0.5 ml of dry pyridine was irradiated with visible light (λ > 500 nm), benzaldehyde was formed with concurrent formation of 2,5-di-*tert*-butyl-1,4-hydroquinone. The substrate dependence experiments revealed following order of reactivity: benzylic ≈ allylic > primary >> secondary (no reaction). This is in accordance with other reported TEMPO-mediated oxidation.

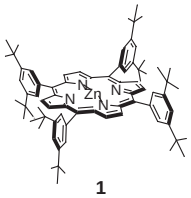

1

With benzyl alcohol as a substrate, the initial rates of product formation were examined under various conditions (Figure 1). As shown in parts (a) and (b), the rate increases with increasing concentrations of $PhCH_2OH$ and TEMPO. Particularly interesting is the dependence on the quinone concentration, shown in part (c). Here the initial rates decrease with increasing quinone concentration. The dependence on the porphyrin concentration (part (d)) also shows a similar trend.

The negative dependence on quinone concentration can be explained by considering the quantum yields of the triplet radical pairs. When the concentration of quinone becomes higher, the quantum yield of the triplet radical pair is lowered because the singlet state is more likely to be quenched prior to intersystem crossing. On the other hand, the negative dependence on porphyrin concentration is ascribed to the electron-transfer equilibrium between the porphyrin cation radical and TEMPO (Equation 1). As the concentration of porphyrin becomes higher, the equilibrium is pushed to the left and the steady-state concentration of the oxoammonium cation $TEMPO^+$ becomes lower. The proposed reaction mechanism is shown in Scheme 1.

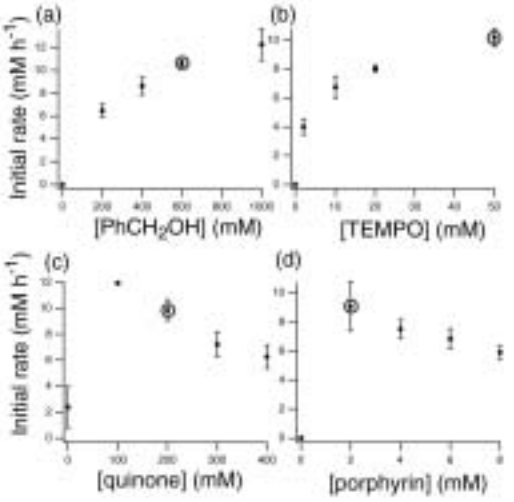

Figure 1. The initial rates of formation of PhCHO under various conditions.

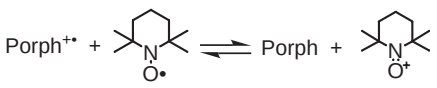

Equation 1.

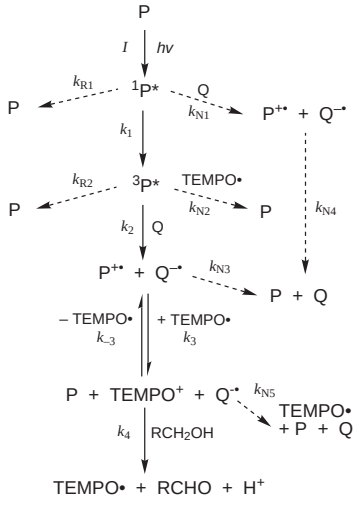

Scheme 1. Proposed reaction mechanism.

VIII-K Development of New Nanomaterials as Components in Advanced Molecular Systems

Nanometer-sized materials exhibit unique electronic behavior. In the quest of advanced redox catalysis, we are currently interested in combining nanometer-sized materials into molecular redox systems. Herein we report two attempts to develop new nanomaterials that potentially suit for combination with advanced molecular system.

VIII-K-1 Development of New Spatially-Relaxed Dendrimers and Their Application as Precursor to Redox Pool Molecules

KIKUZAWA, Yoshihiro; NAGATA, Toshi

We synthesized a series of new dendrimers with up to fourteen "internal" carboxyl groups. These dendrimers (**G$^{1–3}$**) are made from a branching unit and a spacer unit with a carboxyl group. Introduction of the spacer groups makes the internal carboxyl groups more spatially relaxed than previously reported dendrimers.

This type of dendrimer was used as a building framework of new redox pool molecules. The dendrimer **G^3** was connected to a porphyrin, the internal carboxyl groups were converted to alcohols, and ferrocene-carbonyl groups were introduced via ester linkages to give **P-G^3(Fc)$_{14}$**. This molecule will be useful for examination of photoinduced electron transfer between a porphyrin and multiple electron donor molecules.

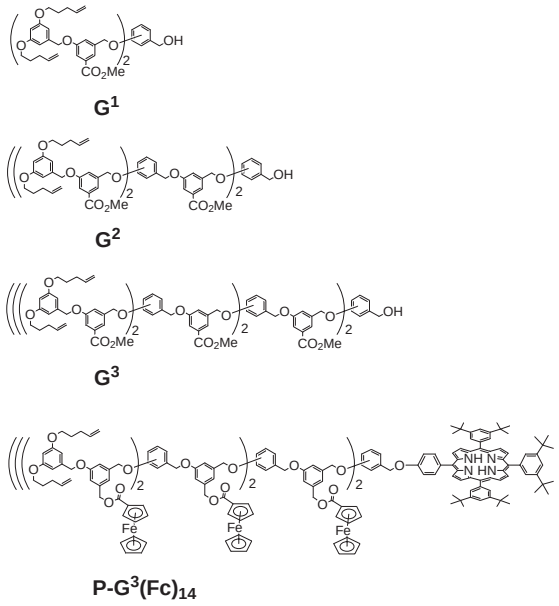

VIII-K-2 Synthesis and Size Control of Gold Sub-Nanoparticles Stabilized by Tripod Organic Molecules

HOSOKAWA, Youichi; NAGATA, Toshi

Recently, gold nanoparticles have received much attention as potentially useful materials showing novel electronic, optical, optoelectronic, and magnetic properties derived from the quantum size effect. One promising application of these materials is utilization as one of the functional "components" in molecular systems. To realize this idea we are developing techniques to treat metal nanoparticles as if they were "molecules."

We synthesized new tripod molecule **1**–**3** (Figure 1) and examined stabilization of of gold sub-nanoparticles stabilized by them. These molecules are designed so that a single molecule can enclose a single metal nanoparticle to give a "molecular" nanoparticle complex (Figure 2). The multi-point interaction by arylthioether units will produce the stabilization, and the different "leg" length will also result in size-selection of metal nanoparticles. Figure 3 shows the TEM pictures and the observed diameter distribution of gold nanoparticles derived from **1**–**3**. The most frequent values of the diameter distribution became larger with increasing numbers of the benzyl thioether units.

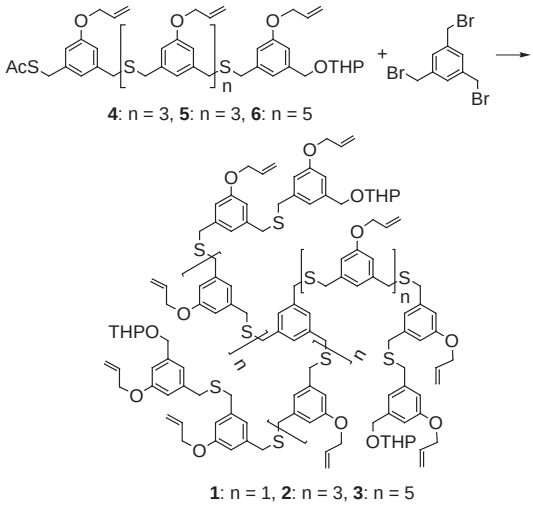

Figure 1. Preparation of the tripod molecules **1**–**3**.

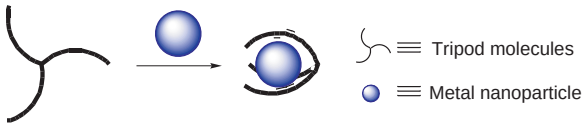

Figure 2. A schematic representation of the complex between the tripod molecule and the metal nanoparticle.

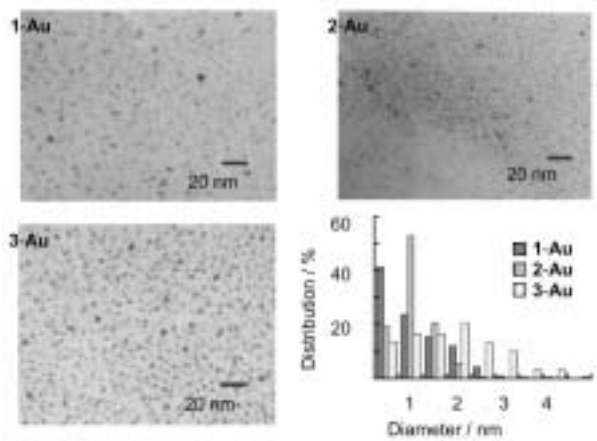

Figure 3. TEM images and the diameter distribution of **1-**, **2-**, and **3-Au**.

VIII-L Photochemistry on Well-Defined Surfaces

Upon the irradiation of light in the wavelength range from visible to ultraviolet, a number of adsorbed molecules on metal surfaces reveal variety of photochemical processes, including photo-stimulated desorption, rearrangement of adsorbed states, photodissociation, and photo-initiated reactions with coadsorbates. A central and fundamental question in the surface photochemistry is to clarify how adsorbate-substrate systems are excited by photon irradiation. In addition, since photo-initiated reactions can be induced without any thermal activation of reactants, they may provide good opportunities for studying a new class of surface reactions that may not be induced thermally. We have studied photochemistry of various adsorption systems on well-defined metal and semiconductor surfaces mainly by temperature-programmed desorption (TPD), x-ray photoelectron spectroscopy (XPS), work function measurements, near edge x-ray absorption fine structure (NEXAFS) and angular-resolved time-of-flight (TOF) mass spectrometry of photodesorbed species associated with pulsed laser irradiation.

VIII-L-1 Photo-Induced Oxygen Elimination on Silver Surfaces

NAKAGOE, Osamu[1]; OHTA, Michiharu[1]; WATANABE, Kazuya[1]; TAKAGI, Noriaki[1]; MATSUMOTO, Yoshiyasu
([1]GUAS)

[*Surf. Sci.* **528**, 144–150 (2003)]

We have investigated the structural changes in the added-rows of Ag–O chains at a Ag(110)(2×1)-O surface due to photo- and CO-induced elimination of O by using scanning tunneling microscopy. The photo-induced elimination occurs only on the surface containing carbidic carbon, resulting in the structural change of the added-rows from (2×1) to (4×1) according to the reduction of O coverage (θ_O). The structural change due to the CO-induced elimination depends on the carbon coverage: the (2×1) structure is retained in spite of the decrease of θ_O for the C-contained surface, while the structure changes sequentially from (2×1) to (4×1) and (6×1) for the carbon-free surface. Furthermore, the CO-induced elimination rate in the low θ_O on the carbon-free surface is much faster than that on the C-contained surface. These results indicate that the small amount of C atoms play an important role not only in the structural changes associated with the oxygen elimination reactions but also in the kinetics of the oxidation reaction of CO.

VIII-M Ultrafast Dynamics at Well-Defined Surfaces

To understand the mechanism of surface photochemistry, it is vital to know how photoinduced electronic excitation induces adsorbate nuclear motions that ultimately lead to chemical reactions. We demonstrate the real-time observations of substrate surface phonons and adsorbate-substrate vibrational modes by fs time-resolved second harmonics generation (TRSHG). If an excitation light pulse has a duration sufficiently shorter than a period of a vibrational mode or a phonon mode, it can excite the mode with a high degree of temporal and spatial coherence. This coherent nuclear motion modulates the second-order susceptibility $\chi^{(2)}$. Thus, by monitoring the intensity modulation of the second harmonics (SH) generation of a probe pulse, we can observe the evolution of the coherent nuclear motion subsequent to the electronic excitation at the surfaces.

VIII-M-1 Coherent Surface Phonon at a GaAs(100)-c(8x2) Surface

WATANABE, Kazuya[1]; DIMITROV, Dimitre T.[1]; TAKAGI, Noriaki[1]; MATSUMOTO, Yoshiyasu
([1]GUAS)

[*Phys. Rev. B* **65**, 235328 (7 pages) (2002)]

Coherent surface phonon at a GaAs(100)-c(8×2)-Ga reconstructed surface has been investigated by time resolved TRSHG. The phonon mode is impulsively excited by an ultrashort laser pulse and subsequent coherent nuclear motion is monitored through the intensity modulation of the second harmonics of a probe pulse. Oscillatory traces are clearly observed in TRSHG signals and their Fourier transformation show two peaks at 8.2–8.6 THz and 8.9 THz. Fitting these traces with two oscillatory components shows that the oscillatory signals are contributed by the bulk LO-phonon at 8.8 THz and the surface phonon at 6.0–8.6 THz. The relative amplitude of the surface phonon modes is sensitive to sputtering and annealing of the surface. Clear dips appear at 8.7 THz in the Fourier spectra, which is caused by the initial phase difference between the surface phonon and the bulk phonon modes. The frequency of the surface component shows red shifts as the pumping power increases. The shifts are indicative of a marked electron phonon interaction or anharmonicity of the surface phonon modes.

VIII-M-2 Impulsive Excitation of a Vibrational Mode of Cs on Pt(111)

WATANABE, Kazuya[1]; TAKAGI, Noriaki[1]; MATSUMOTO, Yoshiyasu
([1]GUAS)

[*Chem. Phys. Lett.* **366**, 606–610 (2002)]

We have performed TRSHG measurements regarding a Cs–Pt stretching mode on a Cs-covered Pt(111) surface under an ultrahigh vacuum condition. The TRSHG trace obtained from the clean surface shows an instantaneous sharp rise right after the excitation. This is followed by a fast decaying component (t < 1 ps) and a slowly decaying one persistent to the longest delay (t = 6 ps) of the measurements. When the surface is covered with Cs, SH signals are enhanced by about 70 times and strongly modulated waveforms are superimposed on the TRSHG traces. The power spectrum obtained from the Cs-covered Pt(111) surface shows a strong peak at 2.3 THz; this is assigned to the Cs–Pt stretching mode. The dephasing time of the coherent vibration was estimated to be 1.4 ps. The strong modulation is observed only the Cs-coverages larger than 0.24 ML. At these coverages alkali metal adsorbates are known to make metallic quantum wells. Thus, the resonant impulsive Raman process between quantum well states is responsible for the creation of the vibrating nuclear wavepacket motion in phase along the Cs–Pt stretching coordinate.

VIII-N Multiphoton Photoelectron Spectroscopy of Electronic States of Nano-Structured Materials on Surfaces

Electronic structure and excited state dynamics of nano-structured materials on surfaces are very important for exploring their properties, thermal reactivity and nonthermal processes including photochemistry and photo-induced charge transfer. For this purpose, we performed multiphoton photoelectron spectroscopy with fs lasers. This year we applied this method to a single-layered nano-graphite crystalline grown on a metal surface.

VIII-N-1 Anomalous Quenching of Electronic States of Nanographene on Pt(111) by Deuterium Edge Termination

KINOSHITA, Ikuo[1]; INO, Daisuke[2]; NAGATA, Kaoru[1]; WATANABE, Kazuya[2]; TAKAGI, Noriaki[2]; MATSUMOTO, Yoshiyasu
([1]Yokohama City Univ.; [2]GUAS)

[*Phys, Rev. B* **65**, 241402R (4 pages) (2002)]

The electronically excited state and its decay dynamics of graphite nano-crystals on metal surfaces have been investigated by fs time-resolved multi-photon photoelectron spectroscopy. Single-layer graphite nano-crystals are formed on a Pt(111) surface. The 3-photon photoelectron spectra taken from this surface reveal two peaks whose intensities are strongly correlated with the graphite coverage. By combining with the measurements of photoemission of adsorbed xenon used as another probe for local work functions, we can clearly identify for the first time that one of the peak is due to the electronically excited σ^* state of the graphite nano-crystal. Moreover, this state is extremely sensitive to hydrogen termination of the edge of the nano-crystal in contrast to the occupied π state. These findings clarify the properties of the electronic states of graphene and finally settle the controversy on the location of the interlayer band and its split-off state of bulk graphite.

VIII-O Chemistry of One-Dimensional Nano-Surface Compounds Studied by Scanning Tunneling Microscopy

The fluctuating configurations of low-dimensional structures can be thermodynamically favorable at finite temperatures, because the energy gain overcomes the energy cost that accompanies local structural fluctuation. In particular, one-dimensional (1D) systems have a propensity to be sensitive to these fluctuations as described by one of the maxims of condensed matter physics, *i.e.*, one chain does not make a crystal. Thus, the dynamical formation of active species and sites by these fluctuations is a key factor in establishing a microscopic model for chemical reactions at surfaces and nano-structured compounds.

VIII-O-1 Role of Structural Fluctuation in a Surface Reaction Studied by Scanning Tunneling Microscopy: The CO + O → CO_2 Clean-Off Reaction on Ag(110)(2x1)-O

NAKAGOE, Osamu[1]; WATANABE, Kazuya[1]; TAKAGI, Noriaki[1]; MATSUMOTO, Yoshiyasu
([1]GUAS)

[*Phys. Rev. Lett.* **90**, 226105 (4 pages) (2003)]

It is well known that the adsorption of O on Ag(110) results in the formation of quasi-1D structures, AgO chains, accompanied by the mass transfer of substrate atoms.

AgO chains arrange periodically to form (n×1) (n = 2 ~ 7) depending on the fractional O coverage due to repulsive inter-chain interactions. While the chains appear as rigid straight lines in the (2×1) structure at room temperature, the structures fluctuate to appear as segmented and sometimes "frizzy" chains in the (n×1) ($n \geq 4$) structures. Energetically-equivalent structures of different configurations of segments exist, reflecting the 1D nature of the chains. Thus, chains fluctuate between configurations rather than freezing into a single configuration, and consequently segmented or frizzy chains are observed. Therefore, AgO chains on Ag(110) is a good system for investigating the effects of structural fluctuation on reactivity.

The kinetics of the clean-off reaction of O adatoms by CO on Ag(110)(2×1)-O is investigated by scanning tunneling microscopy. The reaction is accelerated in the lower O coverage range where AgO chains with (n×1) ($n \geq 4$) configurations show significant structural fluctuation. Simulations based on the Ising model are used to provide a quantitative understanding of the acceleration, which originates from the dynamical formation of active O adatoms by fluctuation of AgO chains.

VIII-P Adsorbate Structure and Surface Chemistry on Well-Defined Surfaces

Surface reactions have been playing an important role in production of many useful compounds and also fabrication of electronic devices. In particular, investigations on the structures of adsorbates and their reactivity are the first step for understanding more complicated catalytic reactions. We investigate surface reactions and kinetics by means of various techniques including temperature-programmed desorption (TPD), x-ray photoelectron spectroscopy (XPS), ultraviolet photoelectron spectroscopy (UPS), work function measurements, Auger electron spectroscopy (AES), infrared reflection absorption spectroscopy (IRAS) and scanning tunneling microscopy (STM).

VIII-P-1 Thermal Decomposition of Acetylene on Pt(111) Studied by Scanning Tunneling Microscopy

NAKAGOE, Osamu[1]; TAKAGI, Noriaki[1]; MATSUMOTO, Yoshiyasu
([1]GUAS)

[*Surf. Sci.* **514**, 414–419 (2002)]

The adsorption and the thermal decomposition processes of C_2H_2 on Pt(111) have been investigated by the use of STM. For a high C_2H_2 coverage, a (2×2) structure is observed locally after the C_2H_2-covered Pt(111) surface is heated to 120 K. By heating to 220 K, the sample surface is covered with the (2×2) structure separated with brighter lines. After heating up to 370 K, (2×2) domains related to ethylidyne species appear with larger and brighter protrusions. For a low C_2H_2 coverage, adsorbates are located randomly and no ordered islands are observed after heating to 120 K. In contrast, heating to 220 K leads to the formation of (2×2) islands. This indicates that the adsorbate-adsorbate interaction in the (2×2) structure observed by 120 K heating is different from that in the (2×2) structure observed by 220 K heating; the former is repulsive, but the latter attractive. Therefore, it is suggested that different surface species are formed by the decomposition of C_2H_2 at 220 K. The detail of the decomposition processes of C_2H_2 and the relation between the adsorbate-adsorbate interaction and the surface species are discussed. The results are also reported measured by heating up to higher temperatures above 400 K.

VIII-P-2 Reaction Intermediates in the Oxidation of Methanol on a Pt(111)-(2x2)O Surface

LIU, Zhengxin[1]; SAWADA, Takeshi[1]; TAKAGI, Noriaki[1]; WATANABE, Kazuya[1]; MATSUMOTO, Yoshiyasu
([1]GUAS)

[*J. Chem. Phys.* **119**, 4879–4886 (2003)]

The oxidation of methanol on a Pt(111)-(2×2)O surface has been investigated by infrared reflection absorption spectroscopy and temperature-programmed desorption. Methanol is dehydrogenated to produce methoxy species in the annealing temperature range from 130 to 170 K. At above 170 K, the reaction proceeds differently, depending on methanol coverage. At the saturation coverage, methanol adsorbates partly desorb molecularly and partly react with precovered

oxygen atoms to produce CO, H_2 and H_2O. No detectable formaldehyde or formate is formed. In contrast, at submonolayer coverages, methoxy species is dehydrogenated to yield formaldehyde at ~ 180 K and further oxidized to formate at ~ 200 K. Formate is decomposed by 300 K. Defect sites such as steps are not relevant to the formation of the intermediates. When CO is coadsorbed on the surface, it destabilizes the reaction intermediates. The destabilization by coadsorbed CO makes the reaction intermediates short lived as not to be detectable at high initial coverages of methanol.

VIII-Q Structures and Photophysical Properties of Monolayer–Protected Metal Clusters

For the last decade, the monolayer-protected metal clusters (MPCs) have gained much attention both as prototype systems to study the size dependent evolution of the electronic properties of the metal clusters and as promising candidates for elementary units of nano-scale devices. The emergence of novel optical and electronic properties is expected for small-sized MPCs because their electronic energy levels become quantized due to the electron confinement into the small dimensions. For example, it is anticipated that the small MPCs exhibit photoluminescence since the radiative process of the photoexcited state can compete with the phonon-mediated nonradiative relaxation processes. Our interests are focused on the following issues on the MPCs: (1) preparation and characterization of the small MPCs with core diameters of ~ 1 nm range (~ 40 atoms/cluster) which may exhibit molecular–like electronic and charging properties, (2) determination of structural dimensions (core diameters and monolayer thickness), (3) development of size–selection method, and (4) clarification of the effects of the core size, core shape, and thiolate ligation on the optical and electronic properties.

VIII-Q-1 One-Pot Preparation of Subnanomerter-Sized Gold Clusters *via* Reduction and Stabilization by *meso*-2,3-Dimercaptosuccinic Acid

NEGISHI, Yuichi; TSUKUDA, Tatsuya

[*J. Am. Chem. Soc.* **125**, 4046–4067 (2003)]

We report herein a simple method to prepare subnanometer-sized gold clusters by the reactions between hydrogen tetrachloroaurate ($HAuCl_4$) and *meso*-2,3-dimercaptosuccinic acid (DMSA; $HO_2CCH(SH)CH(SH)CO_2H$) in water. It is demonstrated that DMSA molecules efficiently reduce the Au(III) species and stabilize the resultant gold clusters. The Au:DMSA clusters, which tend to aggregate into assemblages in water, can be well-isolated each other by ion-pair formation between the carboxyl groups of DMSA and tetraoctylammonium (TOA) cations. This surface modification enables us to examine the core size distributions of the individual clusters by mass spectrometry and TEM. It is revealed that the gold clusters comprised of 10–13 atoms (*ca.* 0.8 nm) are the main products of the reactions.

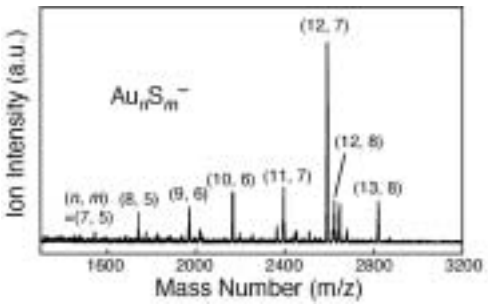

Figure 1. Laser desorption ionization mass spectrum of Au:DMSA-TOA clusters.

VIII-Q-2 Photoluminescence from Nearly Monodispersed Au_{12} Clusters Protected by *meso*-2,3-Dimercaptosuccinic Acid

NEGISHI, Yuichi; TSUKUDA, Tatsuya

[*Chem. Phys. Lett.* **383**, 161–165 (2004)]

Nearly monodispersed gold clusters ($Au_{\sim 12}$) protected by *meso*-2,3-dimercaptosuccinic acid (DMSA) exhibit luminescence at 630 nm with a quantum yield of 1×10^{-6} upon the photoexcitation at 390 nm into the lowest electronic excited state. The large Stokes shift (1.2 eV) suggests that the visible PL is assigned to phosphorescence originating from a triplet-like excited state. The PL quantum yield was enhanced up to 0.9%, greater by 8 orders of magnitude than that of bulk gold, by thickening the protecting layer and freezing of the solvent at 77 K. The emission peak energy is discussed within the context of core-size dependent electronic structures by comparing with those of other gold MPCs reported in literatures.

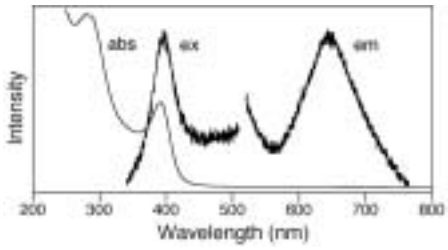

Figure 1. Optical absorption, emission and excitation spectra of Au:DMSA clusters at 298 K; λ_{ex} = 400 nm, λ_{em} = 630 nm.

VIII-Q-3 Isolation and Characterization of Subnanometer-Sized Gold Clusters

NEGISHI, Yuichi; SATO, Seiichi[1]; TAKASUGI, Yoshimitsu[1]; YAO, Hiroshi[1]; KIMURA, Keisaku[1]; SCHAAFF, T. Gregory[2]; WHETTEN, Robert L.[3]; TSUKUDA, Tatsuya

([1]Himeji Inst. Tech.; [2]Oak Ridge Natl. Lab.; [3]Georgia Inst. Tech.)

The Au:SG clusters with the core diameters of 0.8–1.0 nm were synthesized in Kimura group by reducing $AuCl_4^-$ with $NaBH_4$ in the presence of glutathione GSH molecules ($AuCl_4^-$:GSH = 1:2).[1)] The Au:SG clusters thus prepared were further fractionated into five distinct components by using polyacrylamide gel electrophoresis (PAGE).[2),3)] In order to characterize the chemi-

cal composition of these components, the electrospray ionization (ESI) mass spectra were recorded by using an apparatus constructed at IMS. The negative-ion mode ESI mass spectra of these fractions are comprised of series of multiply charged ions of $Au_{21}(SG)_{12}$, $Au_{25}(SG)_{14}$, $Au_{28}(SG)_{16}$, $Au_{32}(SG)_{20}$, $Au_{38}(SG)_{23}$, respectively, demonstrating the isolation of nearly singly-sized clusters. It is found that these isolated clusters exhibit visible photoluminescence with quantum yields in the order of 10^{-3}.

References

1) S. H. Chen and K. Kimura, *Langmuir* **15**, 1075–1082 (1999).
2) T. G. Schaaff, G. Knight, M. N. Shafigullin, R. F. Borkman and R. L. Whetten, *J. Phys. Chem. B* **102**, 10643–10646 (1998).
3) T. G. Schaaff and R. L. Whetten, *J. Phys. Chem. B* **104**, 2630–2641 (2000).

VIII-Q-4 Construction of Apparatus for Photoelectron and Photodissociation Studies of Mass-selected Organometallic Clusters

NEGISHI, Yuichi; NARUSHIMA, Takashi[1]; TSUKUDA, Tatsuya
([1]GUAS)

The electronic structures of the MPCs, especially in the subnanometer-sized regime, are significantly influenced by the thiolate (RS) coordination against the metallic cores as well as their core sizes. In order to study such effects, it is necessary to prepare and isolate the mass selected $M_n(SR)_m$ clusters ($m \geq 0$) in the gas phase, since the clusters with small m are unstable against the aggregation in liquid dispersion. To this end, we have developed a new apparatus, which consists of a cluster ion source, a tandem time-of-flight mass spectrometer, and a photoelectron spectrometer. In the cluster source, the bare metal clusters produced by laser vaporization of the metal target are allowed to react with the thiol molecules, RSH, to form organometallic clusters. The anionic clusters, $M_n(SR)_m^-$, are mass-selected by the first TOF mass spectrometer and then irradiated by pulsed laser light. The photoelectrons and photofragments are detected by the magnetic-bottle type photoelectron spectrometer and the secondary TOF mass spectrometer, respectively.

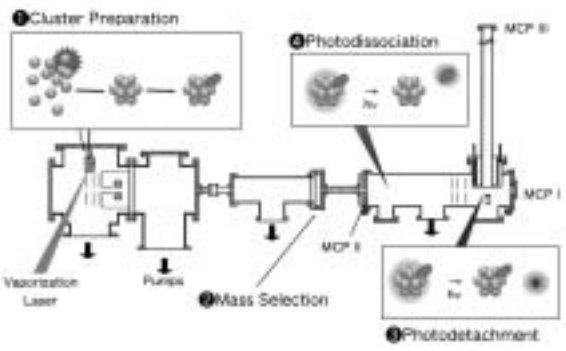

Figure 1. Schematic diagram of the experimental setup.

VIII-Q-5 EXAFS Study on Interfacial Structure between Pd Cluster and *n*-Octadecanethiolate Monolayer: Formation of Mixed Pd–S Interlayer

MURAYAMA, Haruno; ICHIKUNI, Nobuyuki[1]; NEGISHI, Yuichi; NAGATA, Takashi[2]; TSUKUDA, Tatsuya
([1]Chiba Univ.; [2]Univ. Tokyo)

[*Chem. Phys. Lett.* **376**, 26–32 (2003)]

The geometrical structure of a Pd cluster (diameter of ≈ 3.1 nm) protected by *n*-octadecanethiolate monolayer has been investigated by high-resolution TEM (HRTEM), XRD, and EXAFS spectroscopy. The HRTEM and XRD measurements have revealed that the cluster core is comprised of an *fcc* single crystal of Pd. The mean coordination numbers of the Pd–Pd and Pd–S shells determined by the Pd *K*-edge EXAFS analysis suggest that the surface of the Pd core is sulfurized to form a mixed Pd–S layer underneath the thiolate monolayer.

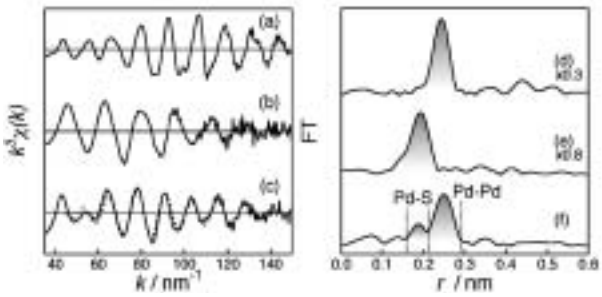

Figure 1. k^3-weighted Pd *K*-edge EXAFS spectra after background subtraction; (a) Pd foil, (b) PdS pellet, (c) Pd:SC_{18} clusters. The broken line in panel (c) represents the best-fit result. Fourier-transforms of the EXAFS spectra; (d) Pd foil, (e) PdS pellet, (f) Pd:SC_{18} clusters.

VIII-Q-6 Structures and Stabilities of Alkanethiolate Monolayers on Palladium Clusters as Studied by Gel Permeation Chromatography

MURAYAMA, Haruno; NARUSHIMA, Takashi[1]; NEGISHI, Yuichi; TSUKUDA, Tatsuya
([1]GUAS)

[*J. Phys. Chem. B* submitted]

Palladium clusters protected by a series of *n*-alkanethiolates, Pd:SC_n (SC_n = *n*-$C_nH_{2n+1}S$, n = 10, 12, 14, 16, and 18), were prepared by a ligand exchange approach: Pd clusters protected by poly (*N*-vinyl-2-pyrrolidone) (PVP) were transferred from aqueous phase to the toluene phase containing the thiols. The structures and stabilities of the thiolate monolayers of the Pd:SC_n clusters were investigated by gel permeation chromatography (GPC) together with TEM, XPS, and FT-IR. The thicknesses of the thiolate layers formed on the Pd clusters were evaluated from the differences between the hydrodynamic diameters and core diameters of the Pd:SC_n clusters, determined by GPC and TEM, respec-

tively. The thicknesses thus obtained are in good agreement with the lengths of the corresponding thiolates in the all-*trans* conformations, illustrating that the alkanethiolates in nearly straight configurations are aligned almost perpendicularly to the core surfaces. Fractionation of the Pd:SC_{18} clusters by GPC yielded a series of the purified samples: the clusters in each fraction are different in their core sizes. The GPC measurements on the Pd:SC_n clusters with small n revealed the decomposition of the monolayers through spontaneous etching and their reconstruction by heat treatment in the presence of the free thiols. The mechanism of these processes is discussed. The present study demonstrates that the GPC provides an elemental and versatile means to characterize and purify the monolayer-protected clusters.

VIII-R Mass Spectroscopic Studies on Nanoscale Materials

Information on the size, shape, and dispersity is of fundamental importance in understanding natures and functions of nanoscale materials. Traditionally, transmission electron microscope (TEM) and powder X-ray diffraction have been employed to measure size, shape and size distributions of the nanoscale materials. We have applied an alternative technique, mass spectrometry, to provide more detailed insight into the structures of these fascinating materials.

VIII-R-1 Self-Assembly of Si Clusters into Single Crystal Arrangements: Formation of Si_{10} Cluster Crystals

SATO, Seiichi[1]; YAMAMOTO, Naoaki[1]; NAKANISHI, Kentaro[1]; YAO, Hiroshi[1]; KIMURA, Keisaku[1]; NARUSHIMA, Takashi[2]; NEGISHI, Yuichi; TSUKUDA, Tatsuya
([1]Himeji Inst. Tech.; [2]GUAS)

[*Jpn. J. Appl. Phys.* **42**, L616–L618 (2003)]

Single crystals at an air/solution interface or a solution/hydrogen-terminated Si substrate interface were created using a self-assembly process, which originated from the hydrophobic nature of Si clusters. Mass analysis indicated that the components of the cluster crystals were partially oxidized hydrogenated Si_{10} clusters. At either interface the nearest-neighbor distances between lattice points in the Si cluster crystals were 0.53 nm or 0.60 nm, which is consistent with the diameters of the Si_{10} clusters. The slight difference in these values seems to be due to variations in the surface passivation of the component Si_{10} clusters.

VIII-R-2 Highly Oxygenated Fullerene $C_{60}O_n$ formed by Corona Discharge Ionization in the Gas Phase

TANAKA, Hideki[1]; TAKEUCHI, Kazuo[1]; NEGISHI, Yuichi; TSUKUDA, Tatsuya
([1]RIKEN)

[*Chem. Phys. Lett.* in press]

Oxygenated fullerenes were produced by a vaporization source equipped with a corona discharge ionizer in the presence of a trace amount of oxygen. *In situ* mass analysis revealed that the species formulated as $C_{60}O_n$ ($n \leq 30$) are formed in the source and that the degree of oxygenation can be altered through the discharge current. Formation of the epoxidized structure in the $C_{60}O_n$ was confirmed by XPS measurements of the thin films of $C_{60}O_n$ and semi-empirical PM3 calculations for $C_{60}O_{30}$. The structures and formation processes for higher analogues $(C_{60})_mO_n$ (m = 2, 3) are briefly discussed.

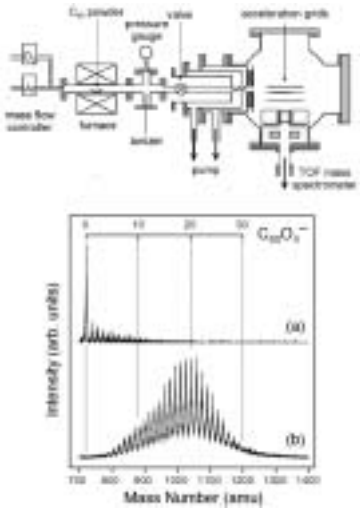

Figure 1. Schematic diagram of experimental setup (top) and typical mass spectra of the negative ions produced by the corona discharge ionizer (bottom) operated at 100 mA under Ar gas flow (a) without oxygen and (b) with 1% oxygen.

VIII-S Structures and Reactions of Molecular Cluster Ions

Molecular clusters, intermediate states of matter between the bulk and the molecule, provide us unique opportunities to study how the chemical and physical properties evolve with a degree of aggregation. We have studied reactions of hydrated anions with a simple molecule by using mass spectrometry, photoelectron and photodissociation spectroscopies and *ab initio* calculations.

VIII-S-1 Gas-Phase Reaction of Hydrated $CO_2^{\cdot-}$ Anion Radicals with CH_3I

TSUKUDA, Tatsuya; NAGATA, Takashi[1]
([1]Univ. Tokyo)

[*J. Phys. Chem. A* **107**, 8476–8483 (2003)]

Hydrated $CO_2^{\cdot-}$ anion radicals, $CO_2^{\cdot-}(H_2O)_n$, are selectively prepared in an electron-impact free jet of $CO_2^{\cdot-}$ containing H_2O. Mass spectrometric measurement reveals that $CO_2^{\cdot-}(H_2O)_n$ reacts with CH_3I to form an anion with $[(CO_2)(H_2O)]^-$ stoichiometry. The product $[(CO_2)(H_2O)]^-$ is further identified as the anion of acetyloxy iodide, $CH_3CO_2I^-$, based on the observation that $[(CO_2)(H_2O)]^-$ photodissociates at 532 nm into $CH_3CO_2^-$ + I or CH_3CO_2 + I^- channels. The $CO_2^{\cdot-}(H_2O)_n$ + CH_3I reaction thus presents a sharp contrast to the corresponding reaction in solution: the gas-phase $CO_2^{\cdot-}(H_2O)_n$ behaves as a carboxylation reagent for alkyl halide (RX), whereas in aqueous solutions the reaction proceeds as $CO_2^{\cdot-}$ + RX → CO_2 + R + X^-. *Ab initio* calculations suggest that $CO_2^{\cdot-}(H_2O)_n$ can take on structures preferable for radical reactions: the hydraion occurs on the O atoms of $CO_2^{\cdot-}$ and the unpaired electron on the C atom remains uncovered with H_2O solvents. The reaction mechanism of the $CO_2^{\cdot-}(H_2O)_n$ + CH_3I process is discussed in conjunction with previous results of $(CO_2)_n^{\cdot-}$ + CH_3I.[1)]

Reference

1) T. Tsukuda, M. Saeki, S. Iwata and T. Nagata, *J. Phys. Chem. A* **101**, 5103–5110 (1997).

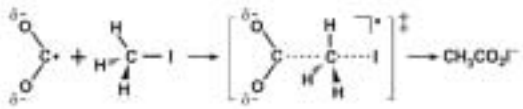

Scheme 1.

VIII-T Nanoscale Characterization of Heterogeneous Catalyst Surfaces

Heterogeneous catalysis occurs on a surface of a solid catalyst. Active centers for heterogeneous catalysis commonly consist of clusters of several surface atoms, and thus a long-range order of surface atoms is not normally required. Therefore, when using precious metals as catalysts, nanometer-scale superfine particles are commonly employed in order to increase its surface area and to decrease the amount of catalysts. This introduces difficulties in characterizing the catalyst surfaces and their active centers, because characterization techniques of solid surfaces at nanometer-scale are not well established. Here we mainly used scanning probe microscopes, in conjunction with other surface characterization techniques, to characterize catalytically active centers as well as the nature of catalyst-support interactions.

VIII-T-1 Monte Carlo Simulation of Pyridine Base Adsorption on Heulandite (010)

YOKOI, Yasuto[1]; YELKEN, Gulnihal[2]; OUMI, Yasunori[3]; KOBAYASHI, Yasunori[1]; KUBO, Momoji[1]; MIYAMOTO, Akira[1]; KOMIYAMA, Masaharu[4]
([1]Tohoku Univ.; [2]Izmir Inst. Tech.; [3]Japan Inst. Sci. Tech.; [4]IMS and Yamanashi Univ.)

[*Appl. Surf. Sci.* **188**, 377–380 (2002)]

Adsorption of pyridine base molecules (pyridine and α-, β- and γ-picolines) on a surface of a natural zeolite, heulandite (010), was examined by Monte Carlo simulations. Two types of adsorption areas were identified on heulandite (010) bound by surface OH arrays, and each area showed different influence on the adsorption and orientation for pyridine base molecules. The presence of methyl group and its position within the adsorbed molecule also influenced its adsorption characteristics. For pyridine adsorption, molecular dynamics simulation was also performed. The results were compared with existing experimental data obtained through atomic force microscopy.

VIII-T-2 Apparent Local Structural Change Caused by Ultraviolet Light on a TiO_2 Surface Observed by Scanning Tunneling Microscopy

KOMIYAMA, Masaharu[1]; LI, Yanjun; YIN, Donghong[2]
([1]IMS and Yamanashi Univ.; [2]Funan Normal Univ.)

[*Jpn. J. Appl. Phys.* **41**, 4936–4938 (2002)]

An apparent local surface structural change at nano-scale was observed by scanning tunneling microscopy on a TiO_2 surface upon irradiation with ultraviolet (UV) light. This phenomenon was reversible with UV light irradiation, and was interpreted to be due to the local accumulation of photoexcited states. This is the first real-space observation of inhomogeneous local charge distribution under UV light irradiation at nanoscale on a semiconductive photocatalyst surface, which may help identify the photocatalytic active sites and elucidate their reaction mechanisms.

VIII-T-3 Electronic Structure Change on TiO_2 Surface due to UV Light Irradiation

KOMIYAMA, Masaharu[1]; YIN, Donghong[2]; LI, Yanjun
([1]IMS and Yamanashi Univ.; [2]Funan Normal Univ.)

[*Stud. Surf. Sci. Catal.* **145**, 153–156 (2003)]

Photocatalysts have been paid extensive attentions for their environmental as well as energy applications. Although each photocatalytic processes may be different in terms of their kinetics and surface reactions involved, they are all initiated with the photoexcitation of TiO_2 electrons, the process commonly understood and explained by the so-called band model which assumes an infinite array of crystallographic lattice points. In contrast, catalytic reactions involved in photocatalysis are highly local in nature: some reactant may need particular local arrangements of atoms that are present on the catalyst surface, and others may need particular local electronic states of the surface atoms to provide unique adsorption or reaction sites. Despite this gap that exist in between the two descriptions involved in heterogeneous photocatalysis (band model and local catalysis), no efforts to address and bridge this gap are known to the authors. The present report is the first of such attempts, and examines the local electronic characters of TiO_2 surface upon UV-light illumination by means of scanning tunneling microscopy (STM).

VIII-T-4 In Situ Observations of Tetraamineplatinum (II) Hydroxide Adsorption from Its Aqueous Solution on Heulandite (010) Surface by Atomic Force Microscopy

KOMIYAMA, Masaharu[1]; LI, Yanjun; GU, Ning[2]
([1]IMS and Yamanashi Univ.; [2]Southeast Univ.)

Adsorption of tetraamineplatinum (II) hydroxide, a Pt catalyst precursor, from its aqueous solution on a (010) surface of a natural zeolite heulandite was observed, in situ, by atomic force microscopy (AFM). The Pt complex exhibited certain adsorption habits on the surface, frequently forming a short chain along the zeolite *a* axis, separated by three times the *c* unit cell length in the *c* direction. Possible adsorption sites on the surface were identified and discussed. The present work constitutes the first in situ atomic-level observation of a

liquid-phase preparation process of supported metal catalysts.

VIII-T-5 Defect Creation on Rutile TiO_2 (110)-(1x1) Surface due to Light Irradiation Observed by Scanning Tunneling Microscopy

LI, Yanjun; MATSUMOTO, Taki; GU, Ning[1]; KOMIYAMA, Masaharu[2]
([1]Southeast Univ.; [2]IMS and Yamanashi Univ.)

Laser light irradiation created atomic-scale structures on rutile TiO_2 (110)-(1×1) surface, the number of which increased with irradiation time. The created bright structures appear to be cross-shaped, each bridging two titanium [001] rows, and having dark areas in the front and in the back. The structure is interpreted as an oxygen deficiency on the (1×1) surface, and the one of the dark spots around the structure as the oxygen atom displaced from its original position. The structure often appears as a pair aligned along [1-10] direction, which could be viewed as a local (2×3) structure.

VIII-T-6 Crater Structures on a Molybdenite Basal Plane Observed by Ultra-High Vacuum Scanning Tunneling Microscopy

KOMIYAMA, Masaharu[1]; KIYOHARA, Kohei[2]; LI, Yanjun; KUBOTA, Takeshi[2]; OKAMOTO, Yasuaki[2]
([1]IMS and Yamanashi Univ.; [2]Shimane Univ.)

Atomic structure of a natural molybdenite (MoS_2) single crystal basal plane was examined by ultra-high vacuum scanning tunneling microscopy (UHV-STM). After high-temperature (473 K) resulfidation, numbers of crater structures with diameters ranging from 6 to 8 nm were observed. Atomic structures within these craters were continuous from the surrounding terrace, with no step structures at the rims of the craters. Atoms in the bottom of the craters showed higher corrugations compared to the terrace atoms, indicating perturbed electronic states in the craters. Its implication in hydrodesulfurization activity over MoS_2 basal plane is discussed.

VIII-U Fundamental Study on Electrostatic Manipulation of Biomolecules and its Application to Gene Analysis

Since conventional DNA sequencing method can determine up to 1000 base pairs at one time, longer DNA must be cut into small fragments. However, order information among these fragments is inevitably lost resulting in tremendous post sequencing process to do a puzzle. To cope with the problem, we have studied DNA sequencing method based on one-by-one DNA handling. The method includes (1) electrostatic manipulation of genomic DNA, (2) fixation in a stretched from, (3) cut from the terminus, (4) recovery and amplification of the fragments.

VIII-U-1 Manipulation of Single Coiled DNA Molecules by Laser Clustering of Microparticles

HIRANO, Ken[1]; BABA, Yoshinobu[1]; MATSUZAWA, Yukiko[2]; KATSURA, Shinji[2]; MIZUNO, Akira
([1]Tokushima Univ.; [2]Toyohashi Univ. Tech.)

A method of manipulating single DNA molecules for application in single-molecule analysis was developed. Manipulation of laser clustered beads allowed manipulation of a single DNA molecule without modification. Figure 1 shows sequential photographs of a DNA molecule anchored at both end to a glass surface. The DNA molecule was tweezed at one point and successfully stretched (figure1(b)–(d)). The stretched DNA molecule returned to its original form after releasing by turning off the laser beam (figure1(e)).

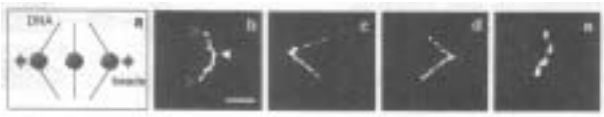

Figure 1. Sequential images of the manipulation of a single DNA molecule using laser clustering of 0.2 μm latex beads.

VIII-U-2 One-End Immobilization of Individual DNA Molecules on a Functional Hydrophobic Glass Surface

MATSUURA, Shun-ichi[1]; KURITA, Hirofumi[1]; NAKANO, Michihiko[1]; KOMATSU, Jun[1]; TAKASHIMA, Kazunori[1]; KATSURA, Shinji[1]; MIZUNO, Akira
([1]Toyohashi Univ. Tech.)

An extremely simple technique of DNA immobilization on a hydrophobic glass surface was developed. The technique includes hydrophobic processing of a cover slip with dichlorodimethylsilane and modification of the terminus of DNA with sulfhydryl group. Dichlorodimethylsilane reacts with silanol groups on a cover slip surface (figure1(a)) and forms hydrophobic monolayer of dichlorodimethylsilane (figure1(b)). Sulfhydryl group of DNA molecule modified at one terminus reacts on the dichlorodimethylsilane layer resulting in anchoring of a single DNA molecule to the cover slip (figure1(c))

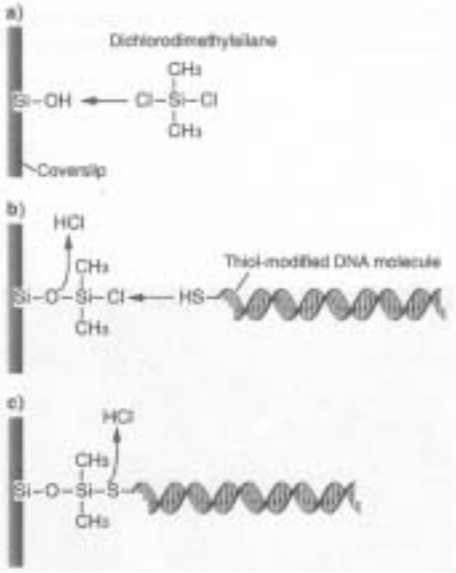

Figure 1. Schematic diagram of reaction mechanism of DNA immobilization on a dichlorodimethylsilane-coated surface.

VIII-U-3 Single-Molecule PCR using Water-in-Oil Emulsion

NAKANO, Michihiko[1]; KOMATSU, Jun[1]; MATSUURA, Shun-ichi[1]; TAKASHIMA, Kazunori[1]; KATSURA, Shinji[1]; MIZUNO, Akira
([1]Toyohashi Univ. Tech.)

[*J. Biotechnology* **102**, 117–124 (2003)]

A simple PCR method utilizing a water-in-oil (W/O) emulsion was developed. Numerous numbers of droplets serving as reaction mixture are included in bulk oil phase in this system. The method allows amplification of very low concentration DNA samples because such droplets increase effective concentration of template DNA. In this method, PCR was started with emulsified samples, in which template DNA was amplified to sufficient amount applicable to conventional PCR next step. After the first PCR in emulsified state was completed, W/O emulsion was broken by centrifuging to start the conventional PCR. By using this method consisting of 13 and 25 cycles in the first and the second step, target DNA of which concentration is 1molecule/tube was successfully amplified.

VIII-U-4 FIM Observation of DNA Molecules

FURUMAKI, Takuya[1]; TSUJI, Yuuta[1]; NAKANO,

Michihiko[1]; TAKASHIMA, Kazunori[1]; UCHIDA, Hironaga[1]; KATSURA, Shinji[1]; MIZUNO, Akira
([1]Toyohashi Univ. Tech.)

An application of field ion microscope (FIM) to DNA sequencing has been experimentally studied. By applying a DC voltage to a FIM tip on which a DNA molecule is attached, the bases may be released and carried along the electric field. Ultra high-speed genome analysis will be feasible by detecting the digested bases. We constructed a DNA sequencing system based on a field ion microscope. An electro-polished gold was used as a substrate. DNA molecules modified with sulfhydryl (-SH) group prepared by PCR (polymerase chain reaction) were attached on the needle tip. High voltage up to 7 kV was applied to DNA-bound tip to observe the FIM images. It was found that binding of DNA on samples decreased on-set voltage of FIM images suggesting the existence of an atomically rough surface.

VIII-U-5 Micro Reactor System Based on Water-in-Oil Emulsion

NAKANO, Michihiko[1]; NAKAI, Naohito[1]; TAKASHIMA, Kazunori[1]; KATSURA, Shinji[1]; MIZUNO, Akira
([1]Toyohashi Univ. Tech.)

A method called as “combinatory chemistry” has been proposed to create useful enzymes higher active and stable. Since the combinatory chemistry is based on multiple mutations of enzymes and evaluation of those mutants, high through-put production and analysis of enzymes is required to promote this method. For this purpose, miniaturization of reactors has been developed by using micro fabrication techniques. However, the miniaturization accompanies with difficulty of liquid handling, therefore size of reactors was limited by liquid handling technique.

To overcome this problem, we have been engaged in development of reaction system based on water-in-oil emulsion. W/O emulsion contains large amount of water droplets in continuous oil phase. Because many biological molecules are hydrophilic, those can be enclosed in the droplets. This indicates that the droplets play a role of small reactors, however reaction control of the droplets has not been established. We are developing unit operations such as transport, fusion to achieve reaction control of the droplets. In this term, we have developed transport methods based on electro-osmosis and charge injection. We have succeeded to drive the droplets by both methods. Now, we are engaged in improving controllability of droplet transport.

VIII-V Studies of Electronic Structure of Organic Thin Films

Electronic structures of organic film surface and organic/inorganic interface are expected to play an important role in organic-device properties. It is important to clarify the characteristics of not only occupied states but also unoccupied states for organic thin films, since the device properties such as the efficiency of the electron and/or the hole injection depend on the position and/or the distribution of these electronic states. We have investigated the electronic structure of organic film surface and organic/inorganic interface using surface sensitive spectroscopies such as photoelectron spectroscopy and near-edge x-ray absorption fine structure (NEXAFS). To help the assignment of NEXAFS spectra, we use the photon energy dependence of photon-stimulated ion desorption, since the chemical bond scission by inner-shell excitation depends on the electronic configuration of the excited state.

VIII-V-1 Photodegradation of Poly(Tetrafluoroethylene) and Poly(Vinylidene Fluoride) Thin Films by Inner Shell Excitation

OKUDAIRA, K. Koji; YAMANE, Hiroyuki[1]; ITO, Kazuyuki[1]; IMAMURA, Motoyasu[2]; HASEGAWA, Shinji; UENO, Nobuo[1]
([1]Chiba Univ.; [2]AIST)

[*Surf. Rev. Lett.* **9**, 335–340 (2002)]

Ion time-of-flight (TOF) mass spectra of poly(tetrafluoroethylene) (PTFE) and poly(vinylidene fluoride) (PVDF) thin films near fluorine and carbon *K*-edges were observed. For PTFE thin films peaks corresponding to F^+, CF^+, and CF_3^+ appeared, while for PVDF F^+ and H^+ were mainly observed. They indicate that for PTFE the polymer chain (C–C bonds) as well as C–F bonds are broken by irradiation of photons near fluorine and carbon *K*-edges, while for PVDF the bond scission occurs mainly at the C–F and C–H bond. In Figures 1 (a), (b), and (c) partial ion yield (PIY) spectra of F^+, CF^+ and CF_3^+ for PTFE thin films are compared with total electron yield (TEY) near the fluorine *K* absorption edge. PIY spectra of F^+, CF^+ and CF_3^+ are different from the TEY spectrum. The intense PIY feature of F^+ appears at $h\nu$ = 689 eV corresponding to the transition from F1*s* to σ(C–F)*. The PIY intensity of F^+ at $h\nu$ = 689 eV is much stronger than at $h\nu$ = 693 eV corresponding to the transition from F1*s* to σ(C–C)*, while the TEY intensity at $h\nu$ = 689 eV is slightly stronger than that at $h\nu$ = 693 eV. That is, the C–F bond scission by irradiation of photons at $h\nu$ = 689 eV (F1*s* → σ(C–F)*) is expected to occur more effectively than at $h\nu$ = 693 eV(F1*s* → σ(C–C)*). For the case of PVDF, the intense PIY feature of F^+ appears at the transition from F1*s* to σ(C–F)*. The excitation from fluorine 1*s* to σ(C–F)* is specially efficient for F^+ ion production for both PTFE and PVDF.

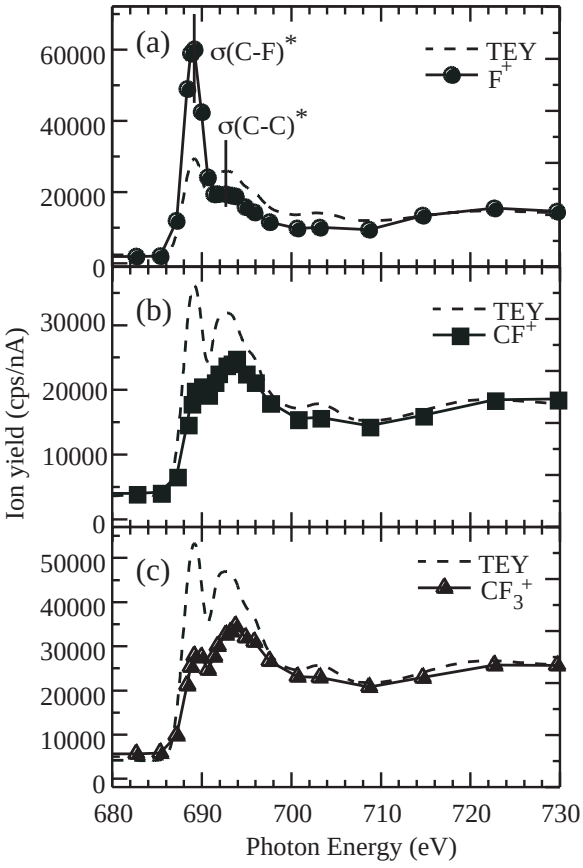

Figure 1. PIY spectra of (a) F^+, (b) CF^+ and (c) CF_3^+ for PTFE thin film near the fluorine *K* absorption edge. TEY spectra (broken curve) are also shown for comparison. TEY spectra are renormalized at $h\nu$ = 682.5 eV and at $h\nu$ = 730 eV to fit PIY intensities.

VIII-V-2 Excited States of Perfluorinated Oligo(p-phenylene) by Inner-Shell Excitation

OKUDAIRA, K. Koji; OHARA, Kosuke[1]; SETOYAMA, Hiroyuki[1]; SUZUKI, Toshiyasu; SAKAMOTO, Youichi[1]; IMAMURA, Motoyasu[2]; HASEGAWA, Shinji; MASE, Kazuhiko[3]; UENO, Nobuo[1]
([1]Chiba Univ.; [2]AIST; [3]IMSS)

[*Nucl. Instrum. Methods Phys. Res., Sect. B* **199**, 265–269 (2003)]

Ion time-of-flight (TOF) mass spectra and near edge x-ray absorption fine structure (NEXAFS) spectra of

perfluorinated oligo(*p*-phenylene) (PF-8P) films near fluorine (F) and carbon (C) *K*-edges were observed. In ion TOF mass spectra near F and C *K*-edges, F^+, CF^+, and CF_3^+ were intensely observed. It indicates that C–C bonds of phenyl ring as well as C–F bonds are broken by irradiation of photons near F and C *K*-edges. Partial ion yield (PIY) spectra of PF-8P show clear $h\nu$ dependence near F and C *K*-edges. Especially, near F *K*-edge, the PIY spectra of F^+ increases remarkably at $h\nu$ = 689.2 eV, which corresponds to the lowest peak in NEXAFS. The lowest peak in the NEXAFS near fluorine *K*-edge is assigned to the transition from F1*s* to σ(C–F)*. Furthermore, from the analysis of PIY spectra of PF-8P near carbon K-edge, the peak at $h\nu$ = 289.5 eV is ascribed to the transition from C1*s* to σ(C–F)*.

VIII-W Electronic Structure and Collision Dynamics of Atoms and Molecules Studied by Electron Impact near the Bethe Ridge

Binary (*e*,2*e*) or electron momentum spectroscopy (EMS), based on the so-called electron Compton scattering, is a high-energy electron-impact ionization experiment in which kinematics of all the electrons are fully determined by coincident detection of the two outgoing electrons. The ability to measure electron momentum distribution for each molecular orbital, square modulus of the momentum-space wavefunction, is a remarkable feature of this technique. Since momentum-space and position-space are uniquely related to each other by Fourier transformation, electron momentum distribution is highly sensitive to diffuse parts of the position-space wavefunction that are important in chemical reaction and molecular recognition. However, the potential of EMS has not been fully achieved as yet, due mainly to the extremely small cross sections involved. For these reasons, together with various improvements to spectrometers we are aiming at developing next-generation EMS for chemistry, which would give quite unique and versatile information on electronic structure of molecules.

VIII-W-1 A High Sensitivity Electron Momentum Spectrometer with Simultaneous Detection in Energy and Momentum

TAKAHASHI, Masahiko; SAITO, Taku[1]; MATSUO, Motoaki[1]; UDAGAWA, Yasuo[1]
([1]Tohoku Univ.)

[*Rev. Sci. Instrum.* **73**, 2242 (2002)]

A new apparatus for electron-electron coincidence experiments has been developed to examine molecular orbital patterns quantitatively by electron momentum spectroscopy. Using a spherical analyzer and position-sensitive detectors, it enables one to measure energy and angular correlations between the two outgoing electrons simultaneously. The design and performance of the apparatus is reported together with results on Ar to show extensive improvements in coincidence count rates and statistical precision, covering a wide range of binding energies and momenta.

VIII-W-2 The Impact Energy Dependence of Momentum Profiles of Glyoxal and Biacetyl and Comparison with Theory at Their High-Energy Limits

TAKAHASHI, Masahiko; SAITO, Taku[1]; HIRAKA, Jyunya[1]; UDAGAWA, Yasuo[1]
([1]Tohoku Univ.)

[*J. Phys. B: At., Mol. Opt. Phys.* **36**, 2539 (2003)]

We report an electron momentum spectroscopy study of the two outermost orbitals of dicarbonyls, glyoxal and biacetyl. The experiments were performed at impact energies of 800, 1200 and 1600 eV by using a recently developed multichannel (*e*,2*e*) spectrometer. The experimental momentum profiles clearly show remarkable variations in the low momentum region with increase in impact energy. Furthermore, it has been found that the two molecules reach their high-energy limits at different impact energies, indicating that the range of the validity of the plane-wave impulse approximation (PWIA) largely depends on the target in question. The results at 1600 eV are employed for comparisons with PWIA calculations using Hartree-Fock and density functional theory (DFT). While the DFT calculations reproduce well the observations for glyoxal, considerable discrepancies between experiment and theory exist in biacetyl.

VIII-W-3 (*e*,2*e*) Ionization-Excitation of H_2

TAKAHASHI, Masahiko; KHAJURIA, Yugal; UDAGAWA, Yasuo[1]
([1]Tohoku Univ.)

[*Phys. Rev. A* in press]

Binary (*e*,2*e*) measurements are reported for simultaneous ionization-excitation processes of H_2. The experiments were performed at impact energies of 1200, 1600 and 2000 eV using an energy- and momentum-dispersive spectrometer. Momentum profiles for transitions to the $2s\sigma_g$ and $2p\sigma_u$ excited final ion states are presented as normalized intensities relative to the cross section of the primary ionization to the $1s\sigma_g$ ground ion state. The results are compared with theoretical calculations of Lermer *et al.* [*Phys. Rev. A* **56**, 1393 (1997)] using the first-order plane-wave impulse approximation. Certain features of the discrepancies between experiment and theory can be explained by incorporating contributions from the second-order two-step mechanisms into the (*e*,2*e*) cross sections. Furthermore, the present results suggest that $2s\sigma_g$ and $2p\sigma_u$ cross sections approach their high-energy limits in different ways.

VIII-W-4 Electron Momentum Spectroscopy of N_2O

KHAJURIA, Yugal; TAKAHASHI, Masahiko; UDAGAWA, Yasuo[1]
([1]Tohoku Univ.)

[*J. Electron Spectrosc.* in press]

An electron momentum spectroscopy study of the outer valence orbitals of N_2O is reported. The experi-

ments were performed at impact energies of 1000, 1200, 1600 and 1800 eV by using a recently developed multichannel (*e*,2*e*) spectrometer. The experimental momentum profiles are compared with each other to examine their impact energy dependence. The results are used for comparisons with Hartree-Fock (HF) and density functional theory (DFT) calculations using various basis sets. The DFT and HF calculations with large basis sets are in good agreement with the measured electron momentum profiles, with the exception of that of the 6σ orbital for which the HF method underestimates the cross sections in the low momentum region.

VIII-W-5 A High Sensitivity Electron Momentum Spectrometer with Two-Dimensional Detectors and Electron Momentum Distributions of Several Simple Molecules

TAKAHASHI, Masahiko; UDAGAWA, Yasuo[1]
([1]Tohoku Univ.)

[*J. Electron Spectrosc.* submitted]

Electron momentum spectroscopy (EMS) makes it possible to examine orbital patterns of individual molecular orbitals in momentum space. A new spectrometer for electron-electron coincidence experiments for EMS has been developed to obtain orbital patterns quantitatively. Using a spherical analyzer and position-sensitive two-dimensional detectors combined with fast electronics, simultaneous measurements of energy and angular correlations between the two outgoing electrons can be made. This spectrometer features high sensitivity and an ease of changing impact energies. Details of the apparatus are described and impact energy dependence of electron momentum distributions of the HOMO of H_2 and biacetyl are compared.

VIII-W-6 Electron-Impact Double Ionization Mechanisms in the Impulsive Regime

VAN BOEYEN, Roger W.[1]; WATANABE, Noboru; DOERING, John P.[1]; MOORE, John H.[2]; COPLAN, Michael A.[2]; COOPER, John W.[2]
([1]Johns Hopkins Univ., USA; [2]Univ. Maryland, USA)

[*Phys. Rev. Lett.* submitted]

Five-fold differential cross sections (5DCS) for the electron-impact double ionization of the 3*s* electrons of magnesium have been measured in a high-impact-energy, high-momentum-transfer regime within the ionization mechanisms can be accurately described by simple models in which the ionization processes and the initial-state atomic properties can be separated. In the unique experimental geometry, the form of the measured cross sections provides strong evidence for impulsive two-collision ionization mechanisms. Second Born calculations are in agreement with the experimental data providing further evidence for the mechanisms. The implications for the measurement of two-electron densities are discussed.

VIII-W-7 Second Born Approximation Calculations of Double Ionization of Mg

WATANABE, Noboru; COOPER, John W.[1]; VAN BOEYEN, Roger W.[2]; MOORE, John H.[1]
([1]Univ. Maryland, USA; [2]Johns Hopkins Univ., USA)

Electron impact double ionization, also called the (*e*,3*e*) reaction, can provide direct information on correlated motion of atomic electrons, provided that the collision mechanism is known. Possible mechanisms for the (*e*,3*e*) reaction include shake-off (SO), two-step 1 (TS1), and two-step 2 (TS2). The SO and TS1 are of the first order in the projectile-target interaction, while the TS2 is a second-order process. In this study we theoretically examine contributions from TS2 in the scattering geometry chosen for the (*e*,3*e*) experiments of the Maryland group, which investigate correlated motion of the 3*s* electrons in the magnesium atom. It has been found that dominant contribution from the Second Born term is involved in the observed (*e*,3*e*) cross sections of Mg. Electron correlation effects in the initial target state are also studied using a configuration interaction wave function.

VIII-W-8 Orbital Momentum Profiles and Binding Energy Spectra for the Complete Valence Shell of CO

SAITO, Taku[1]; TAKAHASHI, Masahiko; UDAGAWA, Yasuo[1]
([1]Tohoku Univ.)

Electron momentum profiles and binding energy spectra for the complete valence shell of CO have been measured using an energy- and momentum-dispersive (*e*,2*e*) spectrometer at an impact energy of 1600 eV. It has been found that shapes of the orbital momentum profiles are well reproduced by Hartree-Fock calculations. Binding energy spectra and momentum profiles in the satellite region beyond 22 eV binding energy of CO are studied in detail, determining pole sterngth distributions of the molecule. Comparisions are made for the pole strength distributions with theoretical predictions of Ehara and Nakatsuji using the SAC-CI general-R method. The agreement between experiment and theory is generally good, but some discrepancies remain for ionization transitions with small pole strength lower than about 0.1.

VIII-W-9 (*e*,2*e*) Study on Ionization-Excitation and Double Ionization of He

TAKAHASHI, Masahiko; UDAGAWA, Yasuo[1]
([1]Tohoku Univ.)

A binary (*e*,2*e*) study has been carried out for He at an impact energy of 2000 eV using a recently developed energy- and momentum-dispersive spectrometer. Binding energy and momentum ranges up to about 100 eV and 4 au were then covered. Momentum distributions of the individual ionization-excitation transitions, converging to the double ionization threshold, have been compared with first-order plane-wave impulse

calculations of Mitroy *et al.* [*J. Phys. B* **18**, 4149 (1985)]. For the primary ionization that leaves the residual He^+ ion in the $n = 1$ ground state, agreement between experiment and theory is satisfactory. On the other hand, for ionization-excitation that leads to change of state of both the two target electrons the experiments always exhibit larger intensity than theory, suggesting noticeable contributions from the second-order two step mechanisms.

VIII-W-10 Development of a Triple Coincidence Spectrometer for a Complete Three-Dimensional Mapping of Electron Momentum Densities in Gaseous Molecules

TAKAHASHI, Masahiko; WATANABE, Noboru; UDAGAWA, Yasuo[1]; ELAND, John H. D.[2]
([1]Tohoku Univ.; [2]Oxford Univ., England)

Electron momentum spectroscopy has been developed as a powerful means for the investigation of electronic structure and electron correlation. In particular, the ability to measure electron momentum distribution for each molecular orbital, square modulus of the momentum-space wavefunction, is a remarkable feature of this technique. It is unfortunate, however, that experimentally observable electron momentum distribution is spherically averaged due to random orientation of gaseous targets, smearing out details of electronic structure inherently involved in the experiments.

To overcome the experimental difficulty a new apparatus has been developed for a complete three-dimensional mapping of electron momentum densities in gaseous molecules. Based on the axial recoil, measurements of vector correlations among the two outgoing electrons and fragment ion correspond to (*e*,2*e*) experiments with oriented molecules. Dissociation of molecular ions perpendicular to the incident electron momentum vector are detected with seven independent channeltrons, while the two outgoing electrons are detected with a pair of position-sensitive detectors. A schematic diagram of the kinematics of our experiments is shown in Figure 1.

Although there are substantial backgrounds due to a huge number of fragment ions produced by forward scattering of electron projectile, we have successfully measured genuine triple coincidence signals for the first time. Figure 2 shows an example of the results, which plots directional electron momentum densities obtained for the $2\sigma_g$ ionization of O_2. While the statistics of the data is not satisfactory, we can clearly see anisotropy of electron momentum densities. For establishing this method developments in detection of the outgoing electrons in the momentum dispersive plane around full 2π azimuth are now in progress to increase sensitivity of two additional orders of magnitude.

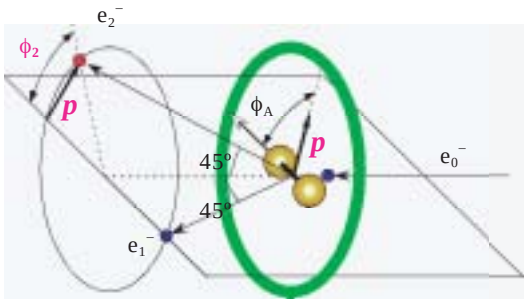

Figure 1. Schematic diagram of the kinematics of the (*e*,2*e*) directional momentum density experiment. The spectrometer records only the component of momentum perpendicular to the scattering plane. When dissociation takes place in the perpendicular plane, the channeltron detectors will record the arrival of the dissociation products.

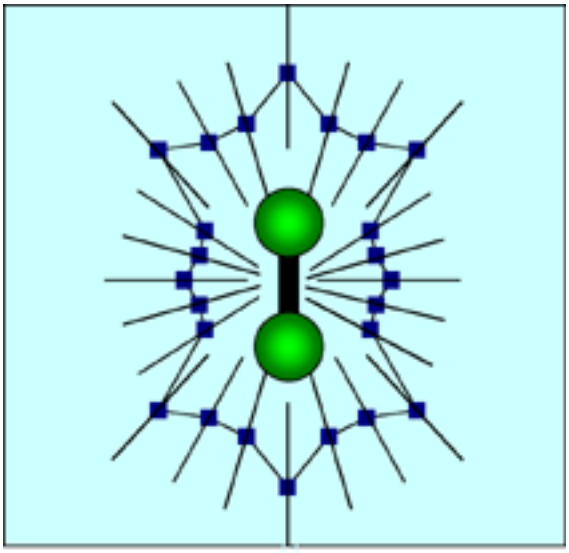

Figure 2. Directional electron momentum densities for the $2\sigma_g$ orbital ionization of O_2.

VIII-X Electronic Structure and Collision Dynamics of Atoms and Molecules Studied by Photon Impact

The group takes another, photon-impact, approach to issues of electronic structure and collision dynamics, since photon-impact and electron-impact or photoelectric effects and Compton scattering are complementary to each other.

VIII-X-1 Multilayer Polarizers for the Use of He-I and He-II Resonance Lines

HATANO, Tadashi[1]; KONDO, Yuzi[1]; SAITO, Katsuhiko[1]; EJIMA, Takeo[1]; WATANABE, Makoto[1]; TAKAHASHI, Masahiko
([1]Tohoku Univ.)

[*Surf. Rev. Lett.* **9**, 587 (2002)]

Multilayer polarizers for the use of He resonance lines have been developed. Si/Mg and SiC/Mg multilayers were designed and fabricated for the He-I and He-II resonance lines, respectievely. The performance was checked by the use of synchrotron radiation. The polarizance and *s*-reflectance of the He-II polarizer measured at an angle of incidence of 40° were 0.98 and 41%, respectievely. The polarizance of the He-I polarizer measured at an angle of incidence of 31.5° was 0.96.

VIII-X-2 Polarization Measurements of Laboratory VUV Light: A First Comparison between Multilayer Polarizers and Photoelectron Angular Distributions

TAKAHASHI, Masahiko; HATANO, Tadashi[1]; EJIMA, Takeo[1]; KONDO, Yuzi[1]; SAITO, Katsuhiko[1]; WATANABE, Makoto[1]; KINUGAWA, Tohru[2]; ELAND, John H. D.[2]
([1]Tohoku Univ.; [2]Oxford Univ., England)

[*J. Electron Spectrosc.* **130**, 79 (2003)]

The use of photoelectron angular distributions to determine the linear polarization of VUV light over a wide range of photon energies is demonstrated. Light at wavelengths from 25.6 to 73.6 nm, partially polarized by large angle reflections in a toroidal grating monochromator and at a refocus mirror, has been analyzed. The results are validated by comparison measurements at spot wavelengths using multilayer polarizers.

VIII-X-3 Carbon *K*-Shell Photoelectron Angular Distribution from Fixed-in-Space CO_2 Molecules

SAITO, Norio[1]; FANIS, Albert De[2]; KUBOZUKA, Kenichiro[3]; MACHIDA, Masatake[3]; TAKAHASHI, Masahiko; YOSHIDA, Hiroaki[4]; SUZUKI, Isao H.[1]; CASSIMI, Amine[5]; CZASCH, Achim[6]; DÖRNER, Reinhard[6]; WANG, Kwanghsi[7]; ZIMMERMANN, Björn[7]; MCKOY, Vincent[7]; KOYANO, Inosuke[3]; UEDA, Kiyoshi[2]
([1]Natl. Metrology Inst.; [2]Tohoku Univ.; [3]Himeji Inst. Tech.; [4]Hiroshima Univ.; [5]Univ. Caen, France; [6]Univ. Frankfurt, Germany; [7]California Inst. Tech., USA)

[*J. Phys. B: At., Mol. Opt. Phys.* **36**, L25 (2003)]

Measurements of photoelectron angular distributions for carbon *K*-shell ionization of fixed-in-space CO_2 molecules with the molecular axis oriented along, perpendicular and at 45° to the electric vector of the light are reported. The major features of these measured spectra are fairly well reproduced by calculations employing a relaxed-core Hartree-Fock approach. In contrast to the angular distribution for *K*-shell ionization of N_2, which exhibits a rich structure dominated by the f-wave (l = 3) at the shape resonance, the angular distribution for carbon *K*-shell photoionization of CO_2 is quite unstructured over the entire observed range across the shape resonance.

VIII-X-4 N 1*s* Photoionization Cross Sections of the NO Molecules in the Shape Resonance Region

HOSAKA, Kouichi[1]; ADACHI, Junichi[1,2]; TAKAHASHI, Masahiko; YAGISHITA, Akira[1,2]
([1]Tokyo Univ.; [2]KEK-PF)

[*J. Phys. B: At., Mol. Opt. Phys.* in press]

The N 1*s* partial photoionization cross sections of NO leading for the $^3\Pi$ and $^1\Pi$ ionic states have been measured in the shape resonance region for the first time. The twin local maxima in the cross sections have been tentatively assigned, based on the simple models for the photoabsorption intensities and for the branching ratio of the $^3\Pi$ and $^1\Pi$ ionic states from the σ^* shape resonance state.

VIII-X-5 Multiplet-Specific N 1*s* Photoelectron Angular Distributions from the Fixed-in-Space NO Molecules

HOSAKA, Kouichi[1]; ADACHI, Junichi[1,2]; TAKAHASHI, Masahiko; YAGISHITA, Akira[1,2]; LIN, Ping[3]; LUCCHESE, Robert R.[3]
([1]Tokyo Univ.; [2]KEK-PF; [3]Texas A&M Univ., USA)

[*Phys. Rev. Lett.* submitted]

Angular distributions of multiplet-specific N 1*s* photoelectrons from the fixed-in-space NO molecules have been measured for the first time. The dynamics of the σ^* shape resonance appeared in the channel leading to the $^3\Pi$ and $^1\Pi$ ionic states has been made clear from the analyses of the angular distributions. Multiplet-specific multichannel calculations have reproduced the observed angular distributions fairy well.

VIII-X-6 Shape-Resonance-Enhanced Vibrational Effects in the Angular Distributions of C 1*s* Photoelectrons from Fixed-in-Space CO Molecules

ADACHI, Junichi[1,2]; HOSAKA, Kouichi[1]; FURUYA, Shuusaku[3]; SOEJIMA, Kouich[3]; TAKAHASHI, Masahiko; YAGISHITA, Akira[1,2]; SEMENOV, Sergei K.[4]; CHEREPKOV, Nikolai A.[4]
([1]Tokyo Univ.; [2]KEK-PF; [3]Niigata Univ.; [4]State Univ. Aerospace Instrum., Russia)

[*Phys. Rev. Lett.* in press]

Angular distributions of C1*s* photoelectrons from fixed-in-space CO molecules have been measured with

vibrational resolution. A strong dependence of the angular distributions on the vibrational states of the residual molecular ion has been found for the first time in the region of the shape resonance. Calculations in the relaxed core Hartree-Fock approximation have reproduced the angular distributions fairly well in the general shapes of the angular distributions due to the correct description of nuclear motion as an average of the internuclear-distance-dependent dipole amplitudes.

VIII-X-7 Angular Distributions of Vibrationally Resolved C 1*s* Photoelectrons from Fixed-in-Space CO Molecules: Vibrational Effect in the Shape-Resonant C 1*s* Photoionization of CO

ADACHI, Junichi[1,2]; HOSAKA, Kouichi[1]; FURUYA, Shuusaku[3]; SOEJIMA, Kouich[3]; TAKAHASHI, Masahiko; YAGISHITA, Akira[1,2]; SEMENOV, Sergei K.[4]; CHEREPKOV, Nikolai A.[4]
([1]Tokyo Univ.; [2]KEK-PF; [3]Niigata Univ.; [4]State Univ. Aerospace Instrum., Russia)

[*J. Electron Spectrosc.* submitted]

We have measured molecular-frame photoelectron angular distributions (MF-PAD) for the vibrationally resolved C1*s* photoelectron from CO molecule in the s shape resonance region. The MF-PAD's for the v_f = 0,1, and 2 levels in the C1*s* → ε*l*σ channel are apparently different each other at each incident photon energy. These MF-PAD's agree woth the present theoretical results from the averaging the nuclear distance dependent dipole matrix elements with the relaxed core Hartree-Fock calculations. The present results show that the internuclear distance dependences of the phase and of the magnitude of the dipole matrix element play a crucial role in the C1*s* photoionization of CO.

VIII-X-8 Coulomb Hole in N_2, CO and O_2 Deduced from X-Ray Scattering Cross Sections

WATANABE, Noboru; KAMATA, Yohei[1]; YAMAUCHI, Kota[1]; UDAGAWA, Yasuo[1]; MÜLLER, Thomas[2]
([1]Tohoku Univ.; [2]Res. Cent. Jülich, Germany)

Total (elastic + inelastic) x-ray scattering cross sections $\sigma_{ee}(q)$ are very sensitive to electron correlation effects, since they are related to the Fourier transform of the radial electron-electron pair distribution function $P(r_{12})$.[1)] X-ray scattering experiments can hence provide a crucial check of whether or not a theoretical wave function takes electron correlation properly into consideration.

In this study, accurate $\sigma_{ee}(q)$ of N_2, CO and O_2 were measured by the use of the energy dispersive method up to a momentum transfer of q =12 *a.u.* $P(r_{12})$ was extracted from the cross sections. The Coulomb hole, defined as the difference between the exact $P(r_{12})$ and the corresponding function evaluated at Hartree-Fock limit, has been derived from experimental data. Comparison with configuration interaction calculations shows small but systematic differences between the theoretical and experimental results.

Reference

1) N. Watanabe *et al.*, *Review of Modern Quantum Chemistry*, K. D. Sen, Ed., World Scientific; Singapore, 553 (2002).

VIII-X-9 Absolute Surface Coverage Measurement Using a Vibrational Overtone

PIPINO, Andrew C. W.[1]; HOEFNAGELS, Johan P. M.[2]; WATANABE, Noboru
([1]Natl. Inst. Standards Tech., USA; [2]Eindhoven Univ. Tech., Netherland)

Sub-monolayer absolute surface number densities are obtained by cavity ring-down spectroscopy (CRDS) for trichloroethylene, cis-dichloroethylene, and trans-dichloroethylene adsorbed on silica using the first C–H stretching overtones, which are probed with the idler of a seeded optical parametric amplifier having a 0.075 cm^{-1} line width. The absolute surface number densities are found by invoking conservation of the integrated band intensity with adsorption together with knowledge of the transition moment orientation as derived from the adsorbate polarization anisotropy. The evanescent wave CRDS (EW-CRDS) measurements employ a fused-silica monolithic folded resonator with a peak finesse of ≈ 28,500 at 1650 nm. The absolute coverage of trichloroethylene on SiO_2 is also obtained by a mass-spectrometer-based surface-uptake technique, which is briefly contrasted with the EW-CRDS method. The sensitivity of EW-CRDS for trichloroethylene detection with an unclad resonator is found to be comparable to that obtained with a long-effective-path-length waveguide having a trichloroethylene-enriching polysiloxane coating.

VIII-Y Study on Compact X-Ray Sources

Electron storage rings are useful devices as x-ray sources. However, these synchrotron radiation facilities usually occupy large area and cost much. So that there have been many works to investigate compact x-ray sources using small electron accelerators. It is also useful to use laser undulator radiation or backward Compton scattering caused by the interactions of electron beams with laser photons, if we provide enough electrons to produce practical intensity of x-rays. RF-photocathode would produce high peak intensity electron beam so that it is a useful candidate of a electron source. It is necessary to search good materials as the photocathode for construction of a practical compact x-ray source. Cesium telluride has reported to have a good quantum efficiency, so that we have studied about it.

In order to generate high brilliant x-rays using small electron accelerators, we propose metal multi-foils as the target irradiated by the electron beam. We have studied x-ray intensity generated from the multi-foil target using Monte Carlo simulation code.

VIII-Y-1 Feasibility Study of X-Ray Generation by Using Metal Multi-Foil Target Irradiated by High Energy Electron Beam

TAKASHIMA, Yoshifumi; KOBAYAKAWA, Hisashi[1]; MATSUBARA, Masahide[1]
([1]Nagoya Univ.)

We performed feasibility study of x-ray source using metal multi-foil target irradiated by high energy electrons. Figure1 shows the sketch of the setup. High energy electron beams extracted from small accelerators are incident on metal multi-foil targets with small angles. X-rays generated in the foils by bremsstrahlung are reflected on the surface of the next foils if the incident angle is small enough to satisfy the total reflection condition.

We calculate the spectrum and angular spread of the x-rays radiated from the multi-foil targets by using EGS4[1)] simulation code. Figure 2 shows the geometry used in the EGS4 calculation. We use stacks of copper foils as the target. The thickness, width and length of a foil are 0.1 μm, 100 mm and 500 mm, respectively. We stack 100 foils as the target for EGS4 calculation. Incident electron energy was 150 MeV and the incident angle of the electron on the surface of the target was 1 mrad.

Figure 3 shows the angular spread of 5keV x-rays using multi-foil and bulk targets. The total thickness of the multi-foil is 10 μm which is the same thickness of the bulk target. The yield of the x-rays from multi-foil target is larger than that from the bulk target because of the reflection of x-rays between the foils.

The energy spectra of x-rays from the multi-foil and bulk targets are shown in Figure 4. X-ray intensity radiated from multi-foil is larger than bulk target in the low energy region, because low energy x-rays have large total reflection angles so that it is not absorbed in the target material but extracted by reflection between foils.

We calculated the spectrum and angular distribution of x-rays generated from metal multi-foils irradiated by high energy electrons using EGS4 simulation code. For further study, we should include the effect of transition radiation in the calculation in order to estimate x-ray intensity more precisely.

Reference

1) W. R. Nelson, H. Hirayama and D. W. O. Rogers, SLAC-Report-256, (1985).

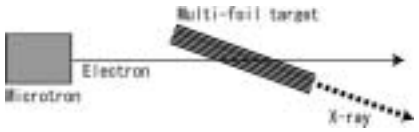

Figure 1. Sketch of experimental setup using multi-foil target.

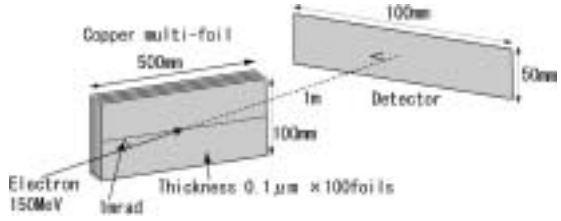

Figure 2. Geometry used in EGS4 simulation.

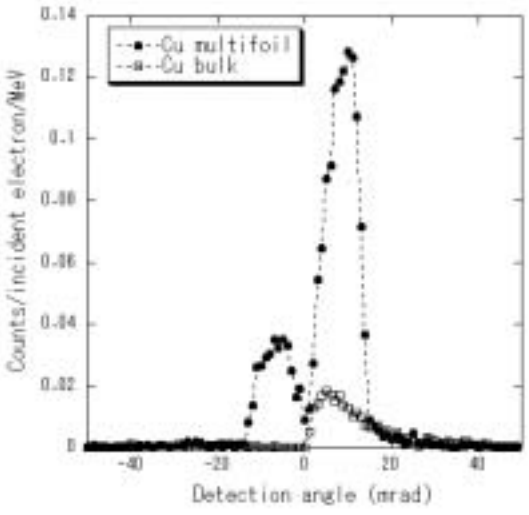

Figure 3. Angular distribution of x-rays generated from multi-foil and bulk targets.

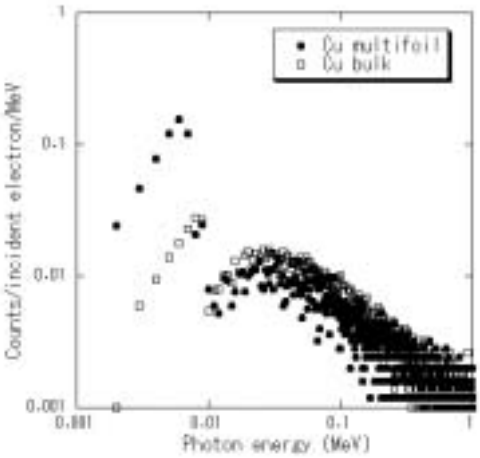

Figure 4. Energy spectrum of x-rays generated from multi-foil and bulk targets.

VIII-Z Syntheses of Fullerene-Based New Materials with Novel Physical Properties and Their Application toward New-Generation Electronic Devices

Fullerene-based new materials are synthesized and their structures and electronic properties are studied in solid, thin film and nanometer scale. The crystal structures of metallofullerene solids are determined by Rietveld refinements for X-ray diffraction patterns with synchrotron radiation. The resistivity and field effect transistor (FET) characteristics are studied with thin films of metallofullerens and higher-fullerenes. Furthermore, the scanning tunneling microscopy (STM) and scanning tunneling spectroscopy (STS) of metallofullerenes deposited onto the well-defined semiconducting surfaces are studied under ultrahigh vacuum.

VIII-Z-1 Crystal Structure and Electronic Transport of Dy@C_{82}

KUBOZONO, Yoshihiro; TAKABAYASHI, Yasuhiro[1]; SHIBATA, Kana[2]; KANBARA, Takayoshi[2]; FUJIKI, Satoshi; KASHINO, Setsuo[2]; FUJIWARA, Akihiko[3]; EMURA, Shuichi[4]
([1]IMS and Okayama Univ.; [2]Okayama Univ.; [3]JAIST; [4]Osaka Univ.)

[*Phys. Rev. B* **67**, 115410 (2003)]

The crystal structure of Dy@C_{82} isomer I at 298 K has been determined by Rietveld refinement for x-ray powder diffraction with synchrotron radiation. Isomer I shows a simple cubic structure (sc: $Pa\bar{3}$) with a lattice constant a of 15.78(1) Å. The C_2 axis of a C_{2v}-C_{82} cage aligns along the [111] direction of this crystal lattice. The C_{82} cage is orientationally disordered to satisfy a $\bar{3}$ symmetry along [111], which is requested in this space group. The large thermal parameter for the Dy atom estimated from the x-ray diffraction probably reflects a large disorder caused by a floating motion of the Dy atom inside the C_{82} cage as well as a ratchet-type motion of the Dy@C_{82} molecule. The electronic transport of thin film of Dy@C_{82} shows a semiconducting behavior. The energy gap E_g is estimated to be 0.2 eV. Further, the variation of valence from Dy^{3+} to Dy^{2+} is found by metal doping into the Dy@C_{82} crystals.

VIII-Z-2 Synthesis, Structure, and Magnetic Properties of the Fullerene-Based Ferromagnets, Eu_3C_{70} and Eu_9C_{70}

TAKENOBU, Taishi[1]; CHI, Dam Hieu[2]; MARGADONNA, Serena[3]; PRASSIDES, Kosmas[4]; KUBOZONO, Yoshihiro; FITCH, Andrew N.[5]; KATO, Ken-ichi[6]; IWASA, Yoshihiro[1]
([1]Tohoku Univ.; [2]JAIST; [3]Univ. Cambridge; [4]Univ. Sussex; [5]European Synchrotron Radiation Facility; [6]JASRI)

[*J. Am. Chem. Soc.* **125**, 1897 (2003)]

Intercalation of C_{70} with europium affords two kinds of magnetic compounds, a canted antiferromagnet Eu_xC_{70}($x \approx 3$) and a ferromagnet Eu_xC_{70}($x \approx 9$) with transition temperatures (T_c) of 5 and 38 K, respectively. The Curie constants in the paramagnetic phase and the saturation moment in the ferromagnetic phase are both understood by the full moment of Eu^{2+} for both systems. The structure of $Eu_{3-\delta}C_{70}$ ($\delta \approx 0.27$) is pseudo-monoclinic, derived by a simple deformation of the parent face-centered cubic (*fcc*) structure. $Eu_{9-\delta}C_{70}$ ($\delta \approx 0.2$) forms an *fcc* structure, in which cuboctahedral clustering of Eu^{2+} ions is observed in the enhanced size octahedral holes. The observed T_c of the $Eu_{9-\delta}C_{70}$ ferromagnet is comparable to or larger than those of simple binary Eu-based ferromagnets, such as Eu chalcogenides or carbides, despite the low atomic ratio of Eu in the chemical formulas. This can be understood by the short Eu^{2+}–Eu^{2+} distances and high coordination numbers permitted by the multiple occupation by Eu^{2+} ions of the expanded octahedral interstitial sites in higher fullerene-based solids.

VIII-Z-3 Pressure-Induced Structural Phase Transition in Fullerides Doped with Rare Earth Metals

CHI, Dam Hieu[1]; IWASA, Yoshihiro[1,2]; UEHARA, Katsuyuki[1]; TAKENOBU, Taishi[2]; ITO, Takayoshi[1]; MITANI, Tadaoki[1]; NISHIBORI, Eiji[3]; TAKATA, Masaki[3,4]; SAKATA, Makoto[3]; OHISHI, Y.[4]; KATO, Ken-ichi[4]; KUBOZONO, Yoshihiro
([1]JAIST; [2]Tohoku Univ.; [3]Nagoya Univ.; [4]JASRI)

[*Phys. Rev. B* **67**, 94101 (2003)]

Rare-earth-metal-doped fullerides with nominal composition of R_3C_{70} (R = Sm, Eu) adopt a pseudo-monoclinic structure in which C_{70} dimers glued with rare-earth ions are involved. High-pressure powder x-ray diffraction experiments revealed that these compounds undergo a reversible first-order structural phase transition at 1.5 GPa, associated with 2.7%–2.9% reduction of the unit cell volume. Structural analyses showed that the rare-earth ions, which are located close to the edge of tetrahedral sites at ambient pressure, move back to the center of the tetrahedral sites. Simultaneously, C_{70} molecules are realigned so that the fivefold (long) axes are perpendicular to the $(10\bar{1})$ or $(11\bar{1})_{fcc}$ plane at high pressure. The derived charge density map indicates that the transition is regarded as a structural change from dimers to three-dimensional polymers of fullerenes. These features are ascribed to the unique bonding nature in rare-earth C_{70} compounds.

VIII-Z-4 Molecular- and Atomic-Like Photoionization of C_{60} in the Extreme Ultaviolet

KOU, Junkei; MORI, Takanori; ONO, Masaki; HARUYAMA, Yusuke[1]; KUBOZONO, Yoshihiro[2]; MITSUKE, Koichiro
([1]Okayama Univ.; [2]IMS and Okayama Univ.)

[*Chem. Phys. Lett.* **374**, 1 (2003)]

Photoion yield spectra of C_{60} in the gas phase were measured from 23 to 180 eV by synchrotron radiation. Two peaks at 26 and 34 eV and a flat area ranging 40–50 eV are newly observed in the high-energy side of the giant resonance at ~ 20 eV. These features are assigned to the shape resonance on photoionization of the valence electrons of C_{60}; the ionized electron is temporarily trapped inside a centrifugal barrier. Above ~ 50 eV the yield curve shows a steady decrease with increasing photon energy like the photoabsorption cross section of atomic carbon. Thus, the spectrum is interpreted as essentially determined by photoionization of the 2*s* orbitals of carbon atoms.

VIII-Z-5 A Complex Fulleride Superstructure-Decoupling Cation Vacancy and Anion Orientational Ordering in $Ca_{3+x}C_{60}$ with Maximum Entropy Methods

CLARIDGE, J. B.[1]; KUBOZONO, Yoshihiro; ROSSEINSKY, M. J.[1]
([1]Univ. Liverpool)

[*Chem. Mater.* **15**, 1830 (2003)]

The structure of the alkaline-earth fulleride $Ca_{3.01}C_{60}$ is refined using maximum entropy data analysis of synchrotron powder diffraction data. Despite the size and complexity of the structural problem, the fulleride anion orientations and the details of multiple occupancy of the octahedral interstitial sites in the fcc anion array are determined. The power of the maximum entropy technique in solving underdetermined problems in powder crystallography is thus demonstrated.

VIII-Z-6 Development of a Photoionizaion Spectrometer for Gaseous Fullerenes in the Extreme Ultraviolet

MORI, Takanori; ONO, Masaki; KOU, Junkei; HARUYAMA, Yusuke[1]; KUBOZONO, Yoshihiro; MITSUKE, Koichiro
([1]Okayama Univ.)

[*Rev. Sci. Instrum.* **74**, 3769 (2003)]

A photoionization spectrometer has been developed for measuring the ion yields for fullerenes in the photon energy range of 23–200 eV. Gaseous fullerenes were supplied from a high-temperature oven, ionized by irradiation of monochromatized synchrotron radiation, and detected after analysis with a time-of-flight mass spectrometer. The fluxes of the synchrotron radiation and fullerene beams were monitored concurrently with the acquisition of the ion signal counts in order to obtain reliable photoionization efficiency curves. The performance of the apparatus was examined by measuring the efficiency curve of C_{60}^+ produced from C_{60}. The spectrum demonstrated better statistics than the previous results in the same photon energy region. Three distinct features were newly observed in the higher-energy side of the prominent resonance at ~ 20 eV.

VIII-Z-7 Structural and Electronic Properties of $Ce@C_{82}$

SHIBATA, Kana[1]; RIKIISHI, Yoshie[1]; HOSOKAWA, Tomoko[1]; HARUYAMA, Yusuke[1]; KUBOZONO, Yoshihiro[2]; KASHINO, Setsuo[1]; URUGA, Tomoya[3]; FUJIWARA, Akihiko[4]; KITAGAWA, Hiroshi[5,6]; TAKANO, Takumi[7]; IWASA, Yoshihiro[7]
([1]Okayama Univ.; [2]IMS, JST and Okayama Univ.; [3]JASRI; [4]JAIST; [5]Univ. Tsukuba; [6]PRESTO/JST; [7]Tohoku Univ.)

[*Phys. Rev. B* **68**, 94104 (2003)]

X-ray diffraction patterns for a solid sample of $Ce@C_{82}$ that contains a mixture of two isomers, I and II, can be indexed in a face-centered cubic lattice with a lattice constant of 15.88(5) Å, while x-ray diffraction patterns for $Ce@C_{82}$ isomer I alone indicate a simple cubic lattice with a lattice constant of 15.78(1) Å. Rietveld refinement for the x-ray diffraction pattern of the latter, $Ce@C_{82}$ isomer I, has been carried out with a space group of $Pa\bar{3}$. Thin films of $Ce@C_{82}$ were first prepared by thermal deposition under ~ 10^{-7} Torr. The Raman spectra for these thin films show a peak ascribable to a Ce-C_{82} cage-stretching mode at ~ 160 cm^{-1}, implying that the valence of Ce in this structure is +3. This valence of +3 is supported by Ce L_{III}-edge XANES for a thin film of $Ce@C_{82}$. Furthermore, the local structure around the Ce ion could be determined by Ce L_{III}-edge EXAFS for a thin-film. Transport properties of a thin film of $Ce@C_{82}$ have been studied by a four-probe method, and these demonstrate a semiconducting behavior with a small gap of 0.4 eV.

VIII-Z-8 N-Channel Field Effect Transistors with Fullerene Thin Films and Their Application to a Logic Gate Circuit

KANBARA, Takayoshi[1]; SHIBATA, Kana[1]; FUJIKI, Satoshi; KUBOZONO, Yoshihiro[2]; KASHINO, Setsuo[1]; URISU, Tsuneo; SAKAI, Masahiro; FUJIWARA, Akihiko[3]; KUMASHIRO, Ryotaro[4]; TANIGAKI, Katsumi[4]
([1]Okayama Univ.; [2]IMS and Okayama Univ.; [3]JAIST; [4]Osaka Univ.)

[*Chem. Phys. Lett.* **379**, 223 (2003)]

N-channel field effect transistors (FETs) were fabricated with thin films of C_{60} and $Dy@C_{82}$. A typical enhancement-type FET property was observed in C_{60} FET above 220 K. The mobility of C_{60} FET increased with increasing temperature. This fact suggests hopping

transport as the conduction mechanism, with the activation energy of 0.29 eV. The Dy@C_{82} FET was found to be a normally-on type FET, which has a property different from that for C_{60} and C_{70} FETs. A complementary metal oxide semiconductor (CMOS) logic gate circuit was first fabricated with C_{60} and pentacene thin-film FETs.

VIII-Z-9 Scanning Tunneling Microscopy of Dy@C_{82} and Dy@C_{60} Adsorbed on Si(111)-(7x7) Surfaces

FUJIKI, Satoshi[1]; KUBOZONO, Yoshihiro[1]; HOSOKAWA, Tomoko[2]; KANBARA, Takayoshi[3]; FUJIWARA, Akihiko[4]; NONOGAKI, Youichi; URISU, Tsuneo
([1]IMS and Okayama Univ.; [2]Okayama Univ.; [3]Tohoku Univ.; [4]JAIST)

[*Phys. Rev. B* in press]

Dy@C_{82} and Dy@C_{60} adsorbed on Si(111)-(7×7) surface are investigated by scanning tunneling microscopy (STM) at 295 K. The Dy@C_{82} molecules in the first layer are adsorbed on Si(111)-(7×7) surface without formation of islands and nucleation, and the internal structure of the Dy@C_{82} molecule is first observed on the surface at 295 K. The average heights of the Dy@C_{82} molecule in the first and second layers are estimated to be 7.2 and 10.8 Å, respectively, by STM. These results suggest strong interactions between the Si atoms and the Dy@C_{82} molecules in the first layer. The STM image reveals that Dy@C_{60} molecule is nearly spherical, showing that the metal endohedral C_{60} possesses a cage-form structure.

VIII-Z-10 Preferred Locations of Metal Ions in Two M@C_{82} Isomers

TAKABAYASHI, Yasuhiro[1]; HARUYAMA, Yusuke[1]; RIKIISHI, Yoshie[1]; HOSOKAWA, Tomoko[1]; SHIBATA, Kana[1]; KUBOZONO, Yoshihiro[2]
([1]Okayama Univ.; [2]IMS and Okayama Univ.)

[submitted]

Location of metal ion in the minor isomer of M@C_{82} (M: metal ion with valence of +3) was determined for the first time by Dy L_{III}-edge EXAFS of Dy@C_{82}. The Dy ion lied near the fused bond between two hexagon rings. On the other hand, the EXAFS showed that the Dy ion in the major isomer of Dy@C_{82} lied near the center of a hexagon ring. The locations found in the minor and major isomers were consistent with those predicted theoretically for the respective isomers.

VIII-Z-11 Fabrication and Characterization of a New Type of Carbon Cluster Field Effect Transistor

SHIBATA, Kana[1]; KUBOZONO, Yoshihiro[2]; KANBARA, Takayoshi[1]; HOSOKAWA, Tomoko[1]; FUJIWARA, Akihiko[3]; SHINOHARA, Hisanori[4]; ITO, Yasuhiro[4]
([1]Okayama Univ.; [2]IMS and Okayama Univ.; [3]JAIST; [4]Nagoya Univ.)

[submitted]

A new type of carbon cluster field effect transistor (FET) was fabricated with thin film of C_{84}, and *n*-channel normally-on depletion-type FET characteristics were found in this FET device. The C_{84} FET device exhibited the highest mobility, μ, of 1.3×10^{-3} $cm^2V^{-1}s^{-1}$ among normally-on carbon cluster FETs. The carrier transport of this FET device suggested a thermally-activated hopping transport. Carrier type (*n*-channel) and transport mechanism (hopping) reflect the electronic properties of the C_{84} molecule. This is the first report of the FET with higher-fullerene thin-film.

VIII-Z-12 Structural and Electronic Characterizations of Two Ce@C_{82} Isomers

RIKIISHI, Yoshie[1]; HOSOKAWA, Tomoko[1]; SHIBATA, Kana[1]; HARUYAMA, Yusuke[1]; TAKABAYASHI, Yasuhiro[1]; KUBOZONO, Yoshihiro[2]
([1]Okayama Univ.; [2]IMS and Okayama Univ.)

[submitted]

X-ray diffraction patterns for the Ce@C_{82} isomers I and II, which refer to major and minor isomers, respectively, are studied in a wide temperature region. The diffraction patterns observed at 295 K can be indexed based on a simple cubic (sc) structures with the lattice constants, *a*'s of 15.78(1) Å for the isomer I and 15.74(4) Å for the isomer II. Rietveld analyses are achieved for these X-ray diffraction patterns with a space group of $Pa\bar{3}$. Temperature dependence of *a* for the isomer I shows a drastic change around 150 K which implies an existence of structural phase transition. The structural phase transition above 300 K cannot be detected for the Ce@C_{82} isomer I in contrast with the fact that the phase transition at 400 K was previously reported for La@C_{82} isomer I by a differential scanning calorimetry and dielectric constant measurements. Temperature dependence of *a* for the isomer II indicates no structural phase transition from 100 to 300 K. Pressure dependence of *a* for the isomer I exhibits a monotonous decrease with an increase in pressure. This result implies no pressure-induced structural phase transition for the isomer I.

VIII-AA Study of Electronic Structure of Organic Thin film and Organic/Inorganic Interface

Organic semiconductors have gained increasing interest because of their potential use in various optoelectronic devices In order to understand electronic processes at interface in the organic devices, many surface sensitive techniques such as high-resolution ultraviolet photoemission spectroscopy (UPS) have been performed for organic thin films, because origins of the energy position and the bandwidth of ultraviolet photoelectron spectra are keys to understand interface properties, such as the energy level alignment at the interface and molecule-molecule and/or molecule-substrate interaction. The energy-band structure is a fundamental basis for the understanding of electronic and optical properties of solids. The intermolecule band dispersion for the organic thin film is observed using angle-resolved UPS using synchrotron radiation, since the width of band dispersion depends the intermolecular interaction.

VIII-AA-1 Intermolecular Energy-Band Dispersion in PTCDA Multilayers

YAMANE, Hiroyuki[1]: KERA, Satoshi; YOSHIMURA, Daisuke; OKUDAIRA, K. Koji; SEKI, Kazuhiko[2]; UENO, Nobuo[1]
([1]Chiba Univ.; [2]Nagoya Univ.)

[*Phys. Rev. B* **68**, 033102 (4 pages) 2003]

The electronic structure of a well-oriented perylene-3,4,9,10-tetracarboxylic acid-dianhydride multilayer prepared on MoS_2 single crystal surface were studied by angle-resolved ultraviolet photoemission spectroscopy using synchrotron radiation. From the photon energy dependence of normal emission spectra, we observed an intermolecular energy-band dispersion of about 0.2 eV for the highest occupied molecular orbital (HOMO) band of single π character. The observed energy-band dispersion showed a cosine curve, which originates from the intermolecular π-π interaction. Analyses using the tight-binding model gave that the transfer integral of about 0.05 eV for the π-π interaction, the effective mass of HOMO hole $m_h^* = 5.28m_0$, and the hole mobility $\mu_h > 3.8$ cm^2/V s. This is the first observation of the intermolecular energy-band dispersion of a conventional single-component organic semiconductor only with the weak intermolecular van der Waals interaction.

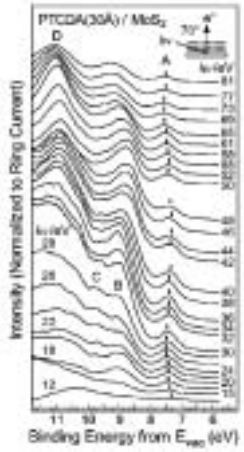

Figure 1. Photon energy ($h\nu$) dependence of SR-ARUPS spectra along the surface normal for the 30-Å-thick PTCDA multilayer (~ 8 ML) prepared on the MoS_2 surface. The binding energy (E_B)scale refers to the vacuum level (E_{vac}).

VIII-AA-2 Very Narrow Photoemission Bandwidth of the Highest Occupied State in a Copper-Phthalocyanine Monolayer

KERA, Satoshi; YAMANE, Hiroyuki[1]; SAKURAGI, Isamu[1]; OKUDAIRA, K. Koji; UENO, Nobuo[1]
([1]Chiba Univ.)

[*Chem. Phys. Lett.* **364**, 93–98 (2002)]

We observed a very narrow bandwidth of the highest occupied molecular orbital (HOMO) state in ultraviolet photoemission spectra (UPS) of copper-phthalocyanine monolayer deposited on graphite. The HOMO band in UPS consists of three components which may originate from the vibrational coupling. The full width at half maximum of each component was found to be ~ 150 meV at 295 K. This HOMO-bandwidth leads to an estimation that the lifetime of the HOMO hole should be at least longer than 2.2 fs, which may be dominated by the electron transfer rate from the substrate to the molecule.

VIII-BB Effects of High Magnetic Field on Chemical and Physical Processes

We have studied the effects of high magnetic field on chemical reaction and physical processes of diamagnetic and paramagnetic materials to unravel the mechanisms of the interaction of matter and magnetic field and to develop unique methods controlling chemical and physical processes and improving chemical and physical properties of functional materials. Currently we are using a vertical superconducting magnet which can generate high magnetic fields (15 T, 1500 T^2/m) in a 40 ϕ bore tube. Magnetic levitation of a water droplet and others is capable using the magnet. It is shown that many chemical reactions and physical processes are significantly affected by the magnetic field. For example, we have succeeded, for the first time, to induce 3D-morphological chirality in zinc silicate membrane tube using a high magnetic field. The results are interpreted in terms of the Lorentz force on ions thermally moving in an aqueous solution. In NaCl:Eu crystals, dislocation mobility is affected by a magnetic field.

VIII-BB-1 3D-Morphological Chirality Induction in Zinc Silicate Membrane Tube Using a Magnetic Field

UECHI, Ichiro[1]; KATSUKI, Akio[2], DUNIN-BARKOVSKIY, Lev R.; TANIMOTO, Yoshifumi
([1]IMS and Hiroshima Univ.; [2]Shinshu Univ.)

[*J. Phys. Chem.* in press]

We report *three-dimensional morphological* chirality induction using a vertical magnetic field. Right-handed *circular* helix of zinc silicate membrane tube was *selectively* induced by application of a magnetic field (5–15 T), whereas the tube grew straightly upward at zero field as shown in Figure 1. Left-handed circular helix was also selectively obtained by changing experimental condition. *Square* and *triangular* helixes were also prepared. The results are interpreted in terms of the boundary-assisted magnetohydrodynamics mechanism in which cyclotron motion of ions in solution results in one-way convection of the solution near the boundary.

Figure 1. Magnetic field effects on the growth of zinc silicate membrane. (a) 0 T, (b) 6 T, (c) 13.5 T.

VIII-BB-2 Effects of a High Magnetic Field on the Growth of 3-Dimensional Silver Dendrites

KATSUKI, Akio[1]; UECHI, Ichiro[2]; TANIMOTO, Yoshifumi
([1]Shinshu Univ.; [2]IMS and Hiroshima Univ.)

[*Bull. Chem. Soc. Jpn.* in press]

A liquid/solid redox reaction between silver ion and copper metal was investigated under a *vertical* and *inhomogeneous* high magnetic field (maximum field strength: 15 T). 3-Dimensional silver dendrites produced *via* the reaction were affected drastically by the magnetic field. Black and round dendrites were obtained in the magnetic field, whereas metallic silver crystals were grown under the gray dendrites at zero field. The yields of silver dendrite and copper ion increased significantly in the magnetic fields. The results are interpreted in terms of magnetic convection of the solution which is induced by the magnetic force on paramagnetic copper ions generated in the reaction as well as the Lorentz force on ions.

VIII-BB-3 Magnetic Field Effects on TiO_2 Photocatalytic Reaction

KAMOCHI, Masataka[1]; FUJIWARA, Yoshihisa[1]; TANIMOTO, Yoshifumi
([1]Hiroshima Univ.)

We attempted to examine whether a magnetic field could affect photo-catalytic reaction of titanium oxide, as little was known about the magnetic field effect (MFE) on catalytic reaction. The reaction studied here is as follows,

$$CH_3OH + H_2O + h\nu + TiO_2/Pt \rightarrow 3H_2\uparrow + CO_2\uparrow$$

A methanol-water (1:1) solution containing titanium oxide powder and chloroplatinic (IV) acid hexahydrate was irradiated with light from a xenon lamp in the absence and presence of a magnetic field and the volume of the photo-generated gas was determined. The yield of the gas decreased gradually with increasing a magnetic field from zero to 4 T (*ca.* –10% at 4 T). Similar MFE was observed on the photocurrent of the photo-galvanic cell, $TiO_2(s)|NaOH(aq)||H_2SO_4(aq)|Pt(s)$.

The present MFE is tentatively explained in terms of

a radical pair model (Δg mechanism). Upon photo-excitation of TiO_2, excited singlet TiO_2, $^1TiO_2$*, is generated. While $^1TiO_2$* undergoes intersystem crossing (ISC) to $^3TiO_2$*, singlet electron-hole pair is generated from $^1TiO_2$*. The free electron and hole will be formed by the dissociation of the singlet pair. In a magnetic field, the singlet-to-triplet ISC in the pair is accelerated due to the difference in *g*-values of electron and hole, leading the depression in the yield of free electron and hole by which the succeeding redox reaction is initiated.

VIII-BB-4 On the Movement of Paramagnetic Ions in an Inhomogeneous Magnetic Field

FUJIWARA, Masao; CHIE, Kenjiro[1]; SAWAI, Jun[1]; SHIMIZU, Daisuke[1] ; TANIMOTO, Yoshifumi
([1]Hiroshima Uinv.)

[*J. Phys. Chem.* submitted]

The movement of transition metal ions was observed in an inhomogeneous magnetic field. The solution containing Cr^{3+}, Mn^{2+}, Co^{2+}, Ni^{2+}, and Cu^{2+} ions was spotted on a silica gel support, and exposed to magnetic fields up to 410 kOe^2cm^{-1}. The distribution of the metal ions was measured, and the frictional coefficient of the movement was analyzed in relation to the susceptibility and concentration of the metal ions as well as to the size of the silica gel particles. When the concentration is higher, the metal ions move to a larger the distance. It is shown that a large group composed of the metal ions and water molecules moves in a magnetic field.

VIII-BB-5 Magnetic Separation of Metal Ions

CHIE, Kenjiro[1]; FUJIWARA, Masao; FUJIWARA, Yoshihisa[1]; TANIMOTO, Yoshifumi
([1]Hiroshima Univ.)

[*J. Phys. Chem.* in press]

The magnetic separation was investigated for Co^{2+}(9500 × 10^{-6} cm^3mol^{-1}) and Fe^{3+} (14600 × 10^{-6} cm^3mol^{-1}) ions and for Cr^{3+} (6200 × 10^{-6} cm^3mol^{-1}) and Al^{3+} (–2 × 10^{-6} cm^3mol^{-1}) ions. The metal ion solutions were spotted on a silica gel support and exposed to a magnetic field of 410 kOe^2cm^{-1} intensity × gradient. The Co^{2+} ions move to a larger distance toward the maximum field than the Fe^{3+} ions. The result is explained by the fact that the Fe^{2+} ions are adsorbed more strongly on the silica gel support than the Co^{2+} ions. The Cr^{3+} ions move farther toward the field center than the Al^{3+} ions. This occurs because the Cr^{3+} ions are attracted more strongly by the magnetic force than the Al^{3+} ions. It is demonstrated that the separation makes effective use of the adsorption activities as well as the magnetic susceptibilities.

VIII-BB-6 Influence of Magnetic Field up to 15 T on Luminescence of NaCl:Eu Crystals

BASKAKOV, A. A.[1]; DUNIN-BARKOVSKIY, Lev R.[2]; MORGUNOV, Roman B.[2]; TANIMOTO, Yoshifumi
([1]ISSP, Chernogolovka; [2]IMS and ISSP, Chernogolovka)

Variations of Eu^{2+} luminescent spectra during Eu aggregation in NaCl crystal lattice has been found. These variations caused by extremely high sensitivity of electronic levels splitting to intracrystalline electrical field and Eu^{2+} environment continuously changing during aggregation process. Influence of magnetic field on luminescent excitation spectra in nonequilibrium quenched crystals during the aggregation acted was found (Figure 1). Redistribution of luminescent bands intensity in the excitation spectra gradually increases with the sample exposure in magnetic field (Figure 1). It is unreasonable to suppose that Eu^{2+} ions being paramagnetic can take part in a spin-dependent solid state reaction controlled by magnetic field.

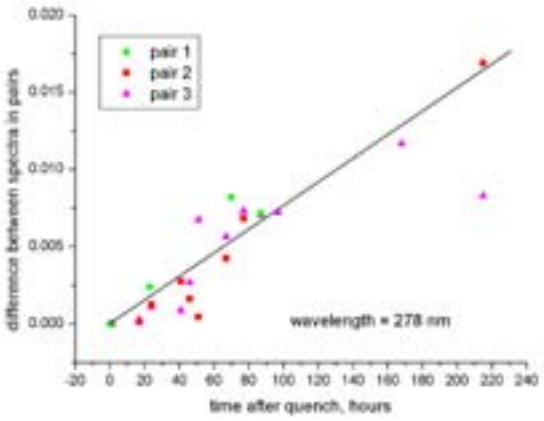

Figure 1. Dependencies of difference between luminescence intensity in reference sample and identical crystal stored in magnetic field after quenching on storage duration for 3 pairs of the identical NaCl:Eu crystals.

VIII-BB-7 Magnetic Field Effect on Dislocation Mobility in NaCl:Eu Crystals

BASKAKOV, A. A.[1]; DUNIN-BARKOVSKIY, Lev R.[2]; MORGUNOV, Roman B.[2]; TANIMOTO, Yoshifumi
([1]ISSP, Chernogolovka; [2]IMS and ISSIP, Chernogolovka)

Recent investigation shown that mobility of dislocations (elementary carriers of plastic deformation) could be considered as an electron spin-dependent process. Magnetic field and its influence on dislocation displacements can serve as a facilities to distinguish spin-dependent part of dislocation interaction with the obstacles. All experiments in this area were carried out early in magnetic fields up to 2 T or in pulsed fields. In this work comparatively strong static magnetic field 15 T was used. It is important because identification of concrete mechanism of spin state mixing in magnetic field as a rule based on correct field dependencies of the magnetic effects.

Displacements of individual dislocation and movement of dislocation in slip bands after exposure of

diamagnetic NaCl:Eu crystals in magnetic field with an induction 15 T were found (Figure 1). Since there was no an external loading of crystals during experiments, the internal stress were the main reason of dislocation displacements. Magnetic field initiates unpinning of dislocations from local obstacles that are Eu aggregates. After magnetic field was switched off increased mobility of the dislocations takes place during 1–2 days. Obtained results open a new possibilities to reliable comparison of theory predictions with the experimental data.

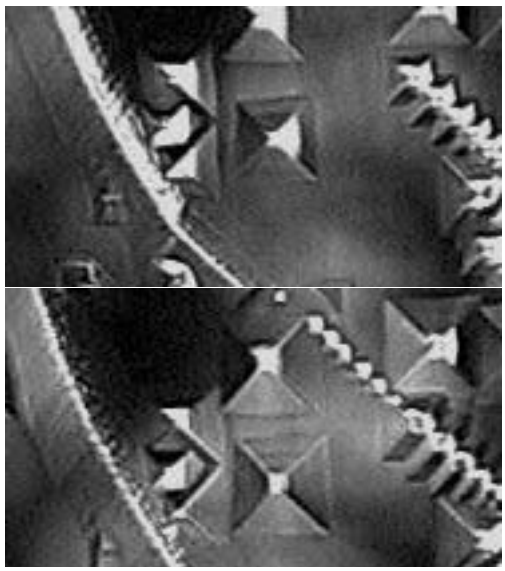

Figure 1. Surface of NaCl crystal a) before, b) after exposure in MF. Big pyramidal pits are initial position of dislocation lines entering on the surface. Small pits are new dislocation line positions after displacement.

VIII-BB-8 Imprinting Magnetic Memory Cells in Molecular Based $NiL_2(C_2H_5OH)_2$ Heterospin Crystals

BASKAKOV, A. A.[1]; FOKIN, S. V.[2]; GUDOSHNIKOV, S. A.[3]; MORGUNOV, Roman B.[4]; OSSIPYAN, YU. A.[1]; OVCHARENKO, V. I.[2]; SAGDEEV, R. Z.[2]; SKOMARVSKII, V. S.[3]; TANIMOTO, Yoshifumi
([1]ISSP, Chernogolovka; [2]Intl. Tomography Cent., Novosibirsk; [3]Inst. Terrestrial Magnetism, Troitsk; [4]IMS and ISSP, Chernogolovka)

Magnetic studies of molecular based crystals have stirred great interest in the magnetic properties of structural defects induced by plastic deformation. In our experiments local deformation of molecular based magnet was carried out by diamond indentor. Local magnetic field around indentation pit was measured by scanning SQUID magnetometer. It has been found that local deformation causes ferromagnetic exchange interaction in $NiL_2(C_2H_5OH)_2$ heterospin single crystals at unusually high temperatures (≥ 77 K). These magnetization temperatures are much higher than the temperature observed for the same, but undeformed crystals (~ 5 K). Ferro- and antiferromagnetic ordering around dislocation cores arise from lattice distortions and changes in distances between the magnetic atoms. Near structural defects high pressure will strongly affect exchange interactions in many spin paramagnetic crystals. Thus, in spite of usual aspiration for perfect crystals grows our experiment shown that disordering can give fruitful results. Local plastic deformation should be considered as a method of control over the magnetic properties of molecular based crystals and as a technique for improving their magnetic characteristics. It offers a nice possibility to imprint the magnetic structure and to distribute magnetic memory cells on the surface premeditatedly. Nanoindentation technologies will probably allow the imprinting of separate magnetic cells ~ 1–10 nm in size.

VIII-BB-9 Localization of Conduction-Band Electrons in β”-(BEDT-TTF)$_4NH_4[Cr(C_2O_4)_3]$·DMF Single Crystals

MORGUNOV, Roman B.[1]; BASKAKOV, A. A.[2]; DUNIN-BARKOVSKIY, Lev R.[1]; KHASANOV, S. S.[1]; SHIBAEVA, R. P.[2]; PROKHOROVA, T. G.[3]; YAGUBSKIY, E. B.[3]; KATO, Tatsuhisa; TANIMOTO, Yoshifumi
([1]IMS and ISSP, Chernogolovka; [2]ISSP, Chernogolovka; [3]Inst. Problems Chem. Phys., Chernogolovka)

Temperature dependence of EPR spectrum of β”-(BEDT-TTF)$_4NH_4[Cr(C_2O_4)_3]$·DMF single crystals, which consists of two separate lines characterizing magnetic features of BEDT-TTF and Cr^{3+} ions, was studied within the range 1.5–300 K. It was found that reconstruction of the EPR spectrum occurs under decrease of the temperature down to $T \approx 20$ K. The reconstruction consists in change of Lorentzian shape of the BEDT-TTF line to Gaussian one and in decrease of the effective magnetic moment of Cr^{3+} ions. Analysis of temperature and orientation dependencies of parameters of the EPR spectra allows one to suppose that localization of conduction electrons within regions with dimensions close to the size of individual BEDT-TTF molecules occurs at $T \approx 20$ K. Exchange interactions between Cr^{3+} ions change towards antiferromagnetic spin correlations as well.

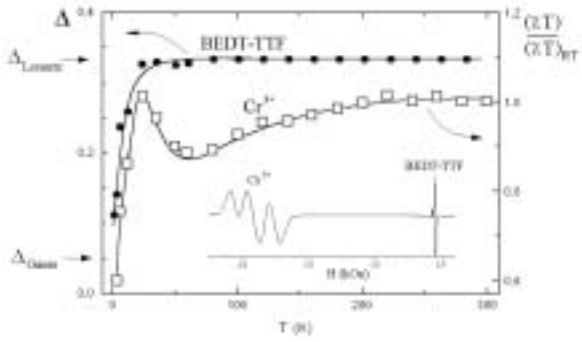

Figure 1. Dependencies of χT and line-shape parameter Δ (Δ = 0.05 for pure Lorenz line and Δ = 0.33 for pure Gauss one) on temperature *T*. ESR spectrum of the salt at room temperature is shown on the insert.

VIII-CC Theoretical and Computational Study on Gas Phase Reactions and Chromic Molecules

1. Quantum chemical calculations are used to produce potential energy surface (PES) to do reaction dynamics simulations. We develop the methodology to generate PES efficiently and automatically using quantum chemical calculation results. The method does not need any derivative information in quantum chemical calculations.
2. Another interest of our group is theoretical explanation and prediction of structural and spectral changes of photochromic and electrochromic substances.
3. We also search a reasonable pathway to form H_2 from H atoms *via* PAH related catalysts to solve why H_2 is abundant in interstellar space.

VIII-CC-1 Theoretical Study on Photoinduced Color Change and Charge Transfer of Methylviologen

ISHIDA, Toshimasa; MURAKAMI, Makoto[1]; WATANABE, Go[1]; YOSHIKAWA, Hirofumi[2]; NISHIKIORI, Shin-ichi[2]
([1]Shizuoka Univ.; [2]Univ. Tokyo)

[*Internet Electronic J. Mol. Design* **2**, 14–23 (2003)]

Methylviologen dication is easily reduced to a monocation radical, and turned to be blue, forming a charge-transfer complex with a donor molecule. Yoshikawa *et al*. recently reported photo-induced reduction and charge transfer complexes in poly-cyano–polycadmate host clathrates. We study this reduction using quantum chemical calculations. The energy changes with the torsion angle of the two cations and the spectral change, solvent effect and the charge transfer between the dication and other guest molecules in the clathrates are investigated. The Hartree-Fock, DFT, CI singles, time dependent DFT calculations are carried out for the ground state and excited states of the two cations. Solvation effect is treated with the polarizable continuum model, and the charge transfer in the clathrates is modeled based on crystal structures determined experimentally. The optimized geometry of the monocation radical was found to be planar while that of the dication is twisted. These results are consistent with recent calculations for related compounds. The color change upon the photoreduction was reproduced by the calculation. The solvent effect of acetonitrile was found to be small. Charge transfer absorption was reproduced for the mesitylene–methylviologen dication complex in the clathrate host using a small model. The geometry modification and the color change were reproduced satisfactorily. The TDDFTscheme reproduces the observed spectra better than the CIS scheme, but the latter scheme is still valuable to evaluate qualitative feature of spectra.

VIII-CC-2 Crystal Structure and Spectroscopic Properties of the CT Complex of Methyl Viologen Dication and *o*-Dimethoxybenzene Included in a Polycyano-Polycadmate Host, and Theoretical Study on Its Red Shifted CT Absorption

YOSHIKAWA, Hirofumi[1]; NISHIKIORI, Shin-ichi[1]; ISHIDA, Toshimasa
([1]Univ. Tokyo)

[*J. Phys. Chem. B* **107**, 9261–9267 (2003)]

Using the polycyano-polycadmate host that is a negative charged Cd cyanide complex with a framework structure built with Cd^{2+} ions and bridging cyanide ligands, we synthesized a clathrate including methyl viologen dication (MV^{2+}) and *o*-dimethoxybenzene (ODMB) as guests. The color of the clathrate was red and its origin was considered to be charge transfer (CT) interaction of a CT complex formed with MV^{2+} as an acceptor and ODMB as a donor in the host. The wavelength at the CT absorption maximum was largely red shifted compared with that of the CT complex in an acetonitrile solution. The single crystal X-ray diffraction analysis revealed a π-π stacking structure of the CT complex and a 1D arrangement of the CT complexes in a channel-like cavity of the framework host. In the array of the CT complexes, MV^{2+} ions are adjacent to each other and their separation is short. The direction of the transition moment of the CT absorption determined from the structural information and the spectrum measured on a crystalline sample agreed with that derived from *ab initio* calculations at the CIS/6-31+G* level. Our calculations also showed that the red shift of the CT absorption is mainly due to electrostatic effects between the CT complexes, not due to the shortening of the distance between MV^{2+} and ODMB, which is generally believed to be the reason. The negative charged host stabilizes the ground state of the CT complex, but the electrostatic interaction between the CT complexes heightens the ground state and lowers the excited state. In this clathrate, due to the CT complex array with the short separation the effect from the guests overcomes that from the host and the red shift appears.

VIII-CC-3 A Local Interpolation Scheme Using No Derivatives in Potential Sampling: Application to $O(^1D) + H_2$ System

ISHIDA, Toshimasa; SCHATZ, George C.[1]
([1]Northwestern Univ.)

[*J. Comput. Chem.* **24**, 1077–1086 (2003)]

We recently proposed a local interpolation scheme, in which interpolant moving least squares (IMLS) and Shepard interpolation are employed to describe potential

energy surfaces. This IMLS/Shepard scheme is applicable to do potential interpolation with quantum chemical results for which analytical derivatives are not available. In this study, we apply the scheme to the highly exothermic $O(^1D) + H_2 \rightarrow H + OH$ reaction and compare it with results based on Shepard interpolation using second order Taylor expansions. An analytical surface is used to define the potential function so that errors in the interpolation function may accurately be determined. We found that the present scheme reproduces the correct reactive cross sections more accurately than the Shepard scheme, and with rms errors for energy and gradients that are significantly smaller than those from Shepard interpolation. This occurs even though the present scheme does not utilize derivative and hessian information whereas the Shepard interpolation does. The Bayesian approach proposed by Bettens and Collins does not improve the IMLS/Shepard results significantly although it does the Shepard-only approach. The accuracy in the IMLS/Shepard scheme is surprising, but can be explained by the more global nature of the interpolation.

VIII-CC-4 Possible Molecular Hydrogen Formation Mediated by the Radical Cations of Anthracene and Pyrene

HIRAMA, Mutsumi[1]; ISHIDA, Toshimasa; AIHARA, Jun-ichi[1]
([1]Shizuoka Univ.)

[*J. Comput. Chem.* **24**, 1378–1382 (2003)]

Hydrogen molecules cannot be formed readily by the association of gaseous hydrogen atoms. Possible H_2 formation mediated by the radical cations of typical polycyclic aromatic hydrocarbons (PAHs), anthracene and pyrene, was studied at the B3LYP/6-31G** level of theory. We presumed that H_2 is formed by way of two elementary reactions, the addition of an H atom to a PAH molecular cation and the H abstraction from the resulting monohydro-PAH cation (*i.e.*, arenium ion) by a second H atom to yield H_2. The first reaction takes place without any activation energy. The second reaction is also predicted to proceed along almost barrierless pathways although it is far from being a typical ion-molecule reaction. There is a possibility that these reactions might constitute one of the mechanisms for H_2 formation in extremely cold interstellar space. Deuterium enrichment in PAH cations is possibly accompanied by such H_2 formation since deuteration lowers the energies of polyatomic PAH cations appreciably.

VIII-CC-5 Molecular Hydrogen Formation Mediated by a Naphthalene Radical Cation

TOKOSUMI, Takaaki[1]; HIRAMA, Mutsumi[1]; TERADA, Yoshihiro[1]; HAGIWARA, Noriko[1]; ISHIDA, Toshimasa; AIHARA, Jun-ichi[1]
([1]Shizuoka Univ.)

[*Phys. Chem. Chem. Phys.* submitted]

Hydrogen molecules cannot be formed readily by the association of gaseous hydrogen atoms. Bauschlicher and we independently proposed a possible molecular hydrogen formation mediated by polycyclic aromatic hydrocarbon (PAH) radical cations in space. We studied such a reaction process at the B3LYP/6-31G** level of theory and for the first time succeeded in determining the entire reaction pathway for the H_2 formation mediated by the naphthalene radical cation. We presumed that H_2 is formed by way of two elementary reactions, the addition of an H atom to a naphthalene cation and the H abstraction from the resulting naphthalenium ion by a second H atom to yield H_2. The first reaction takes place without any activation energy. The second reaction is predicted to proceed *via* a van der Waals complex but with little activation energy. These reactions are supposed to enhance the deuteration of the naphthalene cation. Neutral naphthalene also mediates the H_2 formation but needs some activation energy.

VIII-CC-6 Possible Molecular Hydrogen Formation Mediated by the Inner Carbon Atoms of PAH Radical Cations

HIRAMA, Mutsumi[1]; ISHIDA, Toshimasa; AIHARA, Jun-ichi[1]
([1]Shizuoka Univ.)

[in preparation]

Molecular hydrogen in space is believed to form from atomic hydrogen. During the past few years, we have been performing density functional theory (DFT) calculations to explore the possibility of H_2 formation mediated by the radical cations of gaseous polycyclic aromatic hydrocarbons (PAHs). As a continuation of this study, we explored the catalytic ability of inner carbon atoms of some typical PAH cations at the B3LYP/6-31G** level of theory. We presumed as before that H_2 is formed by way of two elementary reactions, the addition of an H atom to a PAH cation and the H abstraction from the resulting arenium ion by another H atom to yield H_2. We found that both reactions proceed without any activation energy. It follows that almost all carbon atoms of a PAH cation give sites for moelcular hydrogen formation. Since there are large compact PAHs abundantly in space, the H_2 formation at the inner carbon atoms of such PAH cations can never be overlooked. Even if inner carbon atoms might be less reactive than peripheral ones, there are many inner carbon atoms in large compact PAH cations.

VIII-DD Macromolecular Self-Assembly Opens the Way for Development of Novel Materials that Have Characteristics of Cellular Systems

Self-assembly is a principle to integrate molecular devices into a cellular supramolecular system. Exchangeability of the components, characteristic of assembled structures, allows the system to be repairable, reusable and modifiable on demand, and enables metabolism, adaptation, and evolution of the system. This insight may open new perspective for artificial photoelectronic apparatuses at the nano scale. Development and integration of molecular devices have been focuses for downsizing and energy-saving in the field of photoelectronics. For global, sustainable development, in our opinion, the future materials should also be "entropy-saving" (reusable, repairable, and bio-degradable) that has not been considered to date. We thus aimed at development of an artificial photosynthetic system that allows on-demand reuse (Figure 1); for their basis, we also study on molecular mechanisms of photosynthesis. Our study should serve a new design concept for nano- and molecular-scale intelligent materials (see also Special Research Project (c)).

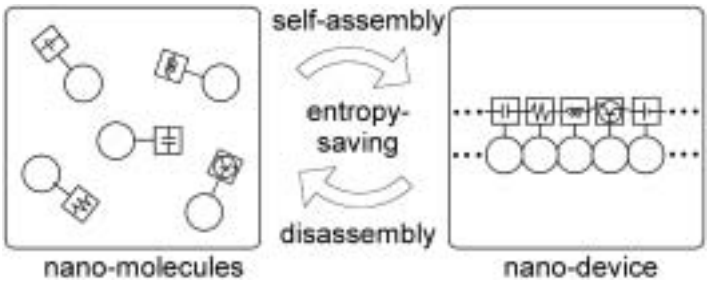

Figure 1. A concept of the "entropy-saving" nano-devices. The device does not function until on-demand self-assembly of nano functional blocks, and the device can easily be decomposed into the reusable components on demand.

VIII-DD-1 Engineering of Tobacco Mosaic Virus

OBA, Toru; TAKATOYA, Haruki[1]; MINABE, Masahiro[1]
([1]Utsunomiya Univ.)

Green photosynthetic bacteria possess rod-shaped nano-elements (4 ~ 5 nmϕ × 200 ~ 300 nm) as cores of light-harvesting antenna function. The rod-element is thought to be a self-assembled chlorophylls whose details remain yet unclear. Such a supramolecule may be useful as unique devices for future photoelectronics and biotechnology, but (1) it is impossible to obtain intact rod-elements from the cell and (2) it is quite difficult to build artificial tubule supramolecules by self-assembly of chlorophylls. We aimed at construction of nano-tubule of self-assembled chlorophylls by using tobacco mosaic virus (TMV) as a template. TMV possesses a tubule structure with an outer diameter of 15 nm, inner diameter of 4 nm, and length of 300 nm: the size of the channel matches that of the chlorosomal rod-element. We synthesized novel hydrophilic chlorophyll derivatives, and examined their affinities for the inner surface of TMV and their self-assemblies in the channel.

VIII-DD-2 Synthesis and Properties of Novel Biotin Derivatives

OBA, Toru; TOBITA, Hiromi[1]; MINABE, Masahiro[1]
([1]Utsunomiya Univ.)

Arrangement and connection of functional molecules in desired sequences and shapes are basic techniques for future fabrication of elaborate molecular systems including nano-devices and nano-computers. We aimed at development of a new method to arrange functional molecules sequentially in a desired order by utilizing specific interaction between avidin and biotin. Avidin is a 6.8 kDa protein (*ca.* 5 × 5 × 6 nm in size) that can bind four biotin molecules. The topology of the biotin binding sites is appropriate to link avidin molecules linearly when using a linear molecule that possesses two biotin moieties at both ends. Syntheses of novel bitoin derivatives and examination of their abilities to control the assembly of avidin molecules are now under way.

VIII-DD-3 Physicochemical Studies on the Molecular Mechanism of Photosynthesis

OBA, Toru; TAMIAKI, Hitoshi[1]
([1]Ritsumeikan Univ.)

[*Photosynth. Res.* **74**, 1–10 (2002)]

Since chlorophylls (Chls) and bacteriochlorophylls (BChls) are highly asymmetric molecules, an external ligand can coordinate to the central Mg atom of (B)Chls either from the chlorin macrocycle side where the C13^2-methoxycarbonyl moiety protrudes (denoting as the "back" side) or from the other side (the "face" side, Figure 2). We found that the "back" side is favored for the ligand coordination, by survey of the highly resolved crystal structures of photosynthetic proteins and by theoretical calculations of model molecules. The calculations reveal that stability of the (B)Chl-ligand

complex is sensitive to distortion of the macrocycle, and the distortion is affected by steric repulsion between particular peripheral substituents as well as flexibility of the macrocycle. We note that not only the static pigment-protein (pigment-pigment) interactions but also dynamics of the pigment-protein (pigment-pigment) assembly should be clarified for better understanding of the role of the planar chirality of (B)Chls *in vivo*.

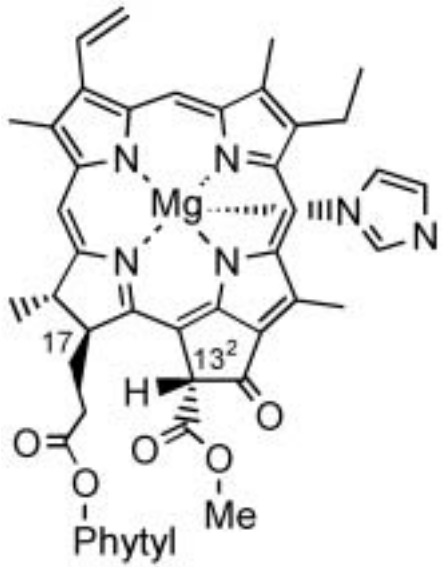

Figure 1. Molecular structure of the "back" type chlorophyll *a*-imidazole complex.

Equipment Development Center

VIII-EE Development of "Special Machine"

The technical staff of the Equipment Development Center is partly engaged in planning, researching, designing and constructing "Special machine." This machine, is a high-tech experimental instrument, with emphasis on newtechnical idea and co-operative work with members inside and outside the Institute including those in industries.

VIII-EE-1 Construction of the Evaluation Endstation Dedicated for Transmission Gratings

HATSUI, Takaki; KOSUGI, Nobuhiro; KONDOH, Takuhiko[1]; MATSUSHITA, Kouji; YANO, Takayuki; UTCHIYAMA, Kouichi; SUZUI, Mitsukazu
([1]Nagoya Univ.)

A novel endstation dedicated for the evaluation of free-standing transmission grating have be en constructed at BL4B of the UVSOR facility in the course of the development project of soft x-ray emission spectrometer in collaboration with the department of vacuum UV photoscience. The transmission grating are planned to be used in a novel soft x-ray emission spectrometer, which covers 100–1000 eV region. The endstation is capable to measure the absolute diffraction efficiency as well as energy resolution limited by the imperfect grating structure. Figure 1 shows the schematic overview of the endstation, which consists of a chamber for target grating (a), a Si diode detector for the diffraction efficiency measurement (b), and a gas cell for the measurement of the energy resolution of the grating (c). The grating chamber is capable to move the grating along 5 axes by using a linear feedthrough and three micrometers. The position of the gas cell is controlled by a manupilator, and monitored by a laser interferrometer so that x-ray absorption spectra of gaseous sample can be measured by scanning the gas cell. The high precision slit located upper stream to the gas cell have two blades. The blades are manufactured by grinding using Electrolytic in-process dressing (ELID) method, which was introduced to the equipment development center through the collaboration with Nagoya university. First results have been obtained for a test grating chip in March 2003.

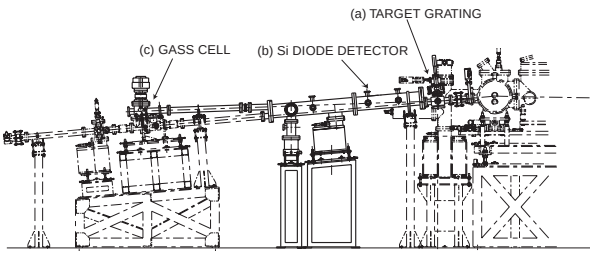

Figure 1. Schematic overview of the endstation at BL4B.

Ultraviolet Synchrotron Orbital Radiation Facility

VIII-FF Development of the UVSOR Light Source

VIII-FF-1 UVSOR Upgrade Project

KATOH, Masahiro; HOSAKA, Masahito; MOCHIHASHI, Akira; YAMAZAKI, Jun-ichiro; HAYASHI, Kenji; HORI, Yoichiro[1]; HONDA, Toru[1]; HAGA, Kaiichi[1]; TAKASHIMA, Yoshifumi[2]; KOSEKI, Tadashi[3]; KODA, Shigeru[4]; KITAMURA, Hideo[5]; HARA, Toru[5]; TANAKA, Takashi[5]
([1]KEK-PF; [2]Nagoya Univ.; [3]RIKEN; [4]Saga Sync. L. S.; [5]RIKEN/SPring-8)

UVSOR was successfully converted to UVSOR-II, which has eight straight sections and small emittance of 27 nm-rad. The magnetic lattice was modified without changing the circumference of 53.2 m. All the magnets and their beam ducts except for the bending magnets were replaced. An undulator and a super-conducting wiggler were replaced with two new in-vacuum undulators. Some parts of the injector were replaced and upgraded. Some beam-lines were reconstructed. All the reconstruction works were completed within three months, from April to June 2003. In July, UVSOR-II was successfully commissioned. Some preliminary measurements on the beam parameters suggested that the design goal of the emittance, 27 nm-rad, was likely achieved. Vacuum conditioning with beams are in progress. Users experiments will start in September.

VIII-FF-2 UVSOR Free Electron Laser

HOSAKA, Masahito; KATOH, Masahiro; MOCHIHASHI, Akira; YAMAZAKI, Jun-ichiro; HAYASHI, Kenji; TAKASHIMA, Yoshifumi[1]; HAMA, Hiroyuki[2]
([1]Nagoya Univ.; [2]Tohoku Univ.)

Q-switching operation of the storage ring FEL provides high peak power and is therefore very attractive to application experiments. On the UVSOR, the Q-switching is performed by modulation of RF frequency. In the operation, an excitation of a coherent synchrotron oscillation of electron beam is observed. However, observed damping of the oscillation is faster than one due to synchrotron radiation by factor 100 and, therefore the influence on the FEL lasing is very small. Detailed analysis reveals that the phenomenon is explained with the Robinson damping.

VIII-FF-3 Ion Trapping at UVSOR

MOCHIHASHI, Akira; KATOH, Masahiro; HAYASHI, Kenji; HOSAKA, Masahito; TAKASHIMA, Yoshifumi[1]; YAMAZAKI, Jun-ichiro
([1]Nagoya Univ.)

A vertical tune shift depending on a beam current in multi-bunch condition was observed in the UVSOR electron storage ring. The vertical tune increased as decrease in the beam current, and the slope of the tune shift depended on the condition of the vacuum in the ring. Such change in the vertical tune was explained by change in stability condition of trapped ions on the beam current. The experimental results were consistent with the results from analytic and tracking calculations.

VIII-FF-4 Improvements of the Vacuum System for the UVSOR II

HORI, Yoichiro; YAMAZAKI, Jun-ichiro; KATOH, Masahiro; HAYASHI, Kenji; HOSAKA, Masahito; MOCHIHASHI, Akira; HAGA, Kaiichi[1]
([1]KEK-PF)

In the upgrading to the UVSOR II, all straight chambers and three bend chambers except some elements such as RF cavities and insertion devices should be replaced to new ones. Those were designed and fabricated considering to increase the pumping speed as much as possible in the bend section and the just downstream. The reconstruction work of the ring was started in April 2003. New beam position monitors were additionally equipped for the reinforcement of the focusing magnets in the UVSOR II. After the installation of all chambers, the ring was re-evacuated and baked. Beam injection to the ring was started in the middle of July. The following vacuum conditioning so-called beam scrubbing has been satisfactorily advanced for the user run scheduled to resume in September.

VIII-FF-5 A New Auger Electron Spectroscopy in Coincidence with Photoelectrons

ITO, Kenji; SHIGEMASA, Eiji

Auger photoelectron coincidence spectroscopy, which involves measuring Auger lines in coincidence with the corresponding photoelectron line, reveals a new trend for doubly charged atomic and molecular ions. The experimental resolution in this spectroscopy can be made as good as the instrument resolution permits; the spectral resolution is limited by a lifetime of the inner-shell hole produced by the photoelectron emission. However, the simultaneous measurements of the two electrons can make the situation such that, due to the energy conservation of the whole process, the instrumental resolution instead of the core-hole lifetime governs the spectral resolution. We are preparing for the experimental investigation that will be carried out at a newly constructed undulator beamline BL3U; a high-resolution and high-efficiency analyzer for threshold photoelectrons with a penetration field, and a high-resolution hemi-spherical analyzer or high-resolution time-of-flight spectrometer for Auger electrons. We have already tested the threshold photoelectron analyzer at UVSOR, and found that the energy resolution of a

few meV can be attained easily.

VIII-GG Researches by the USE of UVSOR

VIII-GG-1 Angle-Resolved Photoion Spectroscopy of NO_2 and SO_2

GEJO, Tatsuo[1]; TAKATA, Yasutaka[2]; HATSUI, Takaki; NAGASONO, Mitsuru; OJI, Hiroshi; KOSUGI, Nobuhiro; SHIGEMASA, Eiji
([1]IMS and Himeji Inst. Tech.; [2]IMS and RIKEN)

[*Chem. Phys.* **289**, 15–29 (2003)]

Based on recent conceptual and technological improvements for soft x-ray monochromators, a varied-line-spacing plane grating monochromator of the Hetrrick type is installed on the bending-magnet beamline BL4B in the UVSOR facility with a second generation VUV ring of the beam energy of 0.75 GeV. The BL4B has enabled us to realize various spectroscopic investigations under high resolution in the energy range of 90 to 800 eV. High-resolution angle-resolved photoion-yield spectra (ARPIS) of NO_2 and SO_2 have been measured in the N and O *K*-shell excitation regions. The fragment-ion yield spectra measured at 0° and 90° relative to the electric vector of the light reveal excitation symmetries of complicated electronic states. The spectral features are interpreted in comparison with other transition systems and quantum chemical calculations show strong or weak Rydberg-valence mixing depending on the excitation site in the molecule.

VIII-GG-2 Atmospheric Lifetime of SF_5CF_3

TAKAHASHI, Kenshi[1]; NAKAYAMA, Tomoki; MATSUMI, Yutaka[1]; SOLOMON, Susan[2]; GEJO, Tatsuo; SHIGEMASA, Eiji; WALLINGTON, Tim J.[3]
([1]Nagoya Univ.; [2]Natl. Oceanic Atmospheric Admin.; [3]FORD Res. Lab.)

[*Geophys. Res. Lett.* **29**, 10.1029/2002GL015356, 7-1–4 (2002)]

The vacuum ultraviolet (VUV) absorption spectrum of SF_5CF_3 was measured over the range 106–200 nm. At 121.6 nm, $\sigma(\text{base } e) = (7.8 \pm 0.6) \times 10^{-18}$ cm^2 molecule^{-1}, in which quoted uncertainty includes two standard deviation from the least-square fit in the Beer-Lambert plot and our estimate of potential systematic errors associated with measurements of the reactant concentrations. The VUV spectrum and literature data for electron attachment and ion-molecule reactions were incorporated into a model of the stratosphere, mesosphere, and lower thermosphere. This information provides better constraints on the atmospheric lifetime and hence on the potential of this highly radiatively-active trace gas to influence the climate system. The atmospheric lifetime of SF_5CF_3 is dominated by dissociative electron attachment and is estimated to be approximately 950 years. Solar proton events could reduce this to a lower limit of 650 years.

VIII-GG-3 Pump /Probe Experiments with FEL and SR Pulses at UVSOR

GEJO, Tatsuo[1]; SHIGEMASA, Eiji; NAKAMURA, Eiken; HOSAKA, Masahito; MOCHIHASHI, Akira; KATOH, Masahiro; YAMAZAKI, Jun-ichiro; HAYASHI, Kenji; TAKASHIMA, Yoshifumi; HAMA, Hiroyuki[2]
([1]IMS and Himeji Inst. Tech.; [2]IMS and Tohoku Univ.)

Storage Ring Free Electron Laser (SRFEL or FEL) has been developed at many synchrotron radiation (SR) facilities all over the world as a powerful light source owing to its high power, high coherence and unique temporal feature. Pump and probe experiments using FEL and SR pulses have been tried to perform for the last decade, since the FEL pulse naturally synchronizes with the SR one. Recently, we have successfully carried out the two-photon double-resonant excitation on Xe atoms, utilizing an SR pulse as a pump and an FEL pulse as a probe light.

In the present work, separate experiments were implemented at two different beamlines of BL3A1 and BL7B at UVSOR. At BL3A1, no monochromator is installed. Therefore, an LiF filter was employed to suppress higher order harmonics of the undulator radiation. The FEL pulses were extracted through the backward mirror of the optical klystron at BL5 and transported to experimental stations through series of multi-layer mirrors. The flight path of FEL, which was adjusted to synchronize timing between the FEL and the SR pulses, was about 30 m. A focusing mirror (f = 10 m) was placed in the center of the flight path to keep the beam size of FEL small throughout the transport. About 69 % of the extracted power was transferred to the experimental station. Fine-tuning of the delay timing was made by using a movable optical delay system (50 cm) at the experimental station. The FEL and SR pulses introduced, coaxially crossed an effusive jet of Xe atoms from a gas nozzle. The singly charged Xe ions produced in the interaction region were detected by means of a conventional channeltron. During the experiment, there were serious background signals due to scattered stray light of SR pulses (typically about 10^5 counts/sec), which made it difficult to detect the real ion signals. In order to overcome such a difficulty, we temporarily employed the Q-switching technique. With use of this technique, much larger peak power of FEL than that in the normal operation is provided, although the duration of lasing becomes relatively short (~ 0.2 msec). However, if events are selected only during this duration, the improvement of signal to noise ratio (S/N)

by a factor of 100 can be achieved.

Figure 1 shows the excitation spectrum near the Xe* $5p^5 5d$ resonance region obtained by setting the FEL wavelength to the maximum of the $5d \rightarrow 4f'$ transition. The background pressure indicated in the figure was kept constant during the measurement. The clear enhancement just below the Xe* $5p^5 5d$ resonance around 117.5 nm is observed in Figure 1, which has not been detected in the previous measurements at a lower pressure. This result strongly suggests that the newly found structure indicated by the arrow is relevant to the formation of Xe clusters, mainly dimers. From the consideration of the excitation energy, it seems to be safe to say that an excited state of Xe_2 exists near the $5p \rightarrow 5d$ transition of the Xe atom, which act as intermediate states in the present experiments.

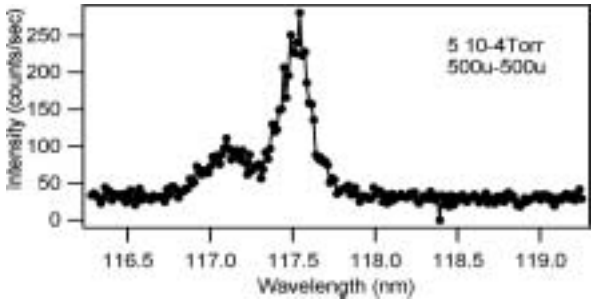

Figure 1. Two-photon ionization signal of Xe as a function of the wavelength of SR.

VIII-GG-4 Photoemission Study of Mixed-Valent Tm-Monochalcogenides: Evidence of Electron-Correlation Effect in Different Tm-Core Levels

NATH, Krishna G.[1]; UFUKTEPE, Yuksel[2]; KIMURA, Shin-ichi; HARUYAMA, Yuichi[3]; KINOSHITA, Toyohiko[4]; MATSUMURA, Takeshi[5]; SUZUKI, Takashi[5]; OGASAWARA, Haruhiko[4]; KOTANI, Akio[4]

([1]JAERI.; [2]Univ. Cukurova, Turkey; [3]Himeji Inst. Tech.; [4]Univ. Tokyo.; [5]Tohoku Univ.)

[*J. Phys. Soc. Jpn.* **72**, 1792–1799 (2003)]

Systematic results of the photoemission spectra for different core levels such as, Tm 4*p*, 5*p* and 3*d* in the mixed valent Tm-monochalcogenides (TmS, TmSe and TmTe) obtained by both experimentally and theoretically are reported. The effects of the electron–electron correlation due to the interaction between core-holes and 4*f*-electrons or the interaction between different configurations are considered to explain the spectral features, depending on the principal (n) and orbital quantum numbers of the core levels. Any sharp peak corresponding to a spin–orbital term is not observed especially from the $n = 4$ states. Instead, the multiplet structures are dominantly observed, and the physical identity of the spin–orbital peaks is totally or partially dissolved into the multiplets. Moreover, the electron-correlation effect is found to be dependent on the valence components (Tm^{2+} and Tm^{3+}). In the case of the Tm 4*p* core level, in which the principal quantum number is identical with the valence 4*f*, the correlation effect is stronger, and the configuration interaction is therefore considered to explain the spectral features. The photoemission spectra for the shallow core level Tm 5*p* also show the effect of electron correlation, but weaker than that for Tm 4*p*. This has been confirmed bythe resonant photoemission spectroscopy taken at Tm 4*d*–4*f* absorption edges. In addition, the feature of Tm 3*d* photoemission spectra is discussed. All the experimental spectra are compared with the calculated ones. It is therefore understood that the electron correlation effect plays an important role on determining the various features in Tm 4*p*, 5*p* and 3*d* photoemission spectra.

VIII-GG-5 Infrared Spectroscopy under Extreme Conditions

KIMURA, Shin-ichi; NISHI, Tatsuhiko[1]; TAKAHASHI, Toshiharu[2]; HIRONO, Toko[3]; IKEMOTO, Yuka[3]; MORIWAKI, Taro[3]; KIMURA, Hiroaki[3]

([1]GUAS; [2]Kyoto Univ.; [3]JASRI/SPring-8)

[*Physica B* **329-333**, 162–1626 (2003)]

We constructed a magneto-optical microspectroscopy apparatus in the infrared region using a synchrotron radiation, SPring-8. In the apparatus, an infrared microscope with the spatial resolution of 11 mm is combined with low temperatures of 3.5 K and high magnetic fields of 14 T. The purpose is to investigate the electronic structure under extreme conditions of tiny materials such as organic conductors and of small region and the spatial distribution of electronic structures. After the installation of high pressure cells, optical measurements under multiple-extreme conditions is available.

VIII-GG-6 Collapse of Kondo Lattice in $Ce_{1-x}La_xPd_3$ (x = 0, 0.03)

KIMURA, Shin-ichi; IWATA, Hideki[1]; KANAI, Kaname[2]; SHIN, Sik[2]; SCHMERBER, G.[3]; KAPPLER, J. P.[3]; PARLEBAS, J. C.[3]

([1]Kobe Univ.; [2]Univ. Tokyo; [3]Univ. Luis Pasteur, France)

[*Acta Physica Polonica B* **34**, 975–978 (2003)]

The change of the electronic structure as well as the hybridization between the localized 4*f* state and the conduction band (cf hybridization) of $Ce_{1-x}La_xPd_3$ (x = 0, 0.03) due to the La-substitution has been studied by the optical conductivity spectra in the infrared region. The width of the optical transition of Pd $4d \rightarrow$ Ce $4f$ states that was mainly observed in the energy region shrinks by the La-substitution. This means that the cf hybridization is strongly suppressed by the absence of the periodicity of the Ce-ion.

VIII-GG-7 Optical Reflectivity of the Clathrate Compound Ba_6Ge_{25}

SICHELSCHMIDT, Jourg[1]; VOEVODIN,

Vladimir[1]; PASCHEN, Silke[1]; CARRILLO-CABRERA, W.[1]; GRIN, Yu.[1]; STEGLICH, Franck[1]; KIMURA, Shin-ichi
([1]Max-Planck-Inst. Chem. Phys. Stoffe, Germany)

[*Acta Physica Polonica B* **34**, 613–616 (2003)]

We report optical investigations of the electronic properties of the clath-rate compound Ba_6Ge_{25} in which at room temperature Ba atoms "rattle" in Ge-network cavities. When lowering the temperature across T_S ~ 200 K a lock-in of the Ba-atoms to split-site positions in the cages is observed. The low energy Drude type of reflectivity is characterized by a low charge carrier density which smoothly varies with temperature. However, the Drude relaxation time of the charge carriers is found to be almost temperature independent, especially when cooling below T_S where, according to thermopower data, the effective mass is enhanced. This behavior could indicate a formation of polaronic quasi particles below T_S which is also supported by previous measurements of magnetic susceptibility of Ba_6Ge_{25}.

VIII-GG-8 Infrared Magneto-Optical Imaging of κ-(BEDT-TTF)$_2$Cu[N(CN)$_2$]Br

NISHI, Tatsuhiko[1]; KIMURA, Shin-ichi; ITO, Takahiro; TAKAHASHI, Toshiharu[2]; MIYAGAWA, Kazuya[3]; KANODA, Kazushi[3]
([1]GUAS; [2]Kyoto Univ.; [3]Univ. Tokyo)

Since the ground state of κ-(BEDT-TTF)$_2$Cu-[N(CN)$_2$]Br locates in the vicinity of the boundary of the Mott transition, the weak perturbations of the deuteration and the rapid cooling make the phase transition from the superconductor to the antiferro-magnetic insulator. The phase separation is expected to appear on the boundary by the magnetic susceptibility data. Then we observed the spatial distribution of the optical spectrum in the infrared region because the peak at around $h\nu$ = 0.3 eV reflects the physical properties. At the result, the spectral distribution on the sample surface at T = 4 K was observed in spite that no distribution appears at 50 K. The result indicates that the phase separation appears at 4 K.

VIII-GG-9 Construction of Angle-Resolved Photoemission Apparatus for Solids

ITO, Takahiro; KIMURA, Shin-ichi; SODA, Kazuo[1]; TAKEUCHI, Tsunehiro[1]; TAKAHASHI, Kazutoshi[2]
([1]Nagoya Univ.; [2]Saga Univ.)

We have constructed a new high-energy-resolution angle-resolved photoemission apparatus shown in Figure 1 for the helical undulator beam line, BL5U. The main purpose is the investigation of the electronic structure near the Fermi level as well as the topological shape of the Fermi surface, so-called "fermiology," of solids, thin films and surfaces. The apparatus consists of a photoelectron analyzer (MBS-Toyama A-1), a main chamber, a sample preparation chamber, a liquid-He flow-type cryostat (JANIS ST-400 UHV) with a manipulator, a He lamp with UV monochromator (GAMMADATA VUV5000 + VUV5040) and several vacuum pumps. Samples are transferred to the preparation chamber from a load-lock chamber, a molecular beam epitaxy system or other chambers that can be replaced by users.

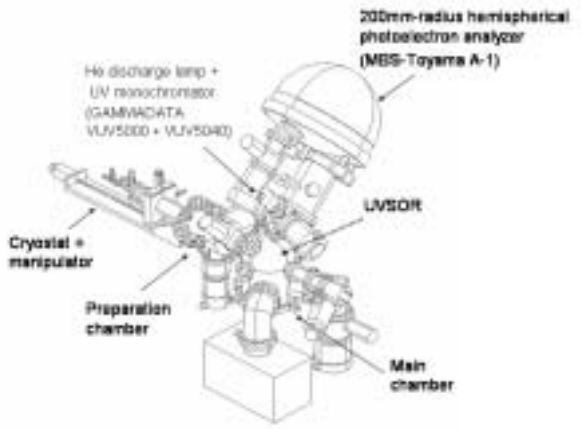

Figure 1. High-energy-resolution angle-resolved photo-emission apparatus for BL5U.

Computer Center

VIII-HH Computer Simulation of Quantum Systems in Condensed Phase

VIII-HH-1 An Analysis of Molecular Origin of Vibrational Energy Transfer from Solute to Solvent Based upon Path Integral Influence Functional Theory

MIKAMI, Taiji; OKAZAKI, Susumu

[*J. Chem. Phys.* **119**, 4790–4797(2003)]

Molecular process of vibrational energy relaxation of CN^- ion in the aqueous solution has been investigated based upon path integral influence functional theory. In order to obtain a molecular-based picture, bath normal coordinates were retransformed to Cartesian coordinate, Eulerian coordinate, and intramolecular vibrational coordinate of the solvent molecule. Then, based upon this retransformation matrix, coupling of the solute with the normal modes may be assigned to the couplings with the solvent molecules. Further, with respect to two-phonon process which is dominant in the relaxation of the present system, the relaxation may be divided into single- and dual-molecular processes. We show that the single-molecular relaxation is dominant in the relaxation. Further, water molecules in the first hydration shell play an essential role in the relaxation, whereas the solvent molecules outside the first hydration shell make little contribution. The solvent molecules located in the direction of CN^- bond axis were found to make great contribution to the relaxation.

VIII-HH-2 Mixed Quantum-Classical Molecular Dynamics Study of Vibrational Relaxation of CN^- Ion in Water: An Analysis of Coupling as a Function of Time

SATO, Masahiro; OKAZAKI, Susumu

[*J. Chem. Phys.* submitted]

Mixed quantum-classical molecular dynamics method has been applied to vibrational relaxation of CN^- in water. The calculated relaxation time was in good agreement with that based upon Fermi's golden rule with classical interaction. Flexible water model adopted here enhanced the relaxation rate by a factor of about 5 compared with the rigid rotor model. This supports our previous result of path integral influence functional theory that intramolecular bending of water plays an essential role in the relaxation. Time-dependent interaction between the solute vibrational degree of freedom and the solvent water shows random-noise-like behavior, no collisional or stationary coupling observed in gas or solid, respectively, being found in the liquid. The interaction has been analyzed in detail defining the effective coupling for the relaxation. The relaxation mechanism in the liquid may be described by a variety of effective couplings, *i.e.*, relaxing and exciting as well as strong and weak, which arise successively as a function of time.

VIII-II Molecular Dynamics Study of Classical Complex Systems

VIII-II-1 A Molecular Dynamics Study of Single Molecular Manipulation by AFM Cantilever—Mechanical Extension of Polyalanine—

IWAHASHI, Kensuke; MIKAMI, Taiji; IKAI, Atsushi[1]; OKAZAKI, Susumu
([1]Tokyo Inst. Tech.)

Potential of mean force of polyalanine in water has been calculated as a function of molecular length by molecular dynamics calculations simulating mechanical extension of the molecule by AFM cantilever. When the molecule keeps alpha helix structure, it behaves like a spring following Hooke's law. After the helix is broken, the force becomes large with increasing extension. Hydrophobic interaction and conformational entropy must play an important role for this force-extension curve. At the extension of about 100%, the force curve rises sharply, showing the increase of molecular bending energy of all trans conformation.

VIII-JJ Development of Simulation Algorithms for Quantum Many-Body Systems

VIII-JJ-1 Path Integral Hybrid Monte Carlo Algorithm for Correlated Bose Fluids

MIURA, Shinichi; TANAKA, Junji

[*J. Chem. Phys.* in press]

Path integral hybrid Monte Carlo (PIHMC) algorithm for strongly correlated Bose fluids has been developed. This is an extended version of our previous method applied to a model system consisting of non-interacting bosons. Our PIHMC method for the correlated Bose fluids is constituted of two trial moves to sample path-variables describing system coordinates along imaginary time and a permutation of particle labels giving a boundary condition with respect to imaginary time. The path-variables for a given permutation are generated by a hybrid Monte Carlo method based on path integral molecular dynamics techniques. Equations of motion for the path-variables are formulated on the basis of a collective coordinate representation of the path, staging variables, to enhance the sampling efficiency. The permutation sampling to satisfy Bose-Einstein statistics is performed using the multilevel Metropolis method developed by Ceperley and Pollock. Our PIHMC method has successfully been applied to liquid helium-4 at a state point where the system is in a superfluid phase. Parameters determining the sampling efficiency are optimized in such a way that correlation among successive PIHMC steps is minimized.

VIII-KK Theoretical Studies on Electronic Structure and Dynamics of Electronically Excited States

VIII-KK-1 Millimeter-Wave Spectroscopy of the Internal-Rotation Band of the X-HCN Complex (X = He, Ne, and Ar) and the Intermolecular Potential Energy Surface

HARADA, Kensuke[1]; TANAKA, Keiichi[1]; TANAKA, Takehiko[1]; NANBU, Shinkoh; AOYAGI, Mutsumi[1]
([1]Kyusyu Univ.)

Millimeter-wave absorption spectroscopy combined with a pulsed-jet expansion technique was applied to the measurement of the internal-rotation band of the X-HCN (X = He, Ne, and Ar) in the frequency region of 95–125 GHz. The observed transition frequencies were analyzed including their hyperfine splitting to yield an intermolecular potential energy surface, as improved from the one given by a coupled-cluster single double (triple) ab initio calculation. Regarding the He complex, the surface obtained has a global minimum in the linear configuration (He···H–C–N) with a well depth of 30.2 cm^{-1}, and the saddle point located in the anti-linear configuration (H–C–N···He) is higher by 8.174 cm^{-1} in energy than the global minimum. The distance R_m between the He atom and the center of mass of HCN along the minimum energy path shows a strong angular dependence; R_m = 4.169 Å and 4.040 Å in the linear and anti-linear forms, respectively, while it is 3.528 Å in a T-shaped configuration. The energy level diagram is consistent with the millimeter-wave observation. And now, we are trying to measure the stretching motion located just below the dissociation limits.

VIII-KK-2 Theoretical Study of Vibrational Spectra of *p*-Tert-Butylcalix[4]crown-6-Ether Complexed with Ethyl Ammonium Cations

MINAMINO, Satoshi; CHOE, Jong-In[1]; CHANG, Suk-Kyu[1]; MIZUTANI, Fumiyasu; NANBU, Shinkoh
([1]Chung-Ang Univ.)

[*Chem. Phys. Lett.* **374**, 572–576 (2003)]

Theoretical infrared (IR) absorption spectra were calculated for *p-tert*-butylcalix[4] crown-6-ether (1) in the cone conformer and its ethyl ammonium complex. The IR spectra were obtained by restricted Hartree-Fock (RHF) calculations with the 6–31 G basis set. For the purpose of an absorption band assignment on the host molecule, guest molecule, and complexes thereof, we discussed a way to distinguish a specific molecule by comparing the calculated vibrational spectra. The theoretical result for the host molecule and its ethyl ammonium complex were preliminarily compared with the experimental result, and found that the calculated result agrees well with the features of the experimental spectra.

VIII-KK-3 He*(2^3S) Penning Ionization of H_2S I. Theoretical Franck-Condon Factors for the $H_2S(X^1A_1, v' = 0) \rightarrow H_2S^+ (X^2B_1, A^2A_1)$ Ionization and the H_2S^+ (A-X) Transitions

TOKUE, Ikuo[1]; YAMASAKI, Katsuyoshi[1]; NANBU, Shinkoh
([1]Niigata Univ.)

[*J. Chem. Phys.* in press]

In order to elucidate the ionization dynamics, in particular the vibrational distribution, of $H_2S^+(\tilde{A})$ produced by the Penning ionization of H_2S with He*(2^3S) atoms, the Franck-Condon factors (FCFs) were presented for the $H_2S(\tilde{X}) \rightarrow H_2S^+(\tilde{X}, \tilde{A})$ ionization and the $H_2S^+(\tilde{A}–\tilde{X})$ transition, and Einstein's A coefficients were presented for the latter transition. The FCFs were obtained by quantum vibrational calculations using the global potential energy surfaces (PESs) of $H_2S(\tilde{X}\,^1A_1)$ and $H_2S^+(\tilde{X}^2B_1, \tilde{A}^2A_1, \tilde{B}^2B_2)$ electronic states. The global PESs were determined by the multi-reference configuration interaction calculations with the Davidson correction (MRCI+Q) and the interpolant moving least squares (IMLS) method combined with the Shepard interpolation. The obtained FCFs exhibit that the $H_2S^+(\tilde{X})$ state primarily populates the vibrational ground state since its equilibrium geometry is almost equal to that of $H_2S(\tilde{X})$, while the bending mode (ν_2) is strongly enhanced for the $H_2S^+(\tilde{A})$ state; the maximum in the population is around ν_2 = 6–7. In the same manner, the bending progressions are expected to consist of the great part of the $H_2S^+(\tilde{A}–\tilde{X})$ emission. A detailed comparison with the experimental study for this system is reported in the accompanying paper, Paper II.

VIII-KK-4 He*(2^3S) Penning Ionization of H_2S II. Formation of $SH^+(A^3\Pi)$ and H_2S^+ (A^2A_1) Ions

TOKUE, Ikuo[1]; YAMASAKI, Katsuyoshi[1]; NANBU, Shinkoh
([1]Niigata Univ.)

[*J. Chem. Phys.* in press]

Emissions in the 200–750 nm region produced by the collision of He(2^3S) with H_2S were studied under single-collision conditions. The hydrogen Balmer lines and the $SH^+(A^3\Pi–X^3\Sigma^-)$ and $H_2S^+(\tilde{A}^2A_1–\tilde{X}^2B_1)$ bands were assigned. The total emission cross section (σ_{em}) was evaluated to be $(1.7 \pm 0.3) \times 10^{-20}$ m^2 at a collision energy of 150 meV. The σ_{em}'s of the $SH^+(A–X)$ and $H_2S^+(\tilde{A}–\tilde{X})$ bands decreased with increase in the collision energy in the 115–200 meV range, indicating that attractive forces are effective for the incident channels with regard to the formation of these species. The rotational distribution of $SH^+(A^3\Pi, v' = 0)$ is represented by a Boltzmann temperature of 870 ± 80 K. The $H_2S^+(\tilde{A}^2A_1–\tilde{X}^2B_1)$ emission, which was assigned

for the first time in the Penning ionization of H_2S, primarily consists of the bending progressions. The internal populations of $H_2S^+(\tilde{A})$ were analyzed using the vibrational energies and Einstein's *A* coefficients calculated in this study. The details of the calculation and derived spectroscopic constants are reported in the accompanying paper, Paper I. The populations obtained for the bending vibration (ν_2') of $H_2S^+(\tilde{A})$ show an inverted distribution with a peak at v_2' = 3. This distribution is shifted lower compared that with a peak at v_2' = 4–5 observed by He(2^3S) Penning ionization electron spectroscopy and that with a peak at v_2' = 6–7 predicted by the theoretical Franck-Condon factors (FCFs) for the $H_2S(\tilde{X})$–$H_2S^+(\tilde{A})$ ionization. The origin of the difference is discussed concerning the formation mechanism of $H_2S^+(\tilde{A}^2A_1)$.

VIII-KK-5 Theoretical Analysis of the Oxygen Insertion Process in the Oxidation Reactions of H_2O + H/Si(100) and 2H + H_2O/Si(100); Calculation of an Ab Initio Molecular Orbital Method and an Analysis of the Tunneling Reaction

WATANABE, Hidekazu[1]; NANBU, Shinkoh; MAKI, Jun[2]; WANG, Zhi-Hong; URISU, Tsuneo; AOYAGI, Mutsumi[2]; OOI, Kenta[1]
([1]Niigata Univ.; [2]Kyusyu Univ.)

[*Chem. Phys. Lett.* submitted]

The reaction paths were analyzed, by an ab initio molecular orbital method, for the surface reaction systems, 2H + H_2O/Si(100)-(2×1) and H_2O + H/Si(100)-(2×1), in which SiH_2 species with one or two oxygen atom-inserted back bonds have been observed as new stable reaction products. It was found that common metastable states exist in both systems, and the initial energy is sufficiently higher than all transition state energies in the former system, while in the latter system, the energy of the highest transition state is much higher than the initial energy, and thus a tunneling effect plays an important role.

VIII-KK-6 Optimal Control of Quantum Chaotic Dynamics

TAKAMI, Toshiya; FUJISAKI, Hiroshi[1]; MIYADERA, Takayuki[2]
([1]Boston Univ.; [2]Tokyo Univ. Sci.)

We numerically investigate how chaos affects controllability of wavepacket dynamics using the monotonically convergent method of optimal control theory introduced by Zhu, Bonita, and Rabitz [*J. Chem. Phys*. **108**, 1953 (1998)]. We find that a quantized kicked rotor in a bounded phase space is successfully controlled with the method, *i.e.*, an initial Gaussian wavepacket can be steered to a target Gaussian wavepacket with a high probability, even in strongly chaotic regions when the target time *T* is larger than a minimal time $T_{\min}$. We also find that $T_{\min}$ saturates to a certain value as the system becomes a random matrix system.